

Physical systems evolving on time-dependent domains

by

Mahdi Ghadiri Motlagh

A thesis submitted in partial fulfillment of the requirements for the degree of

Doctor of Philosophy

in

Applied Mathematics

Department of Mathematical and Statistical Sciences

University of Alberta

© Mahdi Ghadiri Motlagh, 2020

Abstract

Despite the ubiquity of physical systems evolving on time-dependent spatial domains ranging from crystal growth, formation of patterns and shapes in biology and living organisms – animals skin patterns, tentacle patterns on Hydra, whorled leaves, teeth primordia in the alligator – to quantum particles traveling in a time-evolving potential, fluid motion, fluid-structure interaction, and galaxies agglomeration in the expanding Universe, to name a few, understanding their regular and chaotic dynamical properties is still in a quite rudimentary state. The underlying theme of this dissertation is to explore the key differences in the dynamics – both regular and chaotic – between extended systems on time-fixed and time-dependent spatial domains, studied here with the synergy of experimental and theoretical approaches and numerical simulations.

In the quest to understand dynamics of distributed systems on time-dependent spatial domains, in chapter 2, we study experimentally the response to domain deformations by Faraday wave patterns – standing waves formed on the free surface of a liquid layer due to its vertical vibration – chosen as a paradigm owing to their historical use in testing new theories and ideas. In our experimental setup of a vibrating water container with controlled positions of lateral walls and liquid layer depth, the characteristics of the patterns are measured using the Fourier transform profilometry technique, which allows us to reconstruct an accurate time history of the pattern three-dimensional landscape and reveal how it reacts to the domain dynamics on various length- and time-scales.

Analysis of Faraday waves on growing, shrinking, and oscillating domains leads to a number of intriguing results. First, the observation of a transverse instability – namely, when a two-dimensional pattern experiences an instability in the direction orthogonal to the direction of the domain deformation – provides a new facet to the stability picture compared to one-dimensional

systems in which the longitudinal (Eckhaus) instability accounts for pattern transformation on time-dependent domains. Second, the domain evolution rate is found to be a key factor dictating the patterns observed on the path between the initial and final domain aspect ratios. Its effects range from allowing the formation of complex sequences of patterns to impeding the appearance of any new pattern on the path. Third, the shrinkage-growth process turns out to be generally irreversible on a horizontally evolving domain, but becomes reversible in the case of a time-dependent liquid layer depth, i.e. when the dilution and convective effects are absent. These experimentally observed enigmatic effects of the domain size variations in time are complemented here with appropriate theoretical insights elucidating the nature of the phenomena and disentangling the dynamics of two-dimensional pattern evolution, which proves to be more intricate compared to one-dimensional systems.

In chapter 3, we present the experimental discovery of a novel mechanism to control chaos by time-variation of the spatial domain size. Moreover, depending upon the rate of the latter the chaotic state may be prevented altogether. As a testbed to traverse the edge of chaos by varying the domain size, we have chosen the Faraday waves phenomenon, which is a paradigmatic example in pattern-forming systems due to its simplicity and richness, in particular known to exhibit temporal chaos. The experimental findings are disentangled with theoretical insights and numerical modeling, which also demonstrates the ability to control spatio-temporal chaos. These findings may shed some light on biological systems and life, which require ‘a healthy dose of chaos’ for proper operation (Korolja *et al.*, 2019) and hence often balance on the edge of chaos. The latter concept has also been applied in many other areas (Waldrop, 1993): in economy, creative destruction represents the driving force within a market economy; in social science, the dynamic interaction between individuals and macro-levels such as laws, religions, and governments imposing too much order and limiting individual development in the name of conformity, ultimately leading to stasis; in human cognition and creativity (Schwartz, 2014), the states at the edge of chaos can be seen to be maximally novel while still connected to ones in the ordered regime – the hallmark of innovative thinking.

Preface

This dissertation is an original work by Mahdi Ghadiri under the supervision of Professor Krechetnikov at the University of Alberta, Department of Mathematical and Statistical Sciences.

A version of chapter 2 is published in the *Journal of **Fluid Mechanics*** as Ghadiri, M. & Krechetnikov, R. (2019) “Pattern formation on time-dependent domains”, *J. Fluid Mech.* 880, 136–179. In that work, all the experiments were performed in Krechetnikov Fluid Physics Laboratory (KFPL) and M. Ghadiri was responsible for building the experimental platform, conducting the experiments, and data analysis. All the latter tasks have been accomplished under the insightful supervision of Professor Krechetnikov. Both authors contributed to the manuscript composition and its revisions.

Chapter 3 is prepared and finalized for submission to the *Journal of **Nature*** as Ghadiri, M. & Krechetnikov, R. “Controlling chaos by the system size”. In that work, all the experiments were performed in KFPL and M. Ghadiri was responsible for building the experimental platform, conducting the experiments, data analysis, and numerical simulation. Professor Krechetnikov supervised all the latter stages of the project. Both authors contributed to the manuscript composition and its revisions.

An extended version of Appendix 2.D is being prepared for submission to the *Journal of **Applied Optics*** as Ghadiri, M. & Krechetnikov, R. “Common-optical axis Fourier transform profilometry for free surface waves”. In that work, all the experiments were performed in KFPL and M. Ghadiri was responsible for the development of the underlying theoretical principles, building the experimental platform, conducting the experiments, and data analysis while being supervised by Professor Krechetnikov. Both authors will contribute to the manuscript composition and its revisions.

Acknowledgements

First and foremost, I would like to express my great appreciation to my supervisor and mentor Professor Rouslan Krechetnikov for his endless patience and guidance throughout my Ph.D. program. In this journey, Rouslan has opened up many opportunities for me and has always looked out for my best interests, and it has been an honor to be his Ph.D. student. In addition, I thank him for highlighting many skills crucial for becoming a successful researcher – in particular the importance of understanding the physics behind every phenomenon and how finer details and nuances are essential in painting an overall picture of phenomena. On the financial side, he provided me with the research assistant funding, teaching assistant support, and the opportunity and the guidance to apply for different awards and scholarships. I will always be grateful for the privilege to be part of the Krechetnikov Fluid Physics Laboratory under his insightful supervision. I hope to carry forward what I have learned from him into my future endeavors.

I am very grateful to all committee members of my thesis defense for their invaluable time and patience for reading through this thesis. In particular, I would like to express my gratitude for Professor Djubjevic's support, encouragement, and constructive feedback over the years.

I would like to acknowledge financial support from an Alberta Graduate Excellence Scholarship, a Josephine M. Mitchell Scholarship, a Clement W. Bowman Mathematical Turbulence Award, and a Doctoral Recruitment Scholarship.

I would also like to extend my gratitude to the support staff of the Department of Mathematical and Statistical Sciences, most notably Professor Kuttler, Tara Schuetz, and Sean Graves, for not only helping me navigate the unavoidable bureaucracy of a graduate program, but also for providing invaluable advice and guidance. I am also thankful for the privilege of having access to the machine

shop and advanced machining facilities in the Physics department at the University of Alberta. In particular, I appreciate Mr. Tony Vinagreiro's time and patience while helping me to acquire machining skills.

I am incredibly grateful for the support of my friends. A special thanks to Quinton Farr who always patiently agrees to proofread anything and everything that I write. My sincere thank you also goes to Pedram Emami for his fraternal support and the time we spend together throughout these years.

Finally, I would like to thank my family for all of their encouragement despite the distance, especially my sister, whose support afforded me the chance to realize my dreams and goals in my academic path. Among many wonderful things I am blessed with, my wife Maliheh is the greatest gift and I would like to thank her for being the primary source of my motivation and enthusiasm. Beyond a shadow of doubt, this journey would have never come to successful completion without Maliheh on my side.

Contents

List of Figures	ix
1 Introduction:	1
1.1 General context: problems on time-dependent domains	1
1.2 Faraday waves	3
1.2.1 General formulation	4
1.2.2 Linear stability analysis	7
2 Faraday waves on time-dependent domains	14
2.1 Experimental setup and procedure	15
2.1.1 Faraday waves apparatus	15
2.1.2 Visualization and measurement technique	18
2.2 Results: Faraday waves on time-fixed domain	21
2.2.1 Boundary conditions	22
2.2.2 Road-map	23
2.2.3 Thresholds	26
2.2.4 Symmetric mode interactions	27
2.2.5 Summary	31
2.3 Results: Faraday waves on time-dependent domain	32
2.3.1 Phase-slip phenomena	32
2.3.2 Transverse instability	36
2.3.3 Irreversibility	38

2.3.4	Wall speed effects	42
2.3.5	Effect of initial conditions	46
2.3.6	Effect of domain shrinkage or growth on the final stage mode	52
2.3.7	Effect of wall oscillation	53
2.3.8	Draining water tank	55
2.4	Conclusions	58
Appendix 2.A	Effects of gaps underneath the moving walls	61
Appendix 2.B	Meniscus waves	63
Appendix 2.C	Damping sources and effects	64
Appendix 2.D	Common optical axis FTP for free surface waves	69
3	Controlling chaos by the system size	75
3.1	Chaotic Faraday waves and the road map	75
3.2	Traversing the edge of chaos by changing the system size	78
3.3	The effect of the domains evolution rate: chaos prevention	80
3.4	Relation to frequency chirping	83
3.5	The Ginzburg-Landau model	86
3.5.1	Numerical simulation of cGLE on time-fixed domains	87
3.5.2	Numerical simulation of cGLE on time-dependent domains	92
3.5.3	Traversing the edge of chaos	94
3.5.4	The effect of the domain evolution rate	97
3.6	Methods	99
	Conclusions	106
	Bibliography	108

List of Figures

1.1	Patterns observed in problems on time varying domains.	1
1.2	Faraday waves period driven by a harmonic excitation.	3
1.3	Sketch of the accelerated liquid.	5
1.4	Examples of Faraday modes in a rectangular domain.	12
2.1	The Faraday waves assembly and optical setup.	15
2.2	Container sketch and contact angle between water and the walls.	17
2.3	Experimental contact line conditions.	21
2.4	Amplitude-frequency diagram in cosine and sine regimes.	24
2.5	Stability curves for various Faraday modes.	26
2.6	Amplitude-frequency diagram around mode (6, 2) and its symmetric one (2, 6) on a square domain.	28
2.7	Schematic of periodic/chaotic pattern competition regimes of two adjacent modes. .	30
2.8	Phase-slip event on the time-dependent domain.	34
2.9	Transverse instability versus direct instability.	36
2.10	Patterns observed on domain shrinkage versus growth paths.	39
2.11	Patterns observed on shrinkage and growth paths with four distinct wall speeds. . .	44
2.12	Patterns observed on two different runs with two initial modes.	47
2.13	Phase-space portrait, attractor and embedding dimension, and sum of the positive Lyapunov exponents in pattern competition regime between modes $a_{(4,4)}$ and $a_{(2,6)}$. .	49
2.14	The required amplitude and frequency of wall oscillation to destroy a mode (1, n). .	55

2.15	Patterns observed in the draining water tank.	57
A2.1	Optimization of the gap height under moving walls, and flow field observed in the bulk.	61
A2.2	Faraday patterns observed on time-fixed domain with and without the gaps under- neath the walls.	62
A2.3	Various geometrical implementation of Fourier transform profilometry.	69
A2.4	Geometry of the optical paths in Fourier transform profilometry.	70
3.1	Physical experiment: road map.	76
3.2	Physical experiment: regime change in response to domain deformation.	78
3.3	The correlation function.	79
3.4	Physical experiment: wall speed effect.	81
3.5	Physical experiment: regime change in response to frequency chirping.	84
3.6	Numerical modeling: regime change in response to domain growth.	95
3.7	Numerical modeling: regime change in response to domain shrinkage.	96
3.8	Numerical modeling: domain evolution rate effect on periodic initial state.	98
3.9	Numerical modeling: domain evolution rate effect on chaotic initial state.	100
3.10	Experimental setup.	101
3.11	Data analysis procedure.	103

Chapter 1

Introduction:

1.1 General context: problems on time-dependent domains

Despite the ubiquity of physical systems evolving on time-dependent spatial domains ranging from crystal growth, skin patterns on tropical fish (cf. figure 1.1a), crown formation in the drop splash problem (cf. figure 1.1b) to quantum particles traveling in a time-evolving potential and galaxies agglomeration in the expanding Universe, to name a few, understanding their dynamical properties is still in a rudimentary state (Knobloch & Krechetnikov, 2015). For example, standard boundary-value theory developed for ordinary and partial differential equations on time-fixed domains proves to be largely irrelevant because after mapping time-dependent onto time-fixed domains, the differential operators become non-autonomous thus simply moving the difficulty to a different realm. Hence, advancing, both theoretically and experimentally, our understanding of the very basic el-

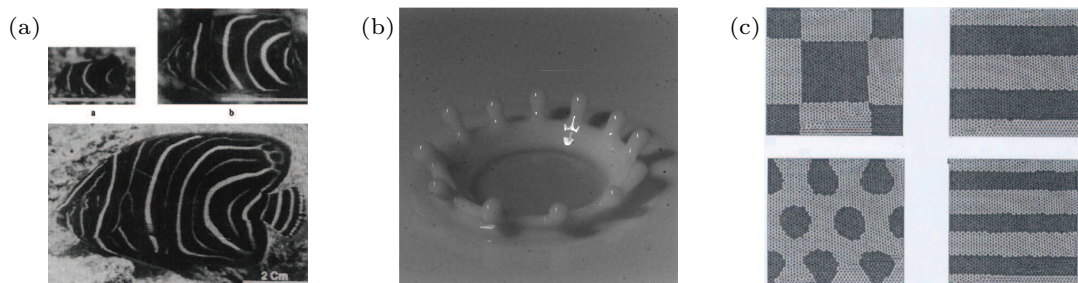


Figure 1.1: Patterns observed in problems on time varying domains: (a) *Pomacanthus semicirculatus* (Painter *et al.*, 1999), (b) crown in the drop splash problem (Hartong-Redden & Krechetnikov, 2011), (c) reaction-diffusion on a growing square domain (Madzvamuse *et al.*, 2003).

ements in the dynamics on time-varying domains is vital for penetrating into the nature of more complex phenomena.

One area where many efforts have been recently put forth is developmental biology, providing both counterpart – reaction-diffusion vs fluid roll system – and context for our study. Historically, morphogenesis in biology – e.g. the stripe patterning observed in the aging Pomacanthus fish (Kondo & Asai, 1995; Painter *et al.*, 1999) – was originally suggested by Turing (1952) to be due to reacting and diffusing morphogens, which interact to produce, via an instability, patterns in concentration. The issue, however, is that this Turing instability on stationary domains occurs under quite restrictive diffusion-controlled conditions: namely, to achieve an instability one must enforce one of the species to diffuse much faster than the other, and hence, due to sensitivity, pattern formation requires tight control of involved parameters and initial conditions and therefore cannot be considered as robust. This constitutes one of the major criticisms of reaction-diffusion theory for pattern formation (Bard & Lauder, 1974), though Turing-type patterns were eventually observed experimentally (Castets *et al.*, 1990; Ouyang & Swinney, 1991). In the search for more robust pattern formation in reaction-diffusion systems, various modifications to the original Turing treatment have been made, in particular taking into account *domain growth* and changes in geometry, cf. figure 1.1c. Crampin *et al.* (1999) showed that in one dimension domain growth may be a mechanism for increased robustness, e.g. in the case of exponential growth a frequency-doubling sequence appears. In fact, there are examples of reaction-diffusion systems which cannot exhibit a diffusively-driven instability in a fixed domain, but are unstable in the presence of slow domain growth (Madzvamuse *et al.*, 2010). Despite much progress in observations, most of the above studies resort to numerical simulations thus providing little insight in the fundamental underlying mechanisms responsible not only for various metamorphoses in pattern formation, but also for the simple creation of a new pattern cell.

Besides reaction-diffusion-driven patterns observed in biology, chemistry, geology, physics, and ecology, another wide class of patterns is encountered in fluid dynamics – such as hexagons and squares in convection and capillary-gravity surface waves driven by external periodic excita-

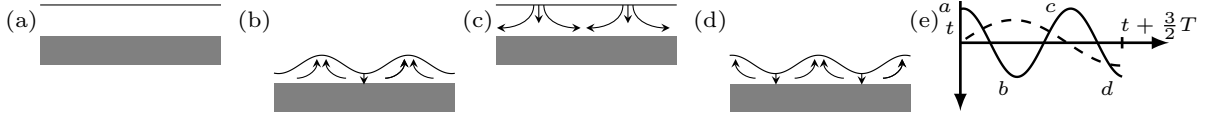


Figure 1.2: Established Faraday waves driven by a harmonic excitation (Douady, 1990). (a) The tank is accelerated downwards at time instant t . (b) While initially the acceleration is positive and hence the air-liquid interface is stable according to the Rayleigh-Taylor theory, the tank must decelerate before reaching the bottom position (b) and at this stage of negative acceleration the heavier liquid is accelerated into the lighter air leading to a Rayleigh-Taylor instability. At the end of this deceleration (b), the water tank is located at its minimum and the Faraday wave has attained its maximum amplitude, which corresponds to $t + \frac{1}{2}T$, where T is the period of the shaker motion. After that the tank starts to move upward which will cause the deformation of the surface to reduce and once the water tank reaches its maximum, the surface deformation will disappear for a moment (c) at $t + T$, which happens provided the fluid motion is periodic. (d) Following another half-period of excitation, at $t + \frac{3}{2}T$ the induced flow will carry the maxima into the minima and vice-versa compared to (b). (e) The shaker position (solid) and the Faraday wave amplitude (dashed) are plotted as functions of time with various stages labeled. Between stages a to c the shaker oscillates for one full period T while the Faraday waves only oscillate for half a period, $T = T_0/2$.

tions (Cross & Hohenberg, 1993) – with an underlying roll structure in the bulk below the free surface. Naturally, such systems may also evolve on the domains either varying in time periodically or experiencing growth/decay (Krechetnikov & Knobloch, 2017). The lack of a systematic connection of theory to observations in fluid systems motivated us to come up with controlled *two-dimensional* (2D) physical experiments, which will further the fundamental understanding of the dynamics of extended systems on time-dependent spatial domains. As a paradigm, we have chosen the Faraday waves phenomenon not only because it provides full control over pattern formation on a time-dependent domain, but also because its dynamics on time-fixed domains has been extensively studied and reasonably well understood for a long time.

1.2 Faraday waves

To provide the basic background, we briefly introduce the reader to the Faraday waves phenomenon, cf. figure 1.2. As first studied by Faraday (1831) in a remarkable for his time set of experiments (Gollub, 2006), when a vessel containing liquid is vibrated vertically a pattern of standing waves at the free surface is observed oscillating at a frequency half that of the vessel, which was later confirmed by Rayleigh (1883) after the controversial work of Matthiessen (1868).

Faraday's observations remained unexplained until [Rayleigh \(1883\)](#) envisaged that the waves result from a parametric resonance analogous to the motion of a simple pendulum of length \mathbb{L} subjected to a vertical oscillation of its pivot. If the acceleration of the pivot is $\epsilon g \cos \omega t$, where ω is the angular velocity, g the gravitational field acceleration, and ϵ the small scaling factor, evolution of the angular displacement $\theta(t)$ in time t obeys

$$\theta'' + \omega_0^2 (1 + \epsilon g \cos \omega t) \theta = 0, \quad (1.1)$$

with $\omega_0 = (g/\mathbb{L})^{1/2}$ being the frequency of small natural oscillations at $\epsilon = 0$, which for $\epsilon \neq 0$ are modulated at a different frequency ω . Moving the modulating part to the right-hand side of (1.1), the equation assumes the form of a simple oscillator driven by a signal $\epsilon \omega_0^2 g \theta \cos \omega t$, that is proportional to its response θ . Obviously, if $\theta(t) \sim \cos \omega_0 t$ already has oscillation at frequency ω_0 and the small amplitude ϵ pumping $f(t) \sim \cos \omega t$ has the double frequency $\omega = 2\omega_0$, from a trigonometric identity it follows that $f(t) \theta(t) \sim \cos \omega_0 t$, where we neglected the harmonic $\cos 3\omega_0 t$ as it attenuates due to being off-resonance. Thus, for $\epsilon \ll 1$ equation (1.1) admits the solution $\theta(t) \sim \cos(\omega t/2)$ subharmonic with respect to the driving frequency ω : the null solution loses stability to this subharmonic one in the frequency interval $\omega_0^2(1 - \epsilon/2) < (\omega/2)^2 < \omega_0^2(1 + \epsilon/2)$. Rayleigh's point of view was confirmed by [Benjamin & Ursell \(1954\)](#) linear approach and will be considered here in detail: starting from the inviscid Euler equations it will be demonstrated that for small amplitudes each normal mode of the liquid sloshing in the container acts as a harmonic oscillator with the natural frequency determined by the dispersion relation for capillary-gravity waves.

1.2.1 General formulation

We consider an inviscid and incompressible fluid housed in a vessel that oscillates with acceleration $A \cos(\omega t)$, cf. figure 1.3. Then the effective acceleration in a coordinate system attached to the moving vessel becomes $\mathbf{G}(t) = [0, 0, g - A \cos(\omega t)]$, where the positive z direction is assumed to be downward. Neglecting the effects due to the wetting of the walls, the bulk dynamics is governed

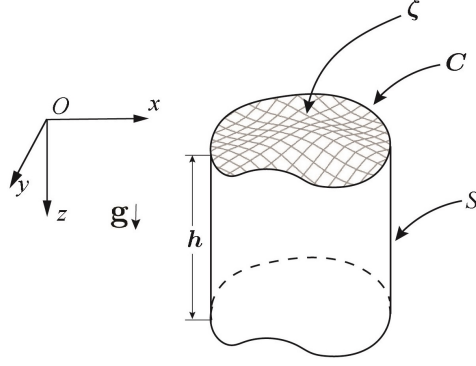


Figure 1.3: Sketch of the accelerated liquid. h , ζ , C , and S denote the depth of the fluid, the free surface, the curve bounding the latter, and the wetted wall surface, respectively.

by the Euler equations of incompressible fluid of constant density ρ :

$$\frac{\partial \mathbf{u}}{\partial t} + (\mathbf{u} \cdot \nabla) \mathbf{u} = -\frac{1}{\rho} \nabla p + \mathbf{G}(t), \quad (1.2a)$$

$$\nabla \cdot \mathbf{u} = 0, \quad (1.2b)$$

where $\mathbf{u} = (u, v, w)$ is the velocity field and p the pressure. Assuming the motion started from rest, the circulation remains zero and hence the flow is irrotational and there exists a potential function ϕ defined via $\mathbf{u} = \nabla \phi$,

$$\nabla \left(\frac{\partial \phi}{\partial t} \right) + \frac{1}{2} \nabla |\mathbf{u}|^2 = -\nabla \left(\frac{p}{\rho} \right) + \mathbf{G}(t), \quad (1.3)$$

where we have used the identity $(\mathbf{u} \cdot \nabla) \mathbf{u} = \frac{1}{2} \nabla |\mathbf{u}|^2 - \mathbf{u} \times (\nabla \times \mathbf{u})$, with the latter term being zero due to irrotational flow. Furthermore, by rewriting the mass force as $\mathbf{G}(t) = \nabla ([g - A \cos(\omega t)] z)$ equation (1.3) reduces to

$$\nabla \left(\frac{p}{\rho} + \frac{\partial \phi}{\partial t} + \frac{1}{2} |\mathbf{u}|^2 - [g - A \cos(\omega t)] z \right) = 0, \quad (1.4)$$

and therefore, leading to Lagrange-Cauchy integral

$$\frac{p}{\rho} + \frac{\partial \phi}{\partial t} + \frac{1}{2} (u^2 + v^2 + w^2) - [g - A \cos(\omega t)] z = F(t). \quad (1.5)$$

where $F(t)$ is the constant of the integration. Since the hydrostatic term gz is already included in the above equation, the pressure at the interface becomes $p = p_0 + \sigma (\kappa_1 + \kappa_2)$, where p_0 is the atmospheric pressure acting on the surface, σ the surface tension and κ_1, κ_2 are the principal curvatures of the surface. The function $F(t)$ and p_0 – after evaluating equation (1.5) at the interface $z = \zeta(t, x, y)$ – can be absorbed in the potential function: since the potential function is not uniquely defined and the velocity is the spatial derivative of ϕ we can add to ϕ any function of the time, therefore redefining the potential function in equation (1.5) as $\phi = \phi - (p_0/\rho)t + \int_0^t F(s)ds$ leads to $\frac{\sigma(\kappa_1+\kappa_2)}{\rho} + \frac{\partial\phi}{\partial t} + \frac{1}{2}(u^2 + v^2 + w^2) - [g - A \cos(\omega t)] \zeta = 0$.

With the surface deformation defined as $\zeta(t, x, y)$, the kinematic boundary condition can be written most conveniently using an implicit representation of the interface, $\mathcal{F}(t, x, y, z) = \zeta(t, x, y) - z = 0$:

$$\frac{\partial\mathcal{F}}{\partial t} + \nabla\mathcal{F} \cdot \mathbf{u} = 0 \quad \Longrightarrow \quad \frac{\partial\zeta}{\partial t} + u\frac{\partial\zeta}{\partial x} + v\frac{\partial\zeta}{\partial y} - w = 0 \quad \text{on } z = \zeta(t, x, y). \quad (1.6)$$

At the walls and the bottom, the boundary conditions are of the no-penetration form:

$$\frac{\partial\phi}{\partial\mathbf{n}} = 0 \quad \text{on } S, \quad (1.7a)$$

$$\frac{\partial\phi}{\partial z} = 0 \quad \text{at } z = h, \quad (1.7b)$$

where S is the wetted surface of the vessel wall (figure 1.3), \mathbf{n} the normal to such a surface, and h the layer depth of the fluid.

All of the considerations above lead to the harmonic equation for the potential ϕ and the Lagrange-Cauchy integral for the pressure p , and interfacial dynamics:

$$\text{bulk (velocity) } z \geq \zeta(t, x, y) : \quad \left\{ \begin{array}{l} \nabla^2\phi = 0, \\ \frac{\partial\phi}{\partial\mathbf{n}} = 0 \quad \text{on } S, \\ \frac{\partial\phi}{\partial z} = 0 \quad \text{at } z = h, \end{array} \right. \quad \begin{array}{l} (1.8a) \\ (1.8b) \\ (1.8c) \end{array}$$

$$\text{bulk (pressure) } z \geq \zeta(t, x, y) : \quad \frac{p}{\rho} + \frac{\partial \phi}{\partial t} + \frac{1}{2} (u^2 + v^2 + w^2) - [g - A \cos(\omega t)] z = 0, \quad (1.8d)$$

$$\text{interface (dynamic) } z = \zeta(t, x, y) : \quad p = \sigma (\kappa_1 + \kappa_2), \quad (1.8e)$$

$$\text{interface (kinematic) } z = \zeta(t, x, y) : \quad \frac{\partial \zeta}{\partial t} + u \frac{\partial \zeta}{\partial x} + v \frac{\partial \zeta}{\partial y} - w = 0. \quad (1.8f)$$

1.2.2 Linear stability analysis

To find the analytical solution with the help of linear approximation, equation (1.8d) is evaluated at the interface $z = \zeta(t, x, y)$, and with the assumption of ζ being small, both equations (1.8d) and (1.8f) are linearized about $z = 0$:

$$\frac{\partial \zeta}{\partial t} = w|_{z=0} = \frac{\partial \phi}{\partial z} \Big|_{z=0}, \quad (1.9)$$

$$\frac{\sigma}{\rho} \left(\frac{\partial^2 \zeta}{\partial x^2} + \frac{\partial^2 \zeta}{\partial y^2} \right) + \frac{\partial \phi}{\partial t} \Big|_{z=0} - [g - A \cos(\omega t)] \zeta = 0, \quad (1.10)$$

where, the expansion $\xi|_{z=\zeta} = \xi|_{z=0} + \frac{\partial \xi}{\partial z} \Big|_{z=0} \zeta + \dots$, with ξ representing any of the terms $\frac{\partial \phi}{\partial t}$, $\frac{\partial \phi}{\partial z}$, and w has been used for the linearization about $z = 0$. In such an expansion, all of the terms on the right hand side, except the first one, are dropped due to linearization. It should be noted that the surface deformation is a function of only x, y , and t , therefore, the linearization about $z = 0$ and accordingly the expansion above are not applicable for $\zeta(t, x, y)$. Also, with the assumption of surface deformation ζ , and the slopes $\frac{\partial \zeta}{\partial x}$, $\frac{\partial \zeta}{\partial y}$ being small, the sum of principal curvatures becomes

$$\begin{aligned} \kappa_1 + \kappa_2 = & \left[\frac{\partial^2 \zeta}{\partial x^2} \left(1 + \left(\frac{\partial \zeta}{\partial x} \right)^2 \right) + \frac{\partial^2 \zeta}{\partial y^2} \left(1 + \left(\frac{\partial \zeta}{\partial y} \right)^2 \right) - 2 \frac{\partial \zeta}{\partial x} \frac{\partial \zeta}{\partial y} \frac{\partial^2 \zeta}{\partial x \partial y} \right] \\ & \cdot \left[1 + \left(\frac{\partial \zeta}{\partial x} \right)^2 + \left(\frac{\partial \zeta}{\partial y} \right)^2 \right]^{-3/2} \approx \frac{\partial^2 \zeta}{\partial x^2} + \frac{\partial^2 \zeta}{\partial y^2}, \end{aligned} \quad (1.11)$$

and accordingly $p = \sigma (\kappa_1 + \kappa_2) \approx \sigma \left(\frac{\partial^2 \zeta}{\partial x^2} + \frac{\partial^2 \zeta}{\partial y^2} \right)$.

For future reference we note that using equation (1.9), the surface deformation ζ may be eliminated from equation (1.10) yielding a single equation involving the potential function only:

$$\frac{\sigma}{\rho} \left(\frac{\partial^2}{\partial x^2} + \frac{\partial^2}{\partial y^2} \right) \left(\frac{\partial \phi}{\partial z} \right) + \frac{\partial^2 \phi}{\partial t^2} - [g - A \cos(\omega t)] \frac{\partial \phi}{\partial z} = 0, \quad \text{at } z = 0. \quad (1.12)$$

In the following we show that both the surface deformation and the potential function are governed by the Helmholtz equation with the Neumann boundary condition.

Surface deformation. First, from equations (1.8b) and (1.9) it follows that $\partial^2 \zeta / \partial t \partial \mathbf{n} = 0$ at any point on the curve C bounding the surface (figure 1.3), and therefore $\partial \zeta / \partial \mathbf{n} = \partial \zeta / \partial \mathbf{n}|_{t=0} = 0$. The latter fact is significant as it suggests the angle of contact remains 90° throughout the time. Second, assuming that the temporal and spatial dependence can be separated in the surface deformation $\zeta(t, x, y)$, in equation (1.10) it can be replaced with $a(t)\zeta_0(x, y)$, and after dividing the equation by $a(t)\zeta_0(x, y)$, we arrive at:

$$\frac{\sigma}{\rho \zeta_0} \left(\frac{\partial^2 \zeta_0}{\partial x^2} + \frac{\partial^2 \zeta_0}{\partial y^2} \right) + \frac{1}{a(t)\zeta_0(x, y)} \frac{\partial \phi}{\partial t} \Big|_{z=0} - [g - A \cos(\omega t)] = 0. \quad (1.13)$$

As the first term above does not depend on time; separation of variables leads to $\frac{1}{\zeta_0} \left(\frac{\partial^2 \zeta_0}{\partial x^2} + \frac{\partial^2 \zeta_0}{\partial y^2} \right) = -k^2$. Hence, ζ_0 satisfies the Helmholtz equation with the Neumann boundary condition:

$$\left(\frac{\partial^2}{\partial x^2} + \frac{\partial^2}{\partial y^2} + k^2 \right) \zeta_0 = 0 \quad \text{on } z = \zeta, \quad (1.14a)$$

$$\frac{\partial \zeta_0}{\partial \mathbf{n}} = 0 \quad \text{on } C. \quad (1.14b)$$

Potential function. With the linearized kinematic boundary condition, cf. equation (1.9), the boundary-value problem governing potential function (1.8a-c) is now completed:

$$\nabla^2 \phi = 0 \quad z \geq \zeta(t, x, y), \quad (1.15a)$$

$$\frac{\partial \phi}{\partial z} = \frac{\partial \zeta}{\partial t} \quad \text{at } z = 0, \quad (1.15b)$$

$$\frac{\partial \phi}{\partial \mathbf{n}} = 0 \quad \text{on } S, \quad (1.15c)$$

$$\frac{\partial \phi}{\partial z} = 0 \quad \text{at } z = h, \quad (1.15d)$$

and is considered to be of the Laplacian form with the Neumann boundary conditions. The solution exists ¹ and is unique (up to a constant) if ²

$$\oint_S \mathbf{n} \cdot \nabla \phi \, dS = \oint_S \frac{\partial \phi}{\partial \mathbf{n}} \, dS = 0 \quad (1.16)$$

where S is the surface bounding the fluid volume. This condition is clearly satisfied on S and $z = h$, whereas on $z = 0$ it reduces to:

$$\oint \frac{\partial \phi}{\partial \mathbf{n}} \, dS = \oint \frac{\partial \phi}{\partial z} \, dS = \iint \frac{\partial \zeta}{\partial t} \, dx \, dy = \frac{\partial}{\partial t} \iint \zeta \, dx \, dy \quad \text{on } z = 0. \quad (1.17)$$

The last equality holds because $dx \, dy$ represents the area element of area in the plane $z = 0$ and hence is not a function of time. Accordingly, $\zeta \, dx \, dy$ denotes the element of volume displaced with respect to the $z = 0$ plane and therefore its summation over the surface is zero, i.e. $\iint \zeta \, dx \, dy = 0$.

Hence, the consistency condition is satisfied.

¹To allow the existence of a solution, the boundary-value problem should be self-consistent (Barton (1989), chapter VI): $\int_V \nabla^2 \phi \, dV = \int_V \nabla \cdot \nabla \phi \, dV = \oint_S \mathbf{n} \cdot \nabla \phi \, dS$, where the last equality followed from the divergence theorem. Since $\nabla^2 \phi = 0$, then it is required that $\oint_S \mathbf{n} \cdot \nabla \phi \, dS = 0$.

²The proof of the uniqueness is straightforward as follows. Assume that there exist two solutions ϕ_1 and ϕ_2 each satisfying the Laplace equation $\nabla^2 \phi_1 = \nabla^2 \phi_2 = 0$, and the Neumann boundary conditions: $\frac{\partial \phi_1}{\partial \mathbf{n}} = \frac{\partial \phi_2}{\partial \mathbf{n}}$ on S . Then for the function $\psi = \phi_1 - \phi_2$ it is evident that $\nabla^2 \psi = 0$ and $\frac{\partial \psi}{\partial \mathbf{n}} = 0$ on S . Now if one defines the volume integral $J = \int_V (\nabla \psi)^2 \, dV$, then $J > 0$ unless $\psi = \text{const}$. Following the identity $\nabla \cdot (\psi \nabla \psi) = (\nabla \psi)^2 + \psi (\nabla^2 \psi)$ and the fact that $\nabla^2 \psi = 0$, it is clear that $(\nabla \psi)^2 = \nabla \cdot (\psi \nabla \psi)$. Therefore, $J = \int_V (\nabla \psi)^2 \, dV = \int_V \nabla \cdot (\psi \nabla \psi) \, dV = \oint_S \psi \mathbf{n} \cdot \nabla \psi \, dS = \oint_S \psi \frac{\partial \psi}{\partial \mathbf{n}} \, dS = 0$ because $\frac{\partial \psi}{\partial \mathbf{n}} = 0$ on S . Hence $J = 0$ which is only possible if $\psi = \text{const}$, establishing that ϕ is unique up to a constant.

Now that the existence and uniqueness of the solution are established, ϕ needs to be determined as follows. In order to keep the solution manageable analytically, separation of variables has to be enforced (Barton, 1989), i.e. $\phi(t, x, y, z) = \phi_0(x, y)\phi_1(z)\phi_2(t)$. Performing similar analysis for equation (1.12) as done for the case of surface deformation for equation (1.10) leads to $\frac{1}{\phi_0} \left(\frac{\partial^2 \phi_0}{\partial x^2} + \frac{\partial^2 \phi_0}{\partial y^2} \right) = -k^2$ and with the boundary condition $\frac{\partial \phi}{\partial \mathbf{n}} = 0$ on C , it can be concluded that ϕ_0 also satisfies Helmholtz equation with the Neumann boundary condition:

$$\left(\frac{\partial^2}{\partial x^2} + \frac{\partial^2}{\partial y^2} + k^2 \right) \phi_0 = 0 \quad \text{on } z = \zeta, \quad (1.18a)$$

$$\frac{\partial \phi_0}{\partial \mathbf{n}} = 0 \quad \text{on } C. \quad (1.18b)$$

Theorem 11.5.2 in Jost (2013) assures that ζ_0 and ϕ_0 satisfying equations (1.14) and (1.18), respectively, can be expanded in terms of complete orthogonal set of eigenfunctions $S_l(x, y)$ ³

$$\left(\frac{\partial^2}{\partial x^2} + \frac{\partial^2}{\partial y^2} + k_l^2 \right) S_l(x, y) = 0, \quad (1.19)$$

and therefore, ζ and ϕ can be written as

$$\zeta(t, x, y) = \sum_{l=0}^{\infty} a_l(t) S_l(x, y), \quad (1.20a)$$

$$\phi(t, x, y, z) = \sum_{l=0}^{\infty} b_l(t) S_l(x, y) \phi_l(z). \quad (1.20b)$$

Substitution of equation (1.20b) into (1.15a) and applying (1.19) yields $\frac{d^2 \phi_l}{dz^2} = k_l^2 \phi_l$. It follows simply from equations (1.15b) and (1.15d) that $\phi_l'(0) = 1$, $\phi_l'(h) = 0$, $b_l(t) = \frac{da_l}{dt}$, and therefore,

$$\phi(t, x, y, z) = - \sum_{l=1}^{\infty} \frac{da_l(t)}{dt} \frac{\cosh[k_l(h-z)]}{k_l \sinh(k_l h)} S_l(x, y) + H(t). \quad (1.21)$$

³The theorem indicates that the eigenvalue problem $\nabla^2 \varphi + k\varphi = 0$ on Ω with $\frac{\partial \varphi}{\partial \mathbf{n}} = 0$ on $\partial\Omega$ has countably many eigenvalues $0 = k_0 \leq k_1 \leq \dots \leq k_n \leq \dots$ (with $\lim_{n \rightarrow \infty} k_n = \infty$), corresponding to the eigenfunctions φ_i that satisfy $\frac{\partial \varphi_i}{\partial \mathbf{n}} = 0$ on $\partial\Omega$ and any vector in the corresponding space can be expanded in terms of these eigenfunctions.

Due to the volume of the fluid being conserved, the amplitude of the zero-mode $a_0(t)$ remains constant, and with the z-coordinate's origin adjusted to be at the undisturbed flat surface, $a_0(t)$ can be set to zero. Accordingly from equation (1.10) it can be concluded that $H(t) = \text{const}$ and can be set to zero. Substituting equations (1.20a) and (1.21) into equation (1.10) reveals:

$$\sum_{l=1}^{\infty} \frac{S_l(x, y)}{k_l \tanh(k_l h)} \left[\frac{d^2 a_l(t)}{dt^2} + k_l \tanh(k_l h) \left(\frac{k_l^2 \sigma}{\rho} + g - A \cos(\omega t) \right) a_l \right] = 0, \quad (1.22)$$

since $S_l(x, y)$ are linearly independent, each mode amplitude satisfies

$$\frac{d^2 a_l(t)}{dt^2} + k_l \tanh(k_l h) \left[\frac{k_l^2 \sigma}{\rho} + g - A \cos(\omega t) \right] a_l = 0. \quad (1.23)$$

Equation (1.23) reduces to the standard form of Mathieu's equation by setting $T = \frac{1}{2}\omega t$

$$\frac{d^2 a_l(t)}{dT^2} + [p_l - 2q_l \cos(2T)] a_l = 0, \quad (1.24)$$

where

$$p_l = \frac{4k_l \tanh(k_l h)}{\omega^2} \left(\frac{k_l^2 \sigma}{\rho} + g \right), \quad q_l = \frac{2k_l A \tanh(k_l h)}{\omega^2}. \quad (1.25)$$

For the case of *free vibration* $A = 0$, from equation (1.23) the dispersion relation found to be

$$\omega_0^2 = [g k + (\sigma/\rho) k^3] \tanh k h. \quad (1.26)$$

On the rectangular domain of length L_x and width L_y , the eigenfunctions $S_l(x, y)$ due to excitation of the single mode $l = (m, n)$ can be determined explicitly; from $\frac{\partial \zeta}{\partial n} = 0$ it is deduced that:

$$\frac{\partial S_l}{\partial y} = 0 \quad \text{on } y = 0, y = L_y, \quad (1.27a)$$

$$\frac{\partial S_l}{\partial x} = 0 \quad \text{on } x = 0, x = L_x, \quad (1.27b)$$

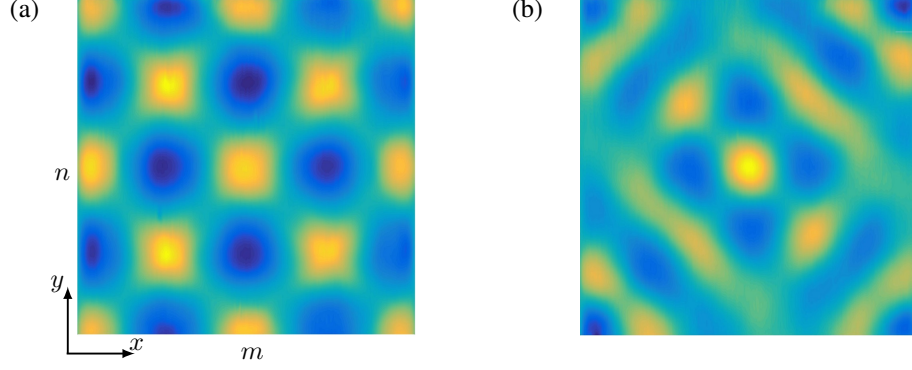


Figure 1.4: Top view of Faraday waves: (a) mode $(m, n) = (4, 4)$, (b) superposition of modes $(6, 4)$ and $(4, 6)$.

thus from $\left(\frac{\partial^2}{\partial x^2} + \frac{\partial^2}{\partial y^2} + k_l^2\right) S_l(x, y) = 0$ it is concluded that:

$$S_l = \cos\left(\frac{m\pi x}{L_x}\right) \cos\left(\frac{n\pi y}{L_y}\right), \quad k_l^2 = \pi^2 \left(\frac{m^2}{L_x^2} + \frac{n^2}{L_y^2}\right). \quad (1.28)$$

In summary, it has been shown that in the linear approximation, the contribution of each mode to the surface deformation, in a rectangular container, is represented by the product of two cosine functions, cf. equation (1.28), and the corresponding amplitude is governed by Mathieu's equation, with the natural frequency determined from capillary-gravity waves dispersion relation, cf. equation (1.26).

Faraday waves exhibit patterns of a large variety of shapes and symmetries depending on the fluid properties, layer depth, driving and boundary conditions (Douady & Fauve, 1988; Gollub, 2006). In the rectangular domain of length L_x and width L_y , the surface deformation $\zeta(t, x, y)$ due to excitation of the single mode $l = (m, n)$ corresponding to the wavenumber $\mathbf{k}_l = (k_x^m, k_y^n)$ has the form:

$$\zeta(t, x, y) = a_l(t) S_l(x, y); \quad a_l = C(\tau) \cos[\omega_0 t + \phi(\tau)], \quad S_l = \cos(k_x^m x) \cos(k_y^n y), \quad (1.29)$$

in which $k_x^m = \pi m / L_x$ and $k_y^n = \pi n / L_y$, while $C(\tau)$ and $\phi(\tau)$ denote the Faraday wave amplitude and phase varying on a slow timescale $\tau \gg \omega_0^{-1}$. The convention to denote the pattern as (m, n) on a rectangular domain, cf. figure 1.4, comes from the number of half-wavelengths formed in

the corresponding (x, y) directions as coined in the work of [Simonelli & Gollub \(1987\)](#), who first applied it to Faraday waves in consonance with [Benjamin & Ursell \(1954\)](#) and in analogy with other two-dimensional instabilities.

Chapter 2

Faraday waves on time-dependent domains

The idea of the present study is to address experimentally the following key questions on the dynamics of 2D systems: (i) How may the spatial structure of an existing pattern be affected by the time-evolution of the domain? In particular, we will consider three regimes of domain evolution with varying time-dependencies – shrinkage, growth, and oscillations – with the goal to understand destruction of one pattern and formation of another through phase-slip phenomena. An interesting related question is whether domain shrinkage or growth leads to stabilization of a pattern that is otherwise unstable in the time-independent domain case or vice versa. (ii) What is the response of both mode numbers (m, n) of 2D patterns to domain deformation in one direction only? (iii) What are the key differences expected in pattern formation on time-dependent domains with and without dilution and convective effects (local volume change and translation with the domain flow, respectively)? The latter regime can be achieved by draining the liquid from the tank thus affecting the dispersion relation (1.26) through the variation of the liquid layer depth h as opposed to changing the horizontal domain size L_x .

With the above scope, a guide to the paper will be useful. Section 2.1 discusses the Faraday assembly and the visualization/measurement technique. Section 2.2 sets the stage for our study of time-dependent domain effects by conducting a series of experiments on a time-fixed domain first, in particular for the purpose of validating the capabilities of the setup and, most importantly, providing a road map for the present study. Section 2.3 reports the results of investigations on time-dependent domains starting with an experimental observation of phase-slip phenomena (§2.3.1) and pattern

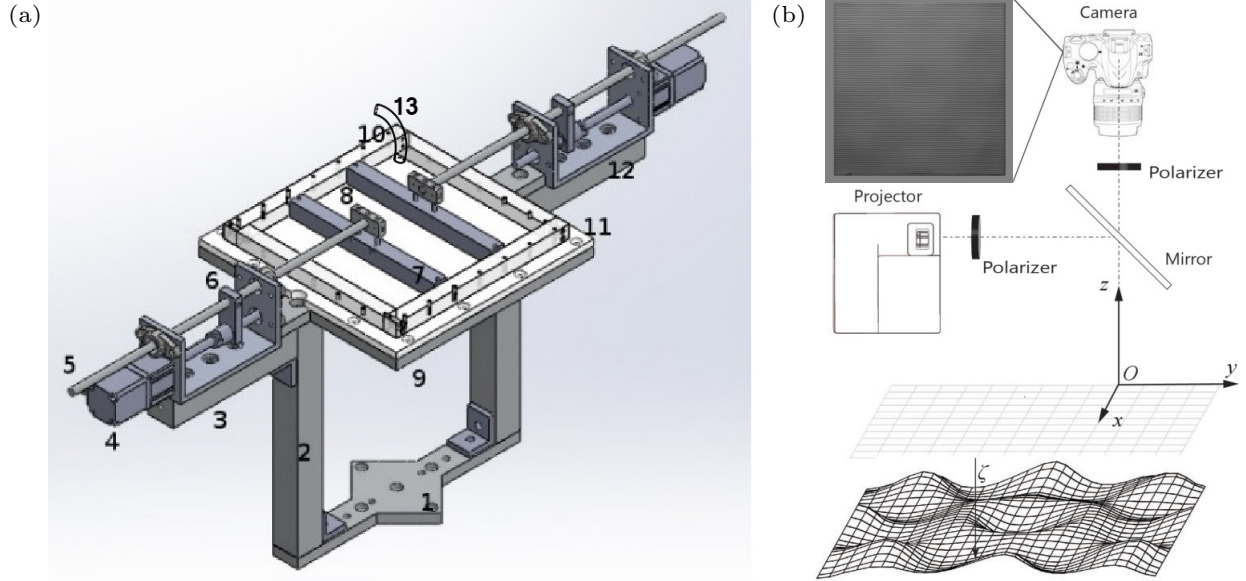


Figure 2.1: (a) The Faraday waves assembly: 1 – base plate, 2 – vertical column, 3 – horizontal column, 4 – stepper motor, 5 – shaft, 6 – traveling nut connector, 7 – moving walls, 8 – wall connector, 9 – container support rim, 10 – parallel container walls, 11 – container bottom, 12 – U-channel, 13 – injection tube. (b) Optical setup. The captured digital image corresponds to the rendered pattern at the bottom; the top view of the colored rendered pattern, i.e. modes $(2, 6) + (6, 2)$, can be found in figure 2.4a.

transformations (§2.3.2), followed by a study of the reversibility of the domain shrinkage-growth process (§2.3.3). The subsequent parts of this section examine the effects of wall speed (§2.3.4), initial conditions (§2.3.5), and wall oscillations (§2.3.7) on the pattern structure. The section is completed by studying Faraday waves in a draining water tank (§2.3.8). The conclusions of the presented study are drawn in §2.4 by reviewing the key findings and posing open questions.

2.1 Experimental setup and procedure

2.1.1 Faraday waves apparatus

The experimental setup should be able not only to produce Faraday waves, but also to change the container dimensions in a time dependent fashion, as well as to measure the characteristics of the formed patterns. Different components of the designed Faraday assembly presented in figure 2.1a are mounted and function independently on top of the electrodynamic shaker, Labworks ET-139. The liquid is housed in a container with a transparent bottom and four sidewalls, so that inner tank

dimensions are $150 \times 150 \times 12.7 \text{ mm}^3$ without moving walls. As the flatness of the brim plays a crucial role in the formation of Faraday patterns (Douady, 1990; Bechhoefer *et al.*, 1995), the tank bottom is made of Plexiglas with the flatness precision of 0.05 mm when mounted. Both fixed and moving container walls are machined from Delrin.

The shaker is driven through a linear amplifier, Labworks PA-138. The force rating of the vibration system is 334 N; thus, given the 3.2 kg weight of our assembly and the fluid, the maximum achievable acceleration is about 10 g, well above the range of accelerations $0.8 - 1.9 \text{ m s}^{-2}$ used throughout all the experiments to produce Faraday waves. The acceleration signal is generated by the LabView software and then converted to an analog voltage by the Data Acquisition Device (DAQ). The actual acceleration of the container is measured by Brüel and Kjær 4513 accelerometer with accuracy of $\pm 1\%$, interfacing with the 1704-A-001 (Brüel and Kjær) signal conditioner before being sent to the DAQ for readout and a real-time signal processing with LabView. The latter, using a fitted sinusoidal curve, determines the actual frequency and amplitude of the signal and then compares to the input driving signal showing the frequency difference within 0.02% and the residual RMS amplitude never exceeding 1.0% of the driving RMS amplitude thus confirming the absence of stray mechanical harmonics.

Since the shaker is the main source of the heat, it is equipped with a cooler pump blowing air through its interior, which in turn helps to maintain the environment temperature unaltered – this, in particular, is important for the constancy of surface tension, otherwise affecting the Faraday waves as per the dispersion relation (1.26). Direct measurement of the temperature with a thermocouple placed at the closest point of the assembly to the shaker, i.e. the aluminum base plate in figure 2.1a, showed the temperature variation between $22.7 - 22.9^\circ$ during a 4-hour long experiment. All the above three setup characteristics – the controlled shaker waveform and apparatus temperature as well as flatness of the container brim and bottom – are crucial for the ability to generate reproducible Faraday waves.

The horizontal domain size can be controlled in a time-dependent fashion according to the prescribed laws $x_1(\tau_w)$ and $x_2(\tau_w)$, cf. figure 2.2a, where τ_w is a long time scale, compared to that of



Figure 2.2: (a) A cross-section of a rectangular container with two moving walls on the left and right; the entire container moves vertically in time. Top (b) and side (c) views of static contact angle near a corner of the domain; the length scale is set by the thickness of the wall being 12.7 mm.

the vertical oscillations. While the locations x_1 and x_2 are independent, in our experiment their implemented motion, controlled by two linear actuators, is symmetric with respect to the centerline of the vessel, i.e. $x_1 = -x_2$. The assembly on each side of the domain, cf. figure 2.1a, is comprised of sliding wall, wall connector, shaft, nut connector, leadscrew, and stepper motor (NEMA 11), which converts the rotatory motion of the stepper motor into linear motion. The linear actuators enable the walls to travel at speeds between 0 and 45 mm s^{-1} while keeping their center of mass over that of the shaker and providing unobstructed optical access from below and above the container. Each stepper motor is driven by a ViX controller, Parker-Hannifin ViX 250IM, which in turn is controlled with Easi-V software. We study the free surface between the movable walls, ignoring the one outside thereby defined domain, cf. figure 2.2a.

Considering that the wall motion may generate sloshing waves, great care must be taken to assure that the Faraday waves are not perturbed; thus, the time scale τ_w of horizontal motion should be necessarily longer than that of the vertical vibration $t \ll \tau_w$. In our experiments, the frequency of the vertical motion is two orders of magnitude greater than the one of the prescribed horizontal motion $f_w = \tau_w^{-1} < 0.07 \text{ Hz}$. At this frequency f_w the amplitude C_w of the wave induced by wall motion (Ursell *et al.*, 1960) is only $C_w = 0.01A_w$, where A_w is the amplitude of the wall motion (see further discussion in §2.3.7), assuring that no sloshing interferes with Faraday waves. Also, to keep the fluid layer depth constant, the moving sidewalls do not reach the bottom of the container, i.e. there exists a clearance of about 2 mm allowing unobstructed flow underneath the walls and not affecting Faraday waves, cf. Appendix 2.A.

A few further comments need to be made about water as a working fluid since some practical limitations naturally arise. Namely, when water is exposed to air, it becomes prone to contamination leading to surface tension gradients over the free surface, which in turn complicates the interpretation of the experiments as discussed by [Bechhoefer *et al.* \(1995\)](#). While we added Titanium Dioxide TiO_2 to water for the visualization purpose (§2.1.2), this chemical neither introduces any surface film effects nor modifies the shear viscosity and surface tension ([Przadka *et al.*, 2011](#)); the latter was maintained at the value $71 \pm 1 \text{ mN m}^{-1}$ throughout the experiment with the temperature of the room held constant at $23^\circ \pm 0.5^\circ \text{ C}$. As a result, based on Young's equation the contact angle is not modified either, which in the static case with and without TiO_2 was measured to 57.5° and 59.5° , respectively. The use of the same material for manufacturing both fixed and moving container walls guaranteed a uniform contact angle over the entire perimeter. Given the partial wetting, no noticeable capillary rise near the container corners was observed in the static case as verified directly by projecting a fine grating pattern, cf. figures 2.2b and 2.2c; in the dynamic case, similarly, no significant distortion of the contact line takes place.

Also, when water is used it can be expected that the system would be sensitive to possible evaporation and thus water layer depth changes ([Douady, 1990](#)). Indeed, through the preliminary experiments, we observed that Faraday waves – especially in the patterns competition regime – are sensitive to the depth of water as per the dispersion relation (1.26). Thus, the water level was kept constant at $h = 12 \pm 0.1 \text{ mm}$ by utilizing a syringe pump, PHD ULTRA Harvard apparatus, to inject water outside the moving walls (figure 2.1a) at the same rate as the evaporation rate determined for the given experimental conditions in the lab, i.e. $42 \mu\text{l min}^{-1}$.

2.1.2 Visualization and measurement technique

To quantitatively study Faraday waves, characterization of their global spatial structure and time evolution $z = \zeta(t, x, y)$ is needed, cf. figure 2.1b, with appropriate spatial and temporal resolutions as per the following requirements. First, the technique should be global, i.e. able to measure the interface deformation over the interrogation area of at least $150 \times 150 \text{ mm}^2$. Second, the minimum

required accuracy is 0.05 mm, as limited by the measured meniscus waves amplitude in the center of the tank in the range 0.05 – 0.2 mm given that the meniscus can move along the sidewall up to ~ 0.7 mm (cf. Appendix 2.B). This enables detection of the flat surface as precise as possible while studying the phase-slip phenomena and thresholds to instability. Third, although throughout the experiment generating waves with large amplitudes is avoided to minimize the nonlinear effects and splashing (over the container edge), still the visualization technique should be able to measure relatively large amplitude waves $\simeq 3$ mm observed under certain conditions. Forth, the temporal resolution should be reasonably fine, i.e. the sampling frequency must be at least 5 to 10 times of the driving frequency to be able to study the dynamical behavior of the system. The last, but not the least, requirement is for the technique to be non-invasive in order to avoid perturbing Faraday waves.

Various visualization and surface measurement techniques have been introduced in literature to study Faraday waves and yet most of them do not satisfy *all* the requirements above. For instance, Xia *et al.* (2012) used the diffusing light photography (Wright *et al.*, 1996), in which a diffusive agent – either suspended imaging particles or a small amount ($< 2\%$ in volume) of milk – is added to water such that the intensity of light transmitted is inversely proportional to the local depth allowing the surface elevation to be computed from the 2D intensity distribution. Such a technique works when the distance over which a light ray scatters through a large angle is larger than the surface deflection, but smaller than the liquid layer depth. Also, the highly accurate amplitude measurement method with the resolution of 10^{-2} mm introduced by Douady (1990), which is based on the image obtained from reflection of a thin laser beam at the specific point on the free surface, is local and useful for small wave amplitudes since the maximum slope at the specific point on the free surface that can be measured is limited by $1/\tan(\frac{1}{2}\vartheta)$, where ϑ is the angle between the incident laser beam and the vertical axis perpendicular to the surface. Thus, Douady (1990) had to use a separate technique (bicolor stroboscopy) to visualize the entire surface. More recently, a free-surface synthetic Schlieren method based on the analysis of the refracted image of a random dot pattern was offered

(Moisy *et al.*, 2009), but among its disadvantages are extreme sensitivity to slight vibrations and application to weak surface deformations only.

Hence, given our considerations and requirements listed above, we resorted to Fourier transform profilometry (FTP) – a single-shot optical profilometric measurement of surface deformation – which has been widely used to visualize and measure water surface waves (Maurel *et al.*, 2009; Cobelli *et al.*, 2009, 2011; Przadka *et al.*, 2011). Such a method is based on an optical system composed of a video projector displaying a grating pattern on the surface and a camera recording the reflection of this pattern from the free surface. The distorted grating pattern due to deformation of the surface is then recorded and compared to the reference image (undistorted grating pattern on the flat surface) in order to produce a phase-shift map – the difference between phases of light intensity at each pixel in the two images – from which the height of the deformed surface is reconstructed through an equation relating the *phase difference* to the *object's height*. The biggest challenge experienced while applying this method to water surface is light reflection, which previously was partially treated by enhancing the water light diffusivity with the addition of TiO₂ (Cobelli *et al.*, 2009; Przadka *et al.*, 2011); however, a considerable amount of light reflection still remains.

In an effort to improve the accuracy and applicability of the method we came up with a common-optical axis geometry implementation of FTP along with an appropriate phase-height relation, cf. appendix 2.D. In our experimental setup, a digital video projector (ViewSonic PJD7820HD) with a resolution of 1920×1080 pixel² projects the sinusoidal fringe pattern on the water surface with interrogation area up to 300×170 mm². A DSLR camera (Nikon D5200) with the resolution of 6000×4000 pixel² provides a record of the phenomena. The images are captured in raw (Nikon electronic) format to prevent unwanted post-processing through the built-in algorithm in the camera, which would reduce the size and quality of the image because we need to extract the actual, not manipulated, intensities. Then they are developed into raw tagged image file format (TIFF) prior to entering the signal processing algorithm. To make the common-optical axis geometry possible, i.e. bringing the camera and projector optical axes together, a semi-transparent mirror (standard 50/50 beam splitter) positioned precisely at 45 degrees, with respect to the projector and/or camera

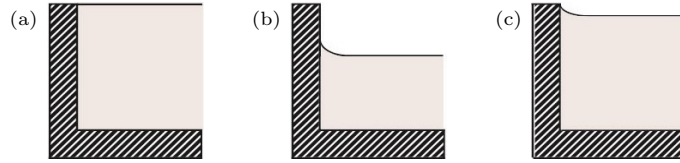


Figure 2.3: Experimental contact line conditions: (a) pinned, (b) non-pinned, and (c) semi-pinned.

axis, was employed. Furthermore, we introduced a proper filtering of light by implementing two linear polarizers – in front of the camera and projector, cf. figure 2.1b – to remove the reflections remaining after the addition of TiO_2 . This technique was calibrated and proved to be capable of detecting and reconstructing the surface deformation for the interrogation area of $300 \times 170 \text{ mm}^2$ with the vertical resolution of 0.05 mm and horizontal resolution of 0.08 mm, therefore providing an order of magnitude improvement in the accuracy compared to literature (Cobelli *et al.*, 2009; Przada *et al.*, 2011).

2.2 Results: Faraday waves on time-fixed domain

The experiments reported in this section serve to (i) characterize the setup in order to demonstrate its capability in accurately capturing all the dynamical features of interest and (ii) develop a benchmark study of patterns behavior to provide the context and comparison with Faraday waves on time-dependent domains in §2.3. In particular, before embarking on experiments in time-dependent domains we need to identify proper range of frequencies to work with. Due to high sensitivity of the Faraday wave system, extreme caution must be taken in selecting proper contact line conditions, especially if one tries to enhance understanding of dynamical phenomena observed experimentally by making comparisons with the available stability theory on time-dependent domains (Knobloch & Krechetnikov, 2014, 2015; Krechetnikov & Knobloch, 2017). This effort led us to the regime of Faraday waves, which has not been extensively studied despite intimate connection to the classical theory of Benjamin & Ursell (1954).

2.2.1 Boundary conditions

Early experimental works sought to disentangle the role of boundary conditions from the physics in the bulk of the fluid as they were considered to be a hindrance in observation of Faraday waves (Douady, 1990; Bechhoefer *et al.*, 1995). According to Douady (1990) two types of boundary conditions for the free surface can be implemented based on the design of our setup. The first one is the *pinned* boundary (e.g. brimful) where the vessel is filled to the fullest $\zeta = 0$, thus preventing the emission of meniscus waves as the boundaries are pinned and the fully flat surface acts as the actual initial condition before vertical vibrations start (Douady, 1990), cf. figure 2.3a. The advantage of a pinned condition is that the patterns are not perturbed by the menisci and could be described approximately as the product of two sine waves $\sin(m\pi x/L_x) \sin(n\pi y/L_y)$, cf. Benjamin & Scott (1979) and Douady (1990). Implementing such boundaries in practice is very delicate as precise alignment of the walls and brim is required. Minor mechanical imperfections lead to the formation of meniscus waves (Bechhoefer *et al.*, 1995).

The second possible boundary condition is the *non-pinned* one, where the vessel is not filled completely, cf. figure 2.3b. For this boundary condition the theoretical treatment in the case of an inviscid fluid is rather straightforward leading to patterns as products of two cosines (1.29) (Benjamin & Ursell, 1954; Douady, 1990). A considerable disadvantage of this condition is that, as the contact lines are free to move, the imminent meniscus waves are emitted from the walls and perturb the excited patterns and potentially could mask the true threshold of each mode appearance. However, if the capillary length $\ell_c = (\sigma/\rho g)^{1/2}$ is negligible compared to the pattern wavelength, the effect of menisci is minimized and therefore the theory can be used as a reference point.

Using pinned boundaries is preferred as minimizing contact line mobility and meniscus waves effects is desirable. Our setup, with the pinned boundary condition – vessel filled to the edge of the walls – was able to produce sine patterns over the range of frequencies 7 – 100 Hz of interest to us without any observable menisci. However, our main objective of conducting experiments on time-dependent domains prevented us from using such boundaries: on a time-fixed domain, when the vessel is filled fully and vibrated vertically by starting from a flat surface with gradual increase

in driving amplitude, a transient wave (especially in the low range of frequencies) with an amplitude of several millimeters is formed, though decays quickly upon reaching the stable pattern (Simonelli & Gollub, 1989). This transient wave substantially disturbs the fluid domain boundaries by forcing the fluid to flow over the wall edges, which is enhanced by the walls motion thus perturbing the whole system. Hence, from an experimental point of view, boundaries cannot be kept fully pinned for all driving conditions. Such considerations led us to a compromise between pinned and non-pinned conditions by setting the waterline 0.7 mm below the wall edge (nearly brimful), thus limiting the meniscus motion, which hereafter will be referred to as *a semi-pinned* boundary condition, cf. figure 2.3c. Depending on driving frequency, it gives either sine or cosine type solutions. Below frequency 12.1 Hz modes are essentially quantized same as for the choice of the boundary conditions in Benjamin & Ursell (1954) due to the boundedness of the domain, which enables us to study the corresponding discernible stability curves (§2.2.2).

2.2.2 Road-map

In spatially unbounded (in the xy plane) systems, there is a continuous spectrum of modes available, while mode quantization is the signature of a finite-size domain (see Bechhoefer *et al.*, 1995). Detailed study of pattern formation on a time-dependent domain requires the mode to be far removed from adjacent modes. Since the infinite-domain regime is approximately accessible on any finite domain size if the driving frequency is high enough, we resorted to a lower range of frequencies to avoid this regime. Also pinned boundaries enhance the mode separation remarkably (Douady & Fauve, 1988; Douady, 1990; Bechhoefer *et al.*, 1995) in the sense that the overlap between the stability curves/tongue regions is reduced thus making the modes more distinct; employing semi-pinned boundaries in our setup contributes to mode separation as well.

Figure 2.4 presents the road map for our experiments, where frequencies ranging from 10 to 22 Hz were studied. We found that from 10 to 14 Hz cosine-type patterns are formed, cf. figure 2.4a, and from 18 to 22 Hz sine-type patterns are excited, cf. figure 2.4b; the range of intermediate frequencies 14 – 18 Hz corresponds to the mixed zone, where patterns could not be categorized

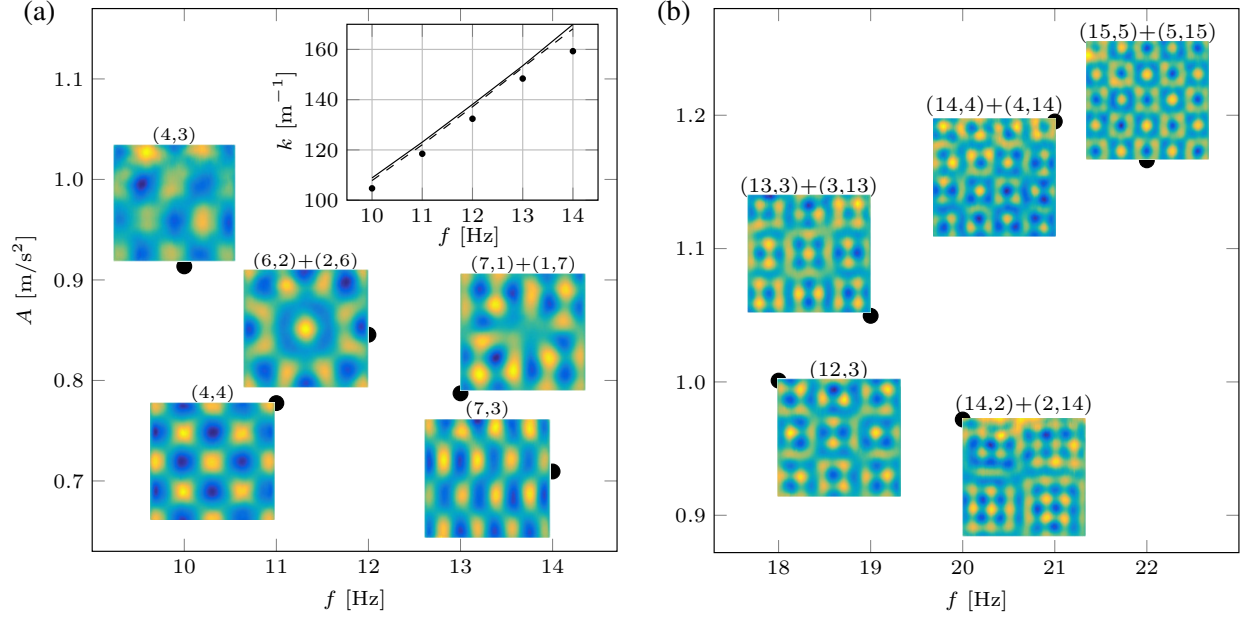


Figure 2.4: Road map on the square domain: for the studied range of frequencies 10–22 Hz (a) and (b) depict cosine and sine regimes, respectively. Each circle represents the measured threshold of vertical acceleration A of various modes at a given excitation frequencies f . The images depict the observed patterns over thresholds. The corresponding mode(s) number is stated on each pattern. Inset in (a) compares the measured wavenumber (dots) with the critical ones predicted from the viscous theory (solid line) by Kumar & Tuckerman (1994) and the inviscid theory (dashed line) by Benjamin & Ursell (1954).

as either sine or cosine type. Given that the wavenumber k depends on (m, n) through (1.29), in figure 2.4 one can see that with increase in excitation frequency $f = 2\pi/\omega$ patterns are formed in the order of increasing wavenumber k – this is in accordance with the monotonic behavior of the dispersion relation (1.26) in the cosine-regime; similar statement can be made about the sine regime based on the work of Benjamin & Scott (1979). Obviously, the dissipative effects do not affect the monotonicity of the wavenumber behavior, which indicates that they are not sufficiently strong in our experiments (Douady, 1990); see also the discussion in Appendix 2.C.

Altogether, observing both types of patterns was made possible by using semi-pinned boundary conditions, which can approximate either pinned and non-pinned boundary conditions depending on the driving frequency. Namely, in the cosine regime (lower mode number with a longer wavelength) the capillary length $l_c \approx 2.7$ mm is negligible compared to a typical wavelength, which is 20 times larger. Also, at these lower frequencies the wave amplitudes are higher, which is easy to see from the real Ginzburg-Landau equation (GLE) describing modulation with the amplitude $U_Q = (\mu - Q^2)^{1/2}$

and wavenumber Q of an excited spatially periodic pattern at the bifurcation parameter μ : clearly, at a fixed μ waves with lower modulation wavenumber Q would have a higher amplitude U_Q . These higher amplitude waves force the contact line to move hence being closer to non-pinned boundary conditions. On the contrary, in the sine regime wavelength is varied from 7 to 9 times of the capillary length which suggests that capillarity is not negligible. Furthermore, modes that are excited at higher frequencies, i.e. with a larger wavenumber, carry lower wave amplitude thus enabling nearly pinned boundary conditions. It should be noted that all the patterns studied throughout the experiments fall under the category of “square patterns” (Kudrolli & Gollub, 1996) based on their symmetries. Given the rectangular geometry of our container, the low viscosity fluid used, and the low range of frequencies and amplitudes of the single-frequency forcing, the formation of patterns with other symmetries such as hexagonal, stripes, quasi-crystalline is not expected.

The images in figure 2.4 depict the observed patterns at the corresponding frequencies close to the minimum acceleration required to excite a pattern on the tongue-like threshold curve. However, the non-monotonic behavior of $A(f)$ is the signature of the threshold curve in the low range of frequencies as shown both experimentally and theoretically by Batson *et al.* (2013) based on the work of Kumar & Tuckerman (1994). This observation is analogous to similar previous findings in the literature (e.g. Bechhoefer *et al.*, 1995; Batson *et al.*, 2013) and is mainly due to the mode separation, which allows each mode to have its tongue-like stability curve well-developed without being early terminated by surrounding stability curves, cf. figure 2.7. The above mentioned non-monotonic behavior is also contributed by the large fluid layer depth, which makes the stability curves less broad because with h much larger than the viscous boundary layer thickness $\delta_v \sim (\nu/\omega_0)^{1/2}$ (where ν is the kinematic viscosity) the dissipation at the bottom of the container is not strong enough to broaden the resonance tongue (Bechhoefer *et al.*, 1995).

Dissipation of each mode is proportional to the minimum acceleration required to excite a pattern (Douady, 1990). For example, in the sine regime, as illustrated in figure 2.4b, increase in the mode number n *transverse* with respect to the *direct* one m , e.g. $(m, n) = (14, 2)$ to $(14, 4)$, leads to an increase in the threshold and correspondingly in dissipation which was also observed in a square

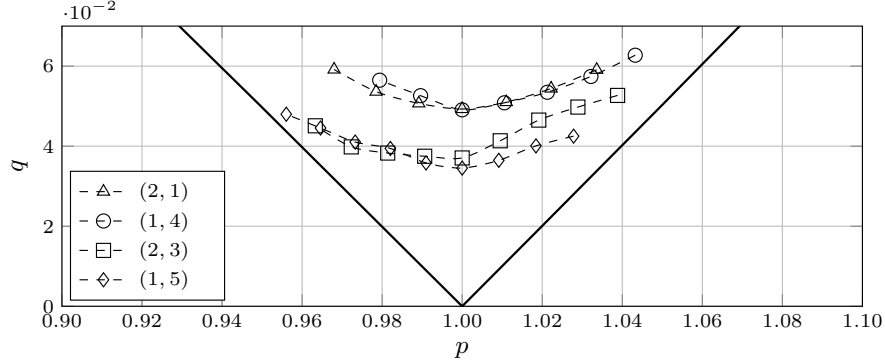


Figure 2.5: Stability curves for various modes, arranged in the increasing order of the total wavenumber (1.29), with the domain aspect ratio $R = 2.00$, where p and q are non-dimensional driving frequency and acceleration, respectively, cf. equation (2.1). Dotted lines represent the experimental data, while solid lines – the stability curve obtained from the linear inviscid theory (Benjamin & Ursell, 1954). The threshold curves in figures 2.4 and 2.5 were found starting from a flat surface at a fixed driving frequency and increasing the amplitude until a stable non-flat mode is reached, though Faraday waves are known to possess a hysteretic behavior in threshold values (Simonelli & Gollub, 1989; Craik & Armitage, 1995; Périnet *et al.*, 2016).

cell by Douady & Fauve (1988). This fact explains why the formed patterns tend to have a lower transverse mode number: due to their lower dissipation, they can mask the observation of other patterns with greater n and thus with larger dissipation. In the sine regime, the system gets closer to the infinite-domain limit due to higher frequencies as mentioned earlier. To keep the system in the quantized regime, the remaining experiments in the paper are restricted to the cosine patterns, which correspond to the classical inviscid theory of Benjamin & Ursell (1954); cf. comparison of the measured with theoretical wavenumbers in the inset of figure 2.4a.

2.2.3 Thresholds

Next, the measured stability curves for several modes on the domain of aspect ratio $R \equiv L_y/L_x = 2.00$ are presented in figure 2.5 in the parameter space of dimensionless driving frequency p and acceleration q :

$$p = 4\omega_0^2/\omega^2 \quad \text{and} \quad q = 2kA \tanh(kh)/\omega^2, \quad (2.1)$$

where A is the dimensional acceleration defined in figure 2.4. The deviation of the experimental results from the theoretical curve in figure 2.5 is due to the inviscid fluid approximation and infinitesimal wave amplitude assumed by Benjamin & Ursell (1954). While the viscous theory developed

by Kumar & Tuckerman (1994) could be used here as a reference for a better comparison with the experimental results, much improvement cannot be expected since this theory was developed on an infinite domain and thereby accounted for the damping in the bulk only. In our setup, however, the bulk dissipation estimated from viscous theory (Kumar & Tuckerman, 1994) in Appendix 2.C constitutes less than one-fifth of the total energy loss and, therefore, is subdominant to the damping caused by the moving contact lines. Nevertheless, for each mode, the tongue-like curve (see figure 2.7) is well established and terminated by the excitation of previous/next mode. Minimum of each curve corresponds to the resonance frequency and the minimum dissipation of the mode. Similar to the square domain case, these modes were observed in the order of increasing wavenumber k with the driving frequency f . This fact suggests that even in this smaller domain size the influence of walls is minimized in our experiment; otherwise, non-monotonic shifts in both wavenumbers and dissipation would be observed (Douady, 1990). The shifts observed in dissipations – e.g. mode (1, 4) appears to have higher dissipation than (1, 5) in figure 2.5 – can be explained similarly to the discussion in §2.2.2: the non-monotonic behavior of dissipation is the signature of the threshold curve at low frequencies (Batson *et al.*, 2013).

2.2.4 Symmetric mode interactions

Previous works on Faraday waves focused primarily on dynamical behaviors of the system such as bifurcations, mode interactions, and patterns competition which leads to chaos under certain conditions. For instance, Simonelli & Gollub (1989) in their experimental work on the interactions between two symmetric modes (m, n) and (n, m) naturally excited on a square domain were able to unravel the differences of the phase-space structure between square and slightly non-square containers. As it will be important for our study on time-dependent domains in the vicinity of pattern competition regime (see §2.3.3), we provide here a detailed study of the interactions between symmetric modes $(2, 6)$ and $(6, 2)$, as they are sufficiently away from excitation of adjacent modes, cf. figure 2.6. The interactions of such modes can reveal up to 16 fixed points, either stable or unstable, in the corresponding phase-space (Simonelli & Gollub, 1989). The discussion here parallels that from

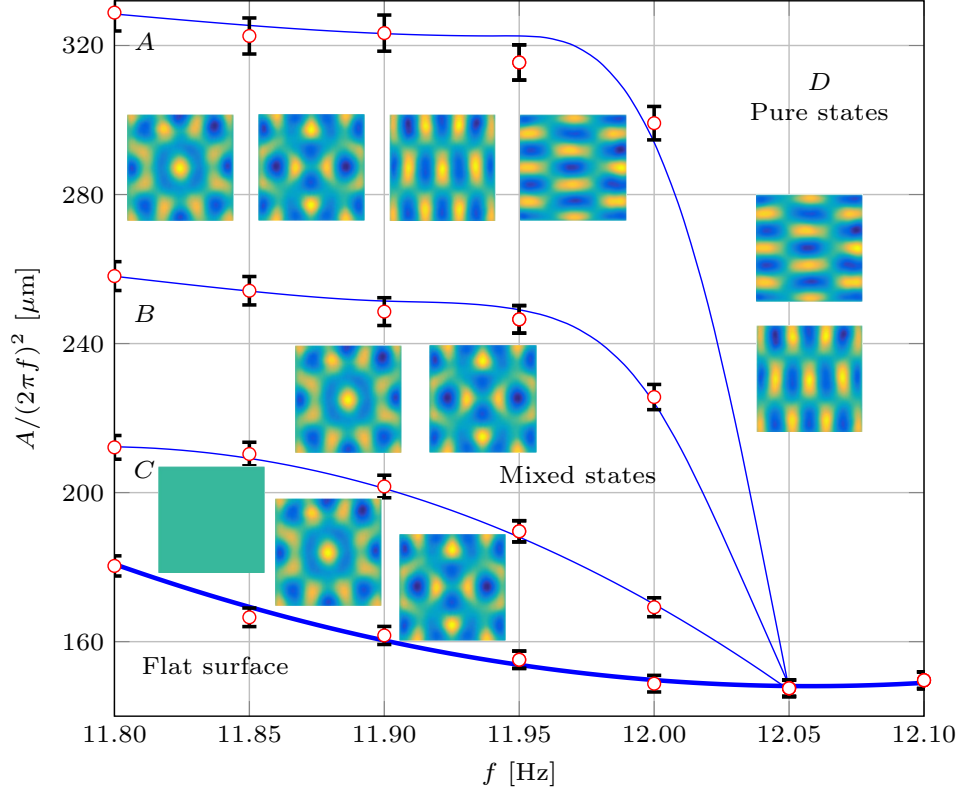


Figure 2.6: Amplitude-frequency diagram around mode $(6, 2)$ and its symmetric one $(2, 6)$ on a square domain. Four regions exist above threshold: mixed states B and pure states D , and two hysteresis ones A and C . The circles represent the experimental data with the error bars corresponding to the accuracy of the measurements; solid lines through the data sets are meant just to guide the eye. The images represent the typical patterns observed in the region and each can be formed in the corresponding region depending on the initial driving frequency and amplitude.

the above reference on the interaction of modes $(2, 3)$ and $(3, 2)$. Obviously (Simonelli & Gollub, 1989), excitation of a pure mode, e.g. $(2, 6)$, or interaction between two modes, e.g. $(6, 2) + (2, 6)$, corresponds to two fixed points, one with positive amplitude and the other with negative amplitude.

Referring to figure 2.6, four distinct regions are observed above the threshold. In region D either of the pure states, $(6, 2)$ or $(2, 6)$, is formed depending on the initial conditions. In region B mixed states, where two modes interact either in-phase $(6, 2) + (2, 6)$ or out of phase $(2, 6) - (6, 2)$, are found. Observation of both in-phase and out-of-phase combinations of these two modes is in accordance with the analytical analysis of Feng & Sethna (1989), who showed that on a square domain D_4 symmetry can be expected, i.e. if the in-phase interaction $(m, n) + (n, m)$ is allowed by the system then all the other combinations – in-phase $-(m, n) - (n, m)$ along with out-of-phase

$(m, n) - (n, m)$ and $-(m, n) + (n, m)$ – can be formed as well. However, [Simonelli & Gollub \(1989\)](#) claimed, based on the symmetry analysis, that when both m and n are odd or even (as in our case), only one of the in-phase or out-of-phase cases is possible which is one of the differences between their analysis and that by [Feng & Sethna \(1989\)](#). Even experimentally, [Simonelli & Gollub \(1989\)](#) observed only out-of-phase mixed state for even mode numbers, (0,4) and (4,0). Nevertheless, they pointed out that due to excitation of nearby modes such types of interactions could not be investigated thoroughly, which may have prevented them from detecting the in-phase combination. Later [Miles & Henderson \(1990\)](#) proved that symmetry analysis performed by [Simonelli & Gollub \(1989\)](#) is incomplete leading to differences from that of [Feng & Sethna \(1989\)](#). Regardless, as follows from figure 2.6, in our experiment we were able to observe both in- and out-of-phase mixed states in region B , where the mixed states are stable fixed points and the pure modes become saddle points.

Regions A and C are hysteretic: namely, if one starts from below the threshold curve at a frequency less than 12.05 Hz and increases the amplitude, in region C a flat surface would be observed, but if the starting point is in region B , then by decreasing the amplitude and entering region C mixed states would be expected. In region A eight stable fixed points are observed (both mixed and pure states), while in region C only five stable fixed points – the pure modes and the flat surface – exist. It should be noted that images in figure 2.6 depict the typical patterns observed in the region and each can be formed in the corresponding region depending on the initially chosen driving frequency and amplitude due to the hysteretic behavior.

Simultaneous excitation of two adjacent modes at the same values of physical parameters takes place in the overlap region of the two stability curves known as a pattern competition regime (dashed areas in figure 2.7), which is very common in Faraday wave phenomena as shown by [Ciliberto & Gollub \(1985b\)](#), whose phenomenological model is able to reproduce it. In this regime slow amplitudes of two different patterns are nonzero, non-equal and oscillate with different phases at a frequency smaller than the driving one by more than two orders in magnitude ([Ciliberto & Gollub,](#)

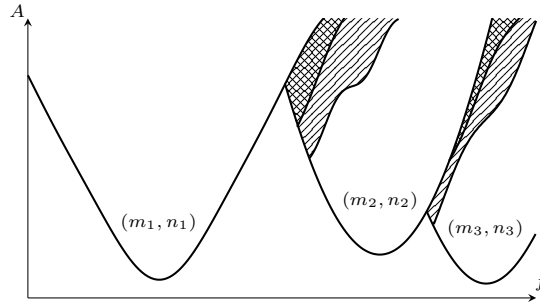


Figure 2.7: Schematic representation of figure 1.2 of Ciliberto & Gollub (1984) based on experiments on a circular domain with a radius of 6.35 mm. For each mode (m, n) solid curve denotes stability boundaries in the driving frequency f and acceleration A coordinates. Single/double dashed regions represent the periodic/chaotic pattern competition regimes of two adjacent modes.

1984, 1985a). An example of patterns observed in such a region in our experiments can be seen in figure 2.10c with the cycling of patterns illustrated by up-down arrows.

When performing experiments on a square domain we did not detect any time-dependent patterns as expected due to symmetry (Simonelli & Gollub, 1989). However, despite the fact that Simonelli & Gollub (1989) did not find any time-independent superposition (stable fixed point) of the two specific symmetric modes $(3, 2)$ and $(2, 3)$ in a nearly square cell, we found one specific case where the interaction between modes $(2, 6)$ and $(4, 4)$ was time-independent (stable fixed point) for the domain aspect ratio $R = 1.25$. Our observation is in agreement with the theory of Feng & Sethna (1989) which predicts that time-independent mixed-states can be expected in a non-square domain as well depending on the detuning frequency (the frequency difference from the resonance frequency of one of the modes) and the domain aspect ratio. Furthermore, for the specific case of interaction between modes $(3, 2)$ and $(2, 3)$, studied by Simonelli & Gollub (1989), the resonant frequencies between these modes differed by 1.5% whereas for modes $(4, 4)$ and $(2, 6)$ in our experiment the difference is only 1% which brings the stability curves closer. This makes the pattern competition region sizable enough (e.g. compared to the Simonelli & Gollub (1989) study) that any finite amplitude perturbations always present in real experiments are not sufficient to destabilize the superposition of modes $(2, 6)$ and $(4, 4)$.

The threshold curves in figure 2.6 were measured using a manual and simpler method than the automated scanning protocol based on the successive approximation applied by Simonelli & Gollub

(1988, 1989). At a fixed driving frequency a low driving amplitude, at which a non-flat surface first forms, is found by increasing it from below – this is assigned as an *upper* bound for the threshold. Then, the amplitude is decreased to arrive at the flat surface which yields yet another bound for the threshold termed as a *lower* one since it proves to be below the previously found upper bound. Finally, the amplitudes between upper and lower bounds are scanned with successively reduced positive and negative increments to identify possible hysteresis regions and to measure the instability boundaries.

2.2.5 Summary

Our search for a suitable Faraday waves regime led us to (i) moderate aspect ratio waves, i.e. with the wavelengths λ not significantly smaller than the domain size as opposed to the widely studied large aspect ratio regime (Kudrolli & Gollub, 1996; Binks & van de Water, 1997; Edwards & Fauve, 1994; Douady, 1990; Douady & Fauve, 1988) thus enabling pronounced square mode separation; (ii) but still considerably longer wavelengths compared to the capillary length l_c in order to minimize the effect of capillarity on the boundary conditions, since wetting details upset the Benjamin & Ursell (1954) theory leading to non-analytical modes (Benjamin & Scott, 1979; Douady & Fauve, 1988; Douady, 1990); and (iii) the use of low viscosity fluids in order to match to the classical theory (Benjamin & Ursell, 1954) amenable to transparent analytical treatment. The accuracy of the inviscid dispersion relation (1.26) applied to our case is demonstrated in the inset of figure 2.4a, which again indicates negligible role of menisci in the sense of deviation from the inviscid contact line conditions assumed by Benjamin & Ursell (1954). As demonstrated in Appendix 2.C, for our low driving frequency experiments using viscous theory (Kumar, 1996) would not modify the quantitative behavior of stability curve noticeably compared to that of inviscid one (Benjamin & Ursell, 1954; Batson *et al.*, 2013); thereby the linear inviscid theory can be used as the reference for our framework. Working in this classical regime, stripped of any complexities associated with appearance of hexagonal, quasi-periodic, quasi-crystal, and chaotic modes, is necessary to make the domain evolution effects distinguishable. Also, while above we used, in particular, the square

container to prove the accuracy of the experimental setup, due to the degeneracy of a square domain (Simonelli & Gollub, 1987), which makes the system very sensitive to small symmetry-breaking perturbations thus dramatically affecting the dynamics, we will study the domain evolution effects on rectangular domains only.

2.3 Results: Faraday waves on time-dependent domain

Given that previous theoretical efforts have mainly focused on dynamical properties on one-dimensional time-dependent domains (Knobloch & Krechetnikov, 2014, 2015; Krechetnikov & Knobloch, 2017), we now resort to the Faraday waves with the aim to understand the following key effects of domain deformation in 2D: *domain shrinkage-growth*, *domain evolution rate*, *domain oscillation*, and *interaction of domain time-dependence with a pattern competition regime*.

2.3.1 Phase-slip phenomena

Interpretation of the subsequent experimental results requires an understanding of the pattern destruction/formation mechanism known as a *phase-slip* which will be considered in detail in this section. On a time-fixed domain, given a phase-winding solution for the order parameter $U(\tau, \xi) = C(\tau, \xi) e^{-i\phi(\tau, \xi)}$ representing a spatially periodic pattern of amplitude $C(\tau, \xi)$ and phase $\phi(\tau, \xi)$ dependant on slow time $\tau = \epsilon^2 t$ and spatial $\xi = \epsilon x$ variables with $\epsilon \ll 1$, a cell in a particular x -direction can only be created or destroyed via the Eckhaus instability (Eckhaus, 1965). This happens at the locations where the order parameter $U(\tau, \xi)$ vanishes, $\text{Re } U(\tau, \xi) = \text{Im } U(\tau, \xi) = 0$, so that the phase-winding spiral intersects the x -axis (Langer & Ambegaokar, 1967) and hence the local spatial phase $\phi(\tau, \xi)$ is undefined, the event usually named as a *phase slip*. A phase slip inserts a new wavelength (cell) into the pattern after relaxation resulting in a new pattern with a shorter wavelength. When this wavelength falls in the Eckhaus-stable region, no further phase slips will be triggered.

Effects of the domain time dependence (Knobloch & Krechetnikov, 2014) can enter in the above picture in the following two ways. First, a gradual growth of the domain leads to repeated phase

slips as the pattern tries to keep its wavelength in the preferred, Eckhaus-stable, range. Second, since the phase slips occur on a fast timescale (the Eckhaus instability is subcritical), the number of phase slips, that occur before stability is restored, depends on the delay in triggering the instability. Local analysis reveals that compared to the time-independent domain case time dependence delays the occurrence of a phase slip when the domain is growing (Knobloch & Krechetnikov, 2014; Krechetnikov & Knobloch, 2017) and accelerates when the domain is shrinking. In the presence of dilution and convection, a modified near-critical amplitude equation of the GLE type for the order parameter U , derived by Krechetnikov & Knobloch (2017), possesses new solutions compared to the standard GLE, including spatially periodic solutions with a time-dependent wavenumber and spatially non-periodic (spatially localized) steady states. Also, the effect of the domain size oscillations is always destabilizing in the sense that the band of stable wavenumbers is always reduced, an effect that enhances with decreasing domain oscillation frequency.

A phase-slip event on a time-dependent domain is analyzed in figure 2.8 in the vicinity of the mode change from (3, 4) to (3, 3) as an example. With the surface deformation (1.29), the complex slow amplitude function is defined as:

$$U(\tau) = C(\tau) e^{-i\phi(\tau)}, \quad (2.2)$$

where the real amplitude C and phase ϕ depend on the slow timescale τ (Simonelli & Gollub, 1989; Feng & Sethna, 1989). On a time-dependent domain when the timescale of the wall motion τ_w is comparable with τ , one can expect that phase-slip would take place and the present pattern changes to another. To investigate such an event in detail, the real and imaginary parts of the complex slow amplitude $U(\tau)$ from the measurements need to be reconstructed as follows. First the total amplitude $a = C(\tau) \cos [\omega_0 t + \phi(\tau)]$ and the time stamps are extracted from each movie frame; then the amplitude envelope C , wave frequency ω_0 , and the phase ϕ are recovered (for each two fast cycles separately). Finally, $\text{Re } U$ and $\text{Im } U$ are determined based on (2.2).

Our visualization technique with a high sampling rate (§2.1.2) allowed us to recover the expected spiral behavior of U (Langer & Ambegaokar, 1967; Knobloch & Krechetnikov, 2015; Krechetnikov

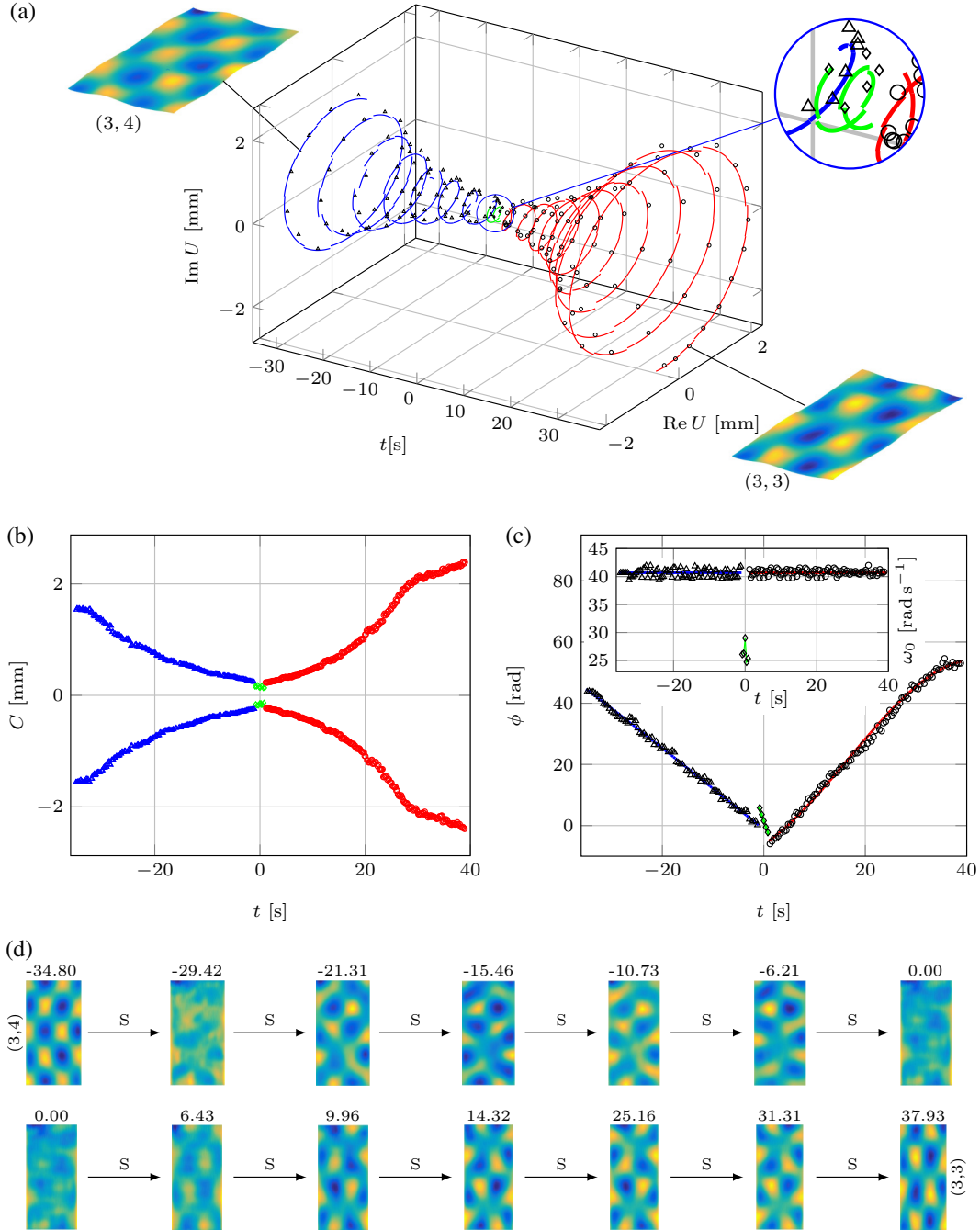


Figure 2.8: Phase-slip event on the time-dependent domain at the driving frequency 12.95 Hz, amplitude 1.4 m s^{-2} , and wall speed of 0.03 mm s^{-1} for the mode change from (3, 4) to (3, 3). Data recovered from the experiment is presented by different shapes: mode (3, 4) – triangle, mode (3, 3) – circles, and the phase-slip event – diamonds; solid lines are the fitted curves through the data. In (a) the complex amplitude U is presented, in which the imaginary and real parts are the slow amplitudes of the above modes, (b) the total amplitude envelope $C(t)$. Wave phase ϕ , and its frequency ω_0 are presented in (c) and the inset, respectively. (d) Representation of patterns evolution: the top row depicts the destruction of mode (3, 4) and bottom row shows formation of mode (3, 3). On the top of each mode the corresponding time at which the given pattern is observed is stated. The time origin is defined to be the mid-point of the phase-slip event.

& Knobloch, 2017) properly during the mode change as presented in figure 2.8a, where different symbols – triangles, circles, and diamonds – depict modes (3,4), (3,3), and the meniscus waves close to the phase-slip, respectively. In addition, solid lines represent curves fitted through the data. The mode change process on the shrinkage path, cf. figure 2.8a, starts from the stage at which mode (3, 4) is established with constant amplitude and frequency (the measured Faraday wave frequency is 40.67 rad s^{-1} , which is very close to 40.68 rad s^{-1} expected from (1.26), cf. inset of figure 2.8c). From the inset we can see that during the mode changing the wave frequency remains reasonably close to half of the driving frequency.

During the phase-slip event, in corroboration with the above theoretical considerations, both real and imaginary parts of the slow amplitude vanish, cf. figures 2.8a,b. It should be noted that the discernible small-amplitude $\approx 0.2 \text{ mm}$ meniscus waves at the phase-slip event, depicted by diamonds, are comparable to the accuracy of our measurement technique in this specific experiment (due to the lower resolution of the used fast camera). Because of that and the nature of these waves, we do not comment on the frequency/phase associated with these data points.

The phases recovered for modes (3, 4) and (3, 3) are presented in figure 2.8c. Curve fitting the data to polynomial functions we find $\phi_{(3,4)} = 2.89 \times 10^{-5} t^3 + 5.08 \times 10^{-4} t^2 - 1.32 t - 1.2072$ and $\phi_{(3,3)} = -0.0011 t^3 + 0.0532 t^2 + 1.0859 t - 6.1170$, in which all the coefficients in front of t^n have the unit of $[\text{rad s}^{-n}]$. With the introduction of the non-dimensional fast time $\bar{t} = \omega_0 t$, the phases read $\phi_{(3,4)} = 4.3 \times 10^{-10} \bar{t}^3 + 3.07 \times 10^{-7} \bar{t}^2 - 0.0326 \bar{t} - 1.2072$ and $\phi_{(3,3)} = -1.59 \times 10^{-8} \bar{t}^3 + 3.21 \times 10^{-5} \bar{t}^2 + 0.0267 \bar{t} - 6.1170$, from where the dominant terms are $\phi_{(3,4)} \approx -0.0326 \bar{t} - 1.2072$ and $\phi_{(3,3)} \approx 0.0267 \bar{t} - 6.1170$. Thus the non-dimensional slow time scale for the phase functions $\bar{\tau} = \epsilon^2 \bar{t}$ as defined in the GLE derivation (Cross & Hohenberg, 1993) yields $\epsilon_{(3,4)} = 0.18$ and $\epsilon_{(3,3)} = 0.16$. These values demonstrate a faster dependence on time compared to a stable Faraday pattern on a fixed domain (for example, see Ciliberto & Gollub (1985a), where $\phi(\bar{\tau}) = 0.008 \bar{\tau}$ or equivalently $\epsilon = 0.09$) implying that the pattern formation time scale τ on a time-dependent domain is enslaved by that of wall motion τ_w . Furthermore, the data in figure 2.8c indicate a jump in phase

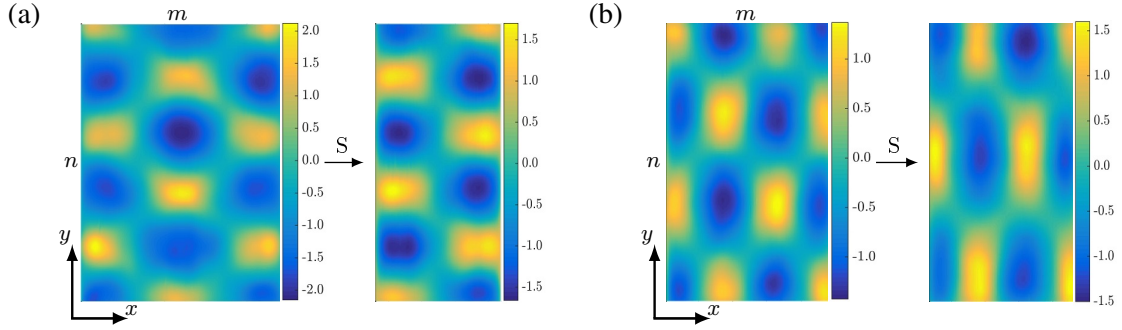


Figure 2.9: Examples of (a) a direct mode change $(2, 5) \rightarrow (1, 5)$ with the corresponding amplitude change $2.12 \rightarrow 1.7$ mm, and (b) a transverse one $(3, 3) \rightarrow (3, 2)$ with the amplitude change $1.37 \rightarrow 1.6$ mm, both observed during domain shrinkage (S) in the x direction. Scalebars are in mm.

about 1.95π confirming the theoretical understanding that the phase is undefined at the phase-slip and experiences a 2π jump.

At the fundamental level, the observed phase-slips correspond to phase transitions of the second kind, which are characterized by scale invariance at the critical point, i.e. possess conformal symmetry – invariance under local scale transformations, while preserving angles between any two vectors (Francesco *et al.*, 1997). In other words, the phenomena at the critical point become renormalizable. Naturally, in our context the only free surface that satisfies this scale-invariance requirement is *flat* thus explaining the peculiarity of the observed phase-slip phenomena when one pattern transforms into another.

2.3.2 Transverse instability

Given the detailed mechanism of the mode change on time-dependent domains we can now focus on patterns deformations during shrinkage and growth paths. As discussed in §2.1.1, the setup design allows us to modulate the domain size in a time-dependent fashion in one direction x . In the course of domain shrinkage or growth many mode changes occur; however, in this section we are specifically focused on the ones that either have the form of (m, n) to $(m \pm 1, n)$ or (m, n) to $(m, n \pm 1)$, henceforth named direct and transverse consecutive mode changes, respectively (cf. figure 2.9). Under the experimental conditions of driving frequency 12.95 Hz, amplitude 1.4 m s^{-2} , and wall speed of 0.03 mm s^{-1} on the domain shrinkage path $R = 1.25 \rightarrow 2.50$ a sequence of the

transverse mode changes $(3, 4) \rightarrow (3, 3) \rightarrow (3, 2) \rightarrow (3, 1)$ was found. The direct consecutive mode change $(m, n) \rightarrow (m \pm 1, n)$ was observed only in the case of $(1, 5) \leftrightarrow (2, 5)$ at the frequency of 11 Hz and amplitude of 1.32 m s^{-2} .

The first significant observation is that *regardless of whether the domain is growing or shrinking in the x direction, the system tends to change its mode transversely in the y direction* $(m, n) \rightarrow (m, n \pm 1)$, whence is referred to as a *transverse instability*. It appears that transverse instability is intrinsic to 2D systems. The direct consecutive mode change, (m, n) to $(m \pm 1, n)$, was highly rare and the single case $(2, 5) \rightarrow (1, 5)$ that we were able to find only happens above some specific wall speed threshold, which is remarkably different between the domain shrinkage and growth. Namely, during domain growth, the mode change $(1, 5) \rightarrow (2, 5)$ takes place for the wall speed above 0.18 mm s^{-1} , cf. figure 2.11c; the opposite mode change $(2, 5) \rightarrow (1, 5)$ shown in figure 2.11c occurs during domain shrinkage only with the wall speed above 2.4 mm s^{-1} , an order of magnitude greater. Below these speeds intermittent patterns, either modes $(2, 4)$ or $(4, 1)$, are formed. The explanation for such a difference between wall speed thresholds will be provided in § 2.3.4.

A basic reason for the observed transverse instability follows from the linear theory. Namely, since subharmonic Faraday waves have their frequency ω_0 fixed at half of the driving one ω , from the dispersion relation (1.26), where the wavenumber k is the modulus $k = \left(k_x^2 + k_y^2\right)^{1/2}$ of the 2D wavenumber $\mathbf{k} = (k_x, k_y)$, it follows that k must be fixed as well. With domain evolution in the x direction the wavenumber component k_x gets stretched as allowed by the presence of the domain dilution (Krechetnikov & Knobloch, 2017), and thus the wavenumber k_y in the y direction should adjust itself accordingly to keep the magnitude k constant leading to the transverse instability. Intrinsically, the mechanism for the transverse mode change is due to an Eckhaus instability: while the direct mode wavelength can be stretched/shrunk, the transverse one is pushed in the Eckhaus unstable region entailing a phase slip and hence a creation/annihilation of a cell (provided that this wavelength is closer to Eckhaus unstable region compared to the direct one).

Finally, it must be noted that the discussed here transverse instability differs from the transverse amplitude modulation instability, analyzed by Ezerskii *et al.* (1986) and Milner (1991), which is

zig-zag as opposed to longitudinal (Eckhaus). Namely, in the case of the 1D zig-zag instability bending of a roll at an unstable wavelength achieves a shorter (than the original) wavelength in the stable region (Hoyle, 2006), i.e. it is not possible to make up for a shortening of the original wavelength as it happens in our transverse instability. In the 2D situation, as shown by Hoyle (1993) on a square domain, the zig-zag instability is a direct equivalent of its 1D counterpart since at the leading order the zig-zag instability of each set of rolls is decoupled from the other one; hence the same wavelength shortening takes place. In our case, however, the mechanism driving the transverse instability originates from maintaining the 2D pattern wavenumber as dictated by the dispersion relation, though some wavenumber variation is allowed due to quantization on a finite domain (Tuckerman & Barkley, 1990).

2.3.3 Irreversibility

The difference in the behavior between domain growth and shrinkage observed in the previous subsection brings about the broader topic of *reversibility* of the sequence of patterns formed on the shrinkage versus growth path. Reversibility is understood here in the sense that patterns observed on the shrinkage and growth paths should be the same. For the experimental conditions of driving frequency 11 Hz, acceleration 1.32 m s^{-2} , and wall speed 0.15 mm s^{-1} , we studied domain shrinkage and growth between four distinct domain ratios: the observed patterns on each path shown in figure 2.10 reveal that, in general, *domain shrinkage-growth is not reversible*. For example, in the case $R = 1.25 \iff 2.50$, cf. figure 2.10a, the initial and final patterns are the same, but the shrinkage $(2,5) \rightarrow (3,3) \rightarrow (2,4) \rightarrow (1,5) \rightarrow (2,2)$ and growth $(2,2) \rightarrow (1,5) \rightarrow (0,0) \rightarrow (4,1) \rightarrow (2,5)$ paths are not the reverse of each other. Such an irreversibility can also be seen in figures 2.10b and 2.10c, while in figure 2.10d the paths are reversible. The latter exception stems from a very short (in space) path preventing the wavenumber to be shifted far away from that on the time fixed domain, so that we cannot expect many mode changes, especially in the low frequency regime in which mode separation is prominent.

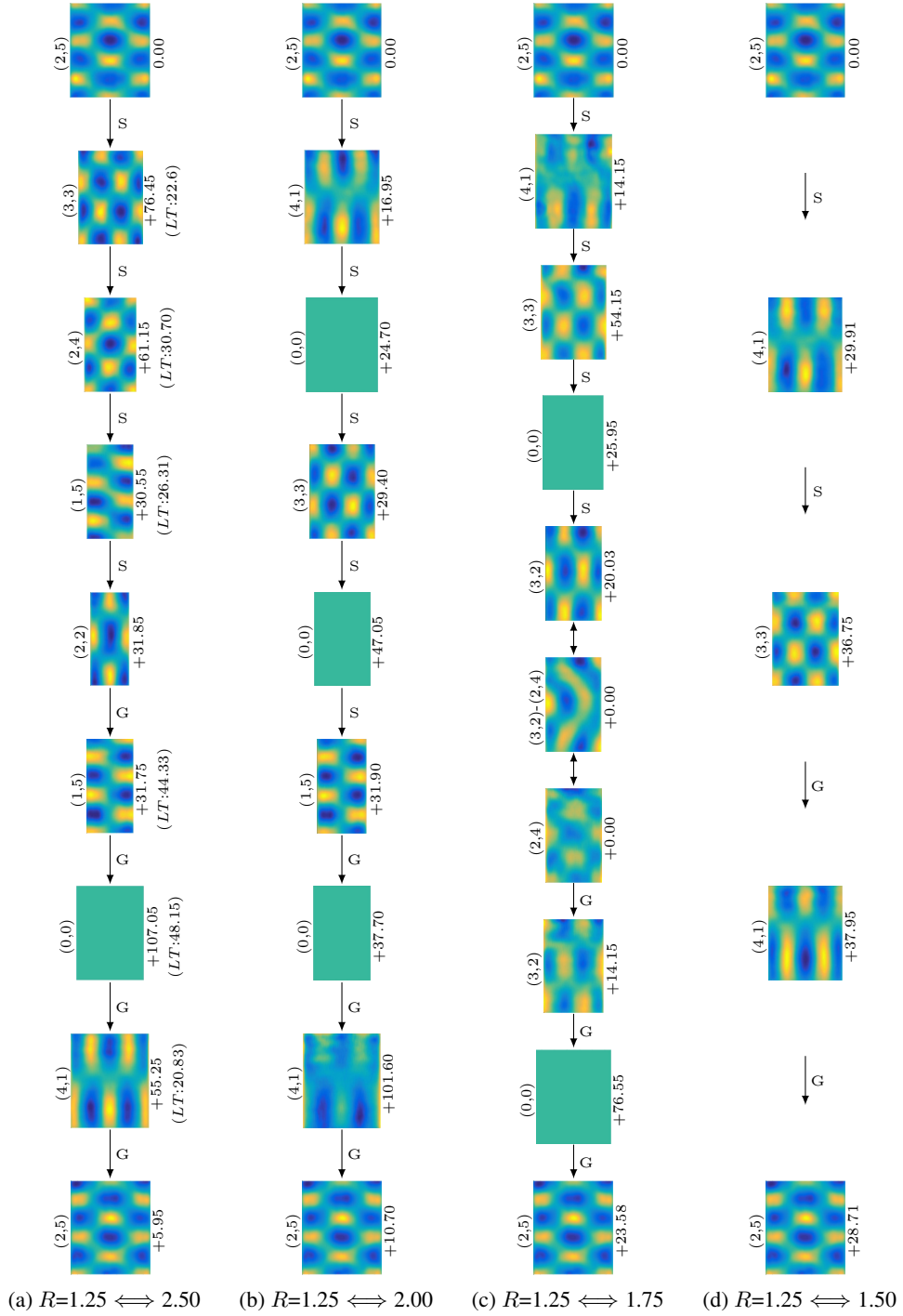


Figure 2.10: Pattern observed on domain shrinkage (S) and growth (G) paths, for four domain aspect ratios. Up-down arrows indicate pattern competition regime. For each image of the pattern scaled proportionally to its instantaneous aspect ratio, the mode number is stated on its left and the number on the right denotes the formation time difference Δt between the given mode and the previous mode on the path. In (a) we also show the lifetime (LT) of each pattern. The experimental fixed parameters are frequency 11.00 Hz, acceleration 1.32 m s^{-2} , and wall speed 0.15 mm s^{-1} .

Although the present system is 2D, the difference between shrinkage and growth paths can be explained invoking the theoretical insights for 1D systems (Krechetnikov & Knobloch, 2017; Knobloch & Krechetnikov, 2015). Domain contraction is known to cause an early phase-slip, thereby making mode changes more frequent on the shrinkage path allowing the system to introduce new patterns more frequently; on the contrary, domain growth delays the phase-slip forcing one pattern to stretch rather than destroying and replacing it with a new one. In other words, once the walls travel for some distance, either after starting from the rest position or after formation of a new pattern, on the shrinking path a phase-slip occurs and a new pattern is introduced, while on the growing path the existing pattern continues to stretch a bit further thus preventing the formation of a new pattern: altogether this renders the shrinkage-growth process irreversible. Therefore, one might expect shorter lifetime (LT) – time from the moment the pattern is formed to the moment it is fully destroyed – for identical patterns on the shrinkage path compared to the growth path. Such a behavior is confirmed experimentally, with the results shown for the case $R = 1.25 \iff 2.50$ in figure 2.10a, which indicates the lifetime of mode (1, 5) on the growth path being about 1.7 times longer than that on the shrinkage path.

Another dynamic source of the observed irreversibility can be related to the sub- and supercritical bifurcations on the opposite sides of the resonant tongue, illustrated in the static situation in figure 2.6 and discussed at length by Simonelli & Gollub (1989). Namely, from the dispersion relation for the surface gravity-capillary waves we know that variation of the forcing frequency f changes the instability wavenumber and hence leads to its time-dependence, $k = k(t)$. Due to mode quantization on a finite domain we also know (and observe) that changing the domain size has a tantamount effect. In particular, the domain size variation leads to the same type of “Doppler effect” term in the amplitude equation (cf. equation 14 in Krechetnikov & Knobloch (2017)) as that due to frequency detuning, cf. §2.2 in Fauve (1998). In the (A, f) diagram, various mode superpositions and hysteresis belong to the subcritical (left) side, $f < 2f_0$, and the pure modes are excited on the supercritical (right) side, $f > 2f_0$, of the resonant tongue (Simonelli & Gollub, 1989). Although figure 2.6 was developed on the square domain, the theoretical work (Gu *et al.*, 1988) provides sim-

ilar result for the rectangular geometry (Simonelli & Gollub, 1989). Thus, on a time dependent rectangular domain we expect that in the overlap region of the tongues the subcritical region would play a role in the reversibility of the growth-shrinkage paths. For instance, in figure 2.11a on the shrinkage path the patterns (2,4), (3,2)+(2,4), and (2,4) are observed, which should belong to the subcritical region of the overlapped tongues (due to the presence of the superposition), while the pure state mode (2,4) being only present on the growing domain should be due to the excitation in the supercritical region. Therefore, in the case of a shrinking domain modes from the subcritical side of the resonant tongue are excited via a finite-amplitude instability (Krechetnikov & Marsden, 2009), while in the case of a stretching domain modes from the supercritical side emerge: altogether this entails irreversibility.

The other remarkable feature that can be observed from figure 2.10 is that *the patterns on the shorter (in space) shrinkage path are embedded in the longer one*. For example, the patterns (4, 1), (3, 3) and (0, 0) on the shrinkage path $R = 1.25 \rightarrow 1.75$ in figure 2.10c are also included in the patterns observed on the shrinkage path $R = 1.25 \rightarrow 2.00$ in figure 2.10b. Such results are expected in the light of the fact that all the shrinkage paths discussed above start from the same initial conditions and the only difference is the final domain aspect ratio. However, there is one case, cf. $R = 1.25 \rightarrow 2.00$ and $R = 1.25 \rightarrow 2.50$ paths in figures 2.10a,b, where such an embedding does not hold because of mode (4, 1). The only possible difference between these two paths is the wave amplitude of the initial pattern (2, 5) affected by the wave phase at the moment when the walls start moving. We believe that at the given experimental conditions mode (4, 1) belongs to a *pattern competition regime* (cf. §2.2.4) which makes it very sensitive to the initial conditions, including the initial wave amplitude. Another proof that mode (4, 1) belongs to the pattern competition regime can be gleaned from the growth path in figure 2.10b and the shrinkage path in figure 2.10c, where we only observed a weak excitation (i.e. with a low amplitude and for a very short time) of mode (4, 1) compared to all other cases. Since we are well above the threshold for driving amplitude of the corresponding resonance frequencies, weak excitation indicates that we are close to the marginal

stability curve – given the geometry of intersection of stability curves, cf. figure 2.7, we are likely in the pattern competition regime.

Further investigation of the effects of initial conditions is postponed to §2.3.5. So far we have seen that the irreversibility of the shrinkage-growth process is dictated by the distinct differences of the phase-slip behavior on the shrinkage path compared to the growth path. In the following section we will explore if such a phase-slip behavior can be controlled.

2.3.4 Wall speed effects

Next, the effect of wall speed on shrinkage and growth paths is investigated. At the driving frequency 11 Hz and acceleration 1.32 m s^{-2} , four distinct wall speeds were considered with the domain aspect ratio changing as $R = 1.25 \iff 2.00$. The first significant finding, which is evident from figure 2.11, is that *reducing speed of walls reveals greater number of patterns on the path*. For example, at a wall speed of 0.15 mm s^{-1} , cf. figure 2.11b, the shrinkage path reveals four patterns and on the growth path two patterns are formed, but at 0.03 mm s^{-1} , cf. figure 2.11a, the number of patterns are six and seven on the shrinkage and growth paths, respectively. Thus, the lower the speed the higher is the number of patterns observed on the path.

The above behavior can be understood as follows. Considering the discussion in § 2.3.1, the *timescale of the domain evolution* plays a crucial role in pattern formation. When the domain evolves on a slow timescale, such as in figure 2.11a, the present pattern starts to become unstable generating a phase-slip which would either insert a new cell into the pattern or annihilate an existing cell. If the resulting pattern with its adjusted wavelength is still unstable, several phase slips may happen until an intermittent stable pattern is formed – this also explains why the mode formation time difference Δt , cf. figures 2.10-2.12, varies from one mode to another. Such a process is typically fast compared to the domain evolution timescale, cf. figure 2.8b, allowing for the formation of several patterns on the path (Knobloch & Krechetnikov, 2014). In the case of a faster timescale of the domain evolution, cf. figures 2.11b-c, pattern formation is naturally impeded as phase slips have no time to develop, which justifies the observation of fewer number of patterns and the presence of flat surfaces

on a major part of the path. Eventually, with further increase of the wall speed “freezing” of the surface in the flat state pattern takes place, which is the only pattern present during the entire domain shrinkage and growth process in figure 2.11d, since the domain evolution timescale surpasses that of the pattern formation (Knobloch & Krechetnikov, 2014). Hence, “freezing” can lead to reversibility, though trivial, by impeding the formation of any new pattern, cf. figure 2.11d. Furthermore, one can conclude that all the patterns observed on the higher speed paths, cf. figures 2.11b-d, are *embedded* in the lowest speed path, cf. figure 2.11a – this is analogous to the one-dimensional theoretical findings of Ueda & Nishiura (2012) indicating that more complex pattern sequences can be expected with slow domain evolution, though these authors have not demonstrated the embedding property.

The aforementioned embedding holds for growth paths between any given wall speed and all the lower speeds studied here, e.g. the growth path with speed of 3 mm s^{-1} is embedded into (or equal to) the growth path with the speed of 0.3 mm s^{-1} and so forth. However, such an embedding does not hold for shrinkage paths for the reason being attributed to pattern competition regimes, which are present in the growth paths as well but do not affect embeddings as explained below. As discussed in §2.2.4, the pattern competition regime is the relatively narrow region of the intersection between two stability curves, in which the system can be perturbed and thus moved to the single mode stability region leading to exhibition of one of the modes, cf. figure 2.7. At the lowest speed considered here, perturbations affecting, in particular, the boundary conditions and thus the dispersion relation (see the discussions in §§2.1 and 2.3.7) are not strong enough to force the system outside the mode competition region, cf. figure 2.11a, whereas at a higher speed only one of the modes (or even none of them in the extreme case where the previous pattern on the path is “frozen”) is observed due to stronger perturbations imposed on the system. Therefore, depending on which mode gets a chance to exhibit itself, embedding may or may not hold. For instance, on the slowest growth path, cf. figure 2.11a, there exists one pattern competition regime revealing modes (4,2) and (4,1), from which (4,2) fails to exist at all higher speeds, cf. figure 2.11b-d, and also (4,1) is only present at one higher speed studied, cf. figure 2.11b, thus allowing the embedding. Since the two components of the pattern competition regime on shrinkage path, modes (3, 2) and (2,4), are present non-uniformly

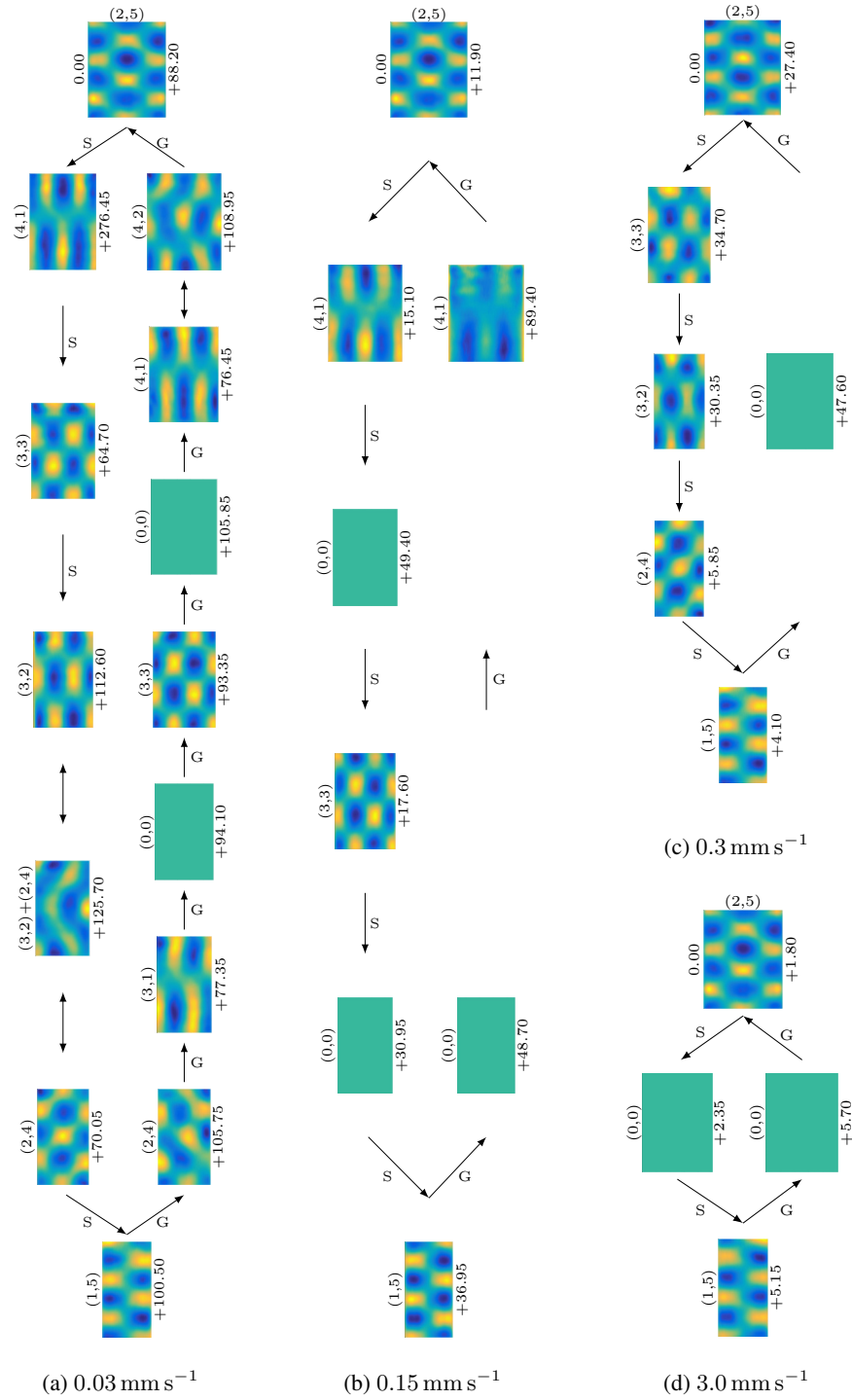


Figure 2.11: Patterns observed on shrinkage and growth paths with four distinct wall speeds. Up-down arrows indicate pattern competition regime. The experimental fixed parameters are frequency 11 Hz , acceleration 1.32 m s^{-2} , and the domain aspect ratio changes $R = 1.25 \iff 2.00$. Same as in figure 2.10, the images are scaled according to the instantaneous aspect ratio and the mode formation time difference Δt is indicated on the right side.

at higher speeds in the sense that their existence is dependent on the wall speed (either one of them or both fail to exist), this prevents the aforementioned embedding to hold for shrinkage path, cf. figure 2.11. In general, the embedding discussed here is more likely to hold for the growth path compared to shrinkage path (such as the case studied in this experiment) due to the fact that the growth path reveals fewer number patterns which may prevent the non-uniform presence of the pattern competition regime's components as explained below.

Based on the discussion in section 2.3.1, for the mode change to happen the flat surface, i.e. zero mode (0,0), needs to be formed during the phase-slip event. In figures 2.10 and 2.11 we showed only those zero modes at which the surface remained flat for a substantial period of time, i.e. order of 10 seconds or above. Considering the presented superpositions of modes involved in pattern competition regimes as distinct patterns while neglecting the flat surfaces during domain shrinkage and growth, one can see from figures 2.10-2.11 that in general *the number of patterns formed on the shrinkage path is greater than or equal to the number of patterns on the growth path*. Following the detailed discussion in §2.3.3, the shrinkage-growth process found to be irreversible due to more frequent phase-slips on the shrinkage path and, as pointed out, such behavior leads to the formation of greater number of patterns on the shrinkage path. Hence, this experimental observation is consistent with the theoretical findings in one dimension (Knobloch & Krechetnikov, 2015; Krechetnikov & Knobloch, 2017).

Given the above ideas, we are now in a position to explain the difference between wall speed thresholds mentioned in section 2.3.2 for the direct consecutive mode change $(1, 5) \rightarrow (2, 5)$ and $(2, 5) \rightarrow (1, 5)$ on the growing and shrinking domains, respectively. From figure 2.11 it is clear that there exist various intermittent patterns on the shrinkage-growth paths between these two modes and thus to achieve a direct consecutive mode change $(2, 5) \leftrightarrow (1, 5)$ formation of intermittent patterns should be prevented, i.e. freezing of the flat surface after destruction of the initial pattern needs to happen, cf. figure 2.11d. Since the fact that on the shrinking domain more patterns compared to domain growth are observed is equivalent to faster pattern formation timescale, to surpass it in order to ensure pattern “freezing” a higher speed of the walls is required. Thus, the direct consec-

utive mode change $(2, 5) \rightarrow (1, 5)$ is accomplished with a higher speed 2.4 mm s^{-1} of the walls on the shrinkage path, cf. figure 2.11d, compared to the reverse (growth) direction with that of only 0.18 mm s^{-1} , cf. figure 2.11c. One may ask if there is an upper bound on the wall speed: in the case of domain growth there is none as no sloshing waves generated, but on the shrinkage path, indeed, an upper bound is expected due to sloshing effects.

Altogether, the wall speed was found to have significant effects on patterns evolution ranging from allowing the formation of complex sequences of patterns to impeding their formation on both growing and shrinking paths; however, it appears that the final pattern on a path is unaffected by wall motion, cf. figure 2.11. This impression is revisited in the following subsections.

2.3.5 Effect of initial conditions

In the next two subsections, we will address the previously raised questions regarding the effects of initial conditions and domain evolution on the final stage pattern. In order to vary the initial condition, while keeping all the other parameters fixed at the initial stage, one realizable possibility is to exploit *a pattern competition regime*, in which more than one mode can co-exist so that a proper initial pattern at the moment walls start to move can be selected (another, more subtle possibility is to start from a different instant within the single mode wave period).

Two specific cases are studied and shown in figure 2.12. In the first case, cf. figure 2.12a, corresponding to the driving frequency 12.3 Hz , acceleration 1.43 m s^{-2} , wall speed 0.15 mm s^{-1} , and domain aspect ratio of $R = 1.25$, modes $(4, 4)$ and $(2, 6)$ are superimposed (at an arbitrary, but fixed in a concrete realization, phase difference). Two separate runs with different starting points, modes $(4, 4)$ and $(2, 6) + (4, 4)$, reveal two distinct shrinkage paths on the right and left in figure 2.12a. However, the final patterns are identical and settled right after (within 2 seconds) walls stop moving in both cases. In the second case, when the experimental parameters were the driving frequency 11.2 Hz , acceleration 1.28 m s^{-2} , wall speed 0.15 mm s^{-1} , and the same domain aspect ratio of $R = 1.25$, the pattern competition regime exhibits a superposition of modes $(2, 5)$ and $(4, 3)$, cf. figure 2.12b. Starting from each of these two modes, two distinct paths are recorded.

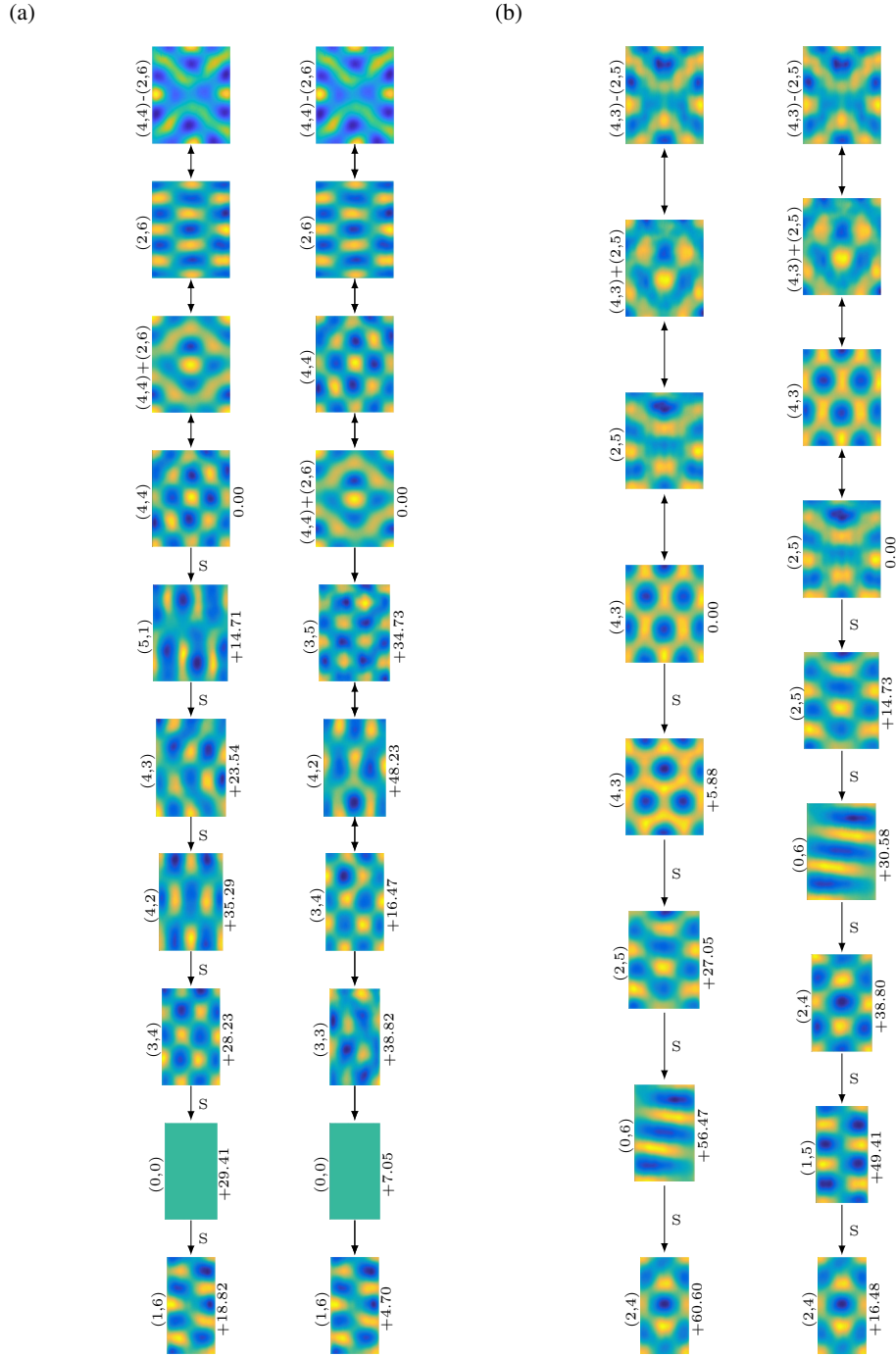


Figure 2.12: (a) Two different runs with two initial modes, $(4, 4)$ and $(4, 4) + (2, 6)$ on the left and right respectively at frequency 12.3 Hz , acceleration 1.43 m s^{-2} , wall speed 0.15 mm s^{-1} and the domain aspect ratio changes as $R = 1.25 \iff 2.00$; the amplitude ratio of the two superimposed modes $(4, 4)$ and $(2, 6)$ is analyzed in figures 2.13a and 2.13b. (b) The initial modes are $(4, 3)$ and $(2, 5)$ on the left and right respectively at frequency 11.2 Hz , acceleration 1.28 m s^{-2} , wall speed 0.15 mm s^{-1} , and the domain aspect ratio changes as $R = 1.25 \iff 2.00$; the superposition of modes $(4, 3)$ and $(2, 5)$ has the corresponding amplitude ratio of $1.00 : 0.95$. Same as in figure 2.10, the images are scaled according to the instantaneous aspect ratio and the mode formation time difference Δt is indicated on the right side.

Similar observations were made on the growth path as well; however, here we only presented the results from shrinkage path as it better demonstrates the above fine behavior of *dependance on the initial pattern characteristics* because the number of patterns formed tends to be greater than that on the growth path (§2.3.3).

Since it is known (§2.2.4) that pattern competition regime is capable of exhibiting chaotic behavior (Ciliberto & Gollub, 1984, 1985a), to assure periodicity of the system state we used two different methods. The first approach is based on construction of the phase-space portraits corresponding to the slow amplitude of the involved modes, cf. figure 2.13b, extracted from the reconstructed surface deformation with the help of 30,000 images taken over the time interval of 600 seconds, cf. figure 2.13a. The modes found to have their phases as functions of slow time, which is expected (Ciliberto & Gollub, 1984, 1985a). The phases recovered for modes (4,4) and (2,6) in this stable (time-independent) regime are linear functions of fast time, i.e. $\phi_{(4,4)} = 0.385 [\text{rad s}^{-1}] t + 0.24 \pi$ and $\phi_{(3,3)} = 0.385 [\text{rad s}^{-1}] t$, which reveal about $\pi/4$ phase difference between the two modes. Again, if we introduce the non-dimensional fast time $\bar{t} = \omega_0 t$, then $\phi_{(4,4)} = 0.01 \bar{t} + 0.24 \pi$ and $\phi_{(2,6)} = 0.01 \bar{t}$, i.e. $\epsilon = 0.1$. The dependence of the phase on the time is very weak as expected since the modes are located in the stable periodic regime, which is analogous to the result found in literature (for example, see Ciliberto & Gollub (1985a) in which case $\phi(\bar{t}) = 0.008 \bar{t}$ or equivalently $\epsilon = 0.09$). The phase difference allows for the observation of various superpositions. For instance, the pattern labeled as (4, 4) + (2, 6) in figure 2.12a is not exactly the in-phase superposition of the two modes even though it may appear so. The resulting phase portrait, which depicts the real part of the two slow amplitudes $a_{(2,6)}$ and $a_{(4,4)}$ against each other, is presented in figure 2.13b revealing no chaotic behavior and instead confirming the periodic state of the system.

Although decomposition of the total amplitude is one of the most desirable methods to study the chaotic behavior of the involved modes, it is limited by the assumed number of modes. Therefore, one also finds it beneficial to analyze the total amplitude $a = C(\tau) \cos [\omega_0 t + \phi(\tau)]$ in (1.29) as a single time series, especially because in the case of Faraday waves there are always a few weakly excited modes contributing to the surface deformation and potentially affecting the dynamics of the

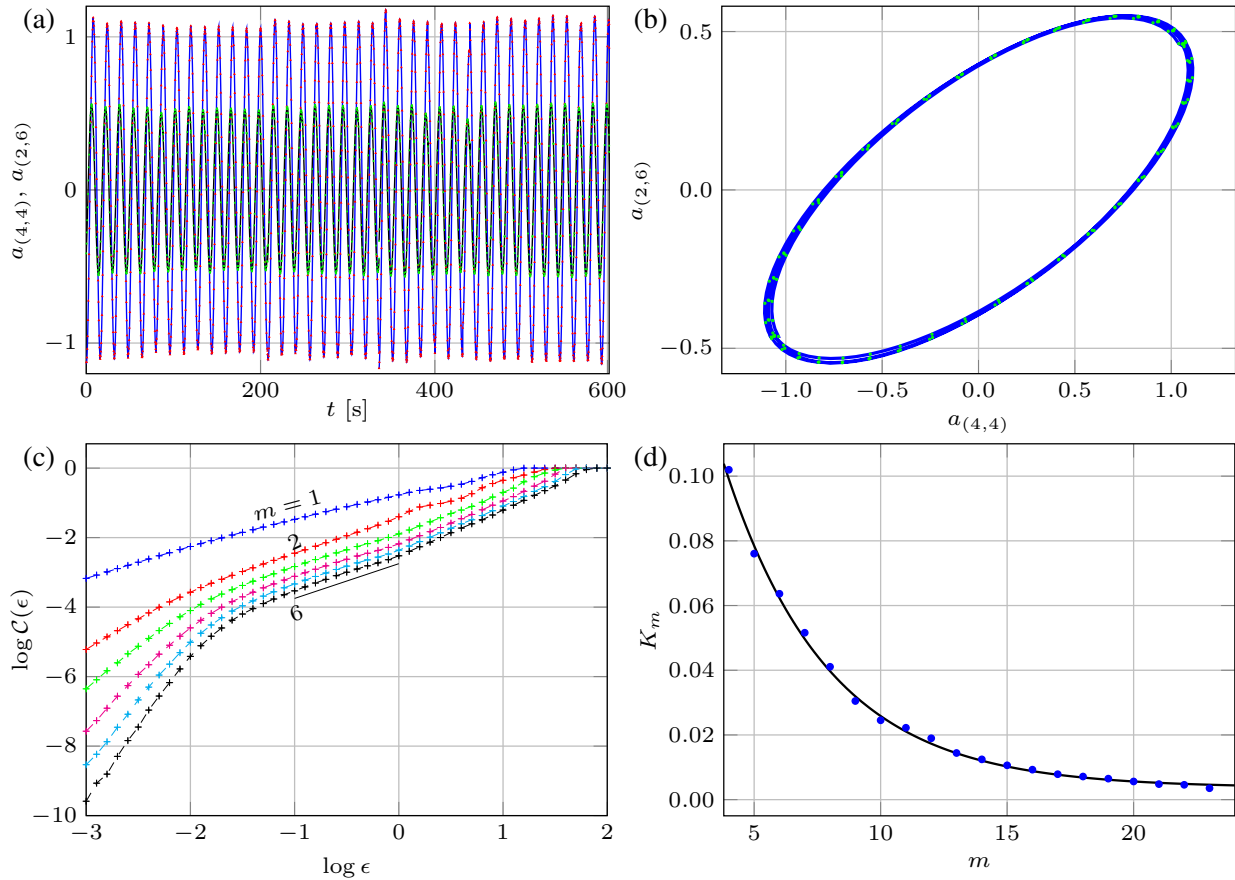


Figure 2.13: Detailed study of a pattern competition regime corresponding to experimental conditions in figure 2.12a. In (a) the decomposed real parts of slow amplitudes, $a_{(4,4)}$ and $a_{(2,6)}$, are presented. These amplitudes are plotted against each other in (b) forming a 4-folded limit cycle. (c) The correlation function $C(\epsilon)$ obtained from a single time series of the total amplitude a for various embedding dimensions m . The solid black line with slope one helps to visualize the saturated slope d . (d) The Kolmogorov entropy K_m , which limit for large m is known to be less than or equal to the sum of the positive Lyapunov exponents.

system. Thus, following the work of [Ciliberto & Gollub \(1985a\)](#) we also resorted to the embedding technique ([Takens, 1981](#); [Grassberger & Procaccia, 1983c](#); [Sauer & Yorke, 1991](#)) as the second approach to test for a chaos through the existence of strange attractors. This technique assumes that all the important dynamical features are contained (embedded) in a single time series, and therefore, with the measurement of Faraday waves amplitude $a(t)$ at only a single location on the water surface not only reveals the type of the regime regularity but also the number of Faraday modes involved. The embedding technique determines both by measuring the dimension of the strange attractor and that of the phase-space, respectively. A strange attractor is characterized as an aperiodic one, in which the surrounding trajectories diverge exponentially from each other in time,

and most importantly is an object of *fractal dimension*: in Euclidean space \mathbb{R}^m , geometrical objects can be fully described as a set of points and their dimension d could range from 0 to m . Standard objects have their dimension as an integer, for instance, points in Euclidean space are represented with dimension $d = 0$, lines with $d = 1$, plane surfaces with $d = 2$, and volumes with $d = 3$. The simplest procedure to determine these values is the idea of box-counting dimension (Henry *et al.*, 2012) which indicates that the number of small cells of size ϵ required to cover the object scales as ϵ^{-d} as $\epsilon \rightarrow 0$. For example, the number of squares with the area ϵ^2 required to cover a surface of the size A is $A/\epsilon^2 = A\epsilon^{-2}$, hence $d = 2$. On the contrary, fractal dimension D refers to the objects with non-integer dimensions, such as strange attractors, and its significance in dynamics lies in the fact that the fractal dimension of a strange attractor is related to the number of dynamical variables, i.e. phase-space dimension size m , required to describe the strange attractor dynamics.

In order to determine the fractal dimension D and the phase-space dimension size m using only a single time-series the embedding technique exploits the theorem proved by Takens (1981) and Sauer & Yorke (1991). Takens embedding theorem assures that if the time-series, for our case $a(t)$, is one of the components of a d -dimensional attractor (with d an integer) then the topological properties such as dimension and Lyapunov exponent of the embedding, formed by the m -dimensional embedding phase-space coordinates constructed as $\{a[t], a[t + \delta t], \dots, a[t + (m - 1)\delta t]\}$, where δt is an arbitrary delay, are equivalent to that of the attractor provided that $m \geq 2d + 1$. Sauer & Yorke (1991) generalized this theorem to the case where the attractor is a strange one with fractal dimension D .

Practically, it is very difficult to measure D from an experimental data set (Swinney & Gollub, 1986; Ciliberto & Gollub, 1984, 1985a; Henry *et al.*, 2012); however, there exist other equivalent estimates of dimension D allowing experimental measurement, the most common one being based on the correlation dimension:

$$D = \lim_{\epsilon \rightarrow 0} \frac{\log C(\epsilon)}{\log \epsilon} \leq D, \quad (2.3)$$

where $C(\epsilon)$ is N^{-2} (with N denoting the total number of data points) multiplied by the number of data-point pairs in the same cell of size ϵ , hereafter denoted by \mathcal{N} . The numerical implementation of

the above equation has been well developed in literature and the algorithm proposed by [Grassberger & Procaccia \(1983a\)](#) is the most widely used. Such an algorithm is based on the approximation that the probability of two points being in a cell of size ϵ is equivalent to the probability of two points being separated in the phase-space by a distance less than ϵ :

$$C(\epsilon) = \lim_{N \rightarrow \infty} \frac{\mathcal{N}}{N^2} \approx \lim_{N \rightarrow \infty} \frac{\sum_{i,j=1}^N H(\epsilon - |\mathbf{x}_i - \mathbf{x}_j|)}{N^2}, \quad (2.4)$$

where H denotes the Heaviside function

$$H(t) = \begin{cases} 1 & \text{if } t \geq 0, \\ 0 & \text{if } t < 0. \end{cases} \quad (2.5)$$

In practical applications, the limits $\epsilon \rightarrow 0$ and $N \rightarrow \infty$ in equations (2.3) and (2.4) cannot be realized, and therefore, it was proposed to plot $C(\epsilon)$ against ϵ for different values of the phase-space dimension m ; then the limiting slope in the scaling region defines the value of d ([Grassberger & Procaccia, 1983a](#)). Accordingly, the specific value of the phase-space dimension m at which the slope is saturated and does not change with further increase of m , defines the dimensional size of the phase space, i.e. the number of required dynamical variables to model the strange attractor.

It can be seen from figure 2.13c that the slope in the scaling region does not change with further increase of m beyond four and is saturated at the value of 1.01 ± 0.02 which corresponds to the dimension of a unit cycle. Such findings indicate that the system is periodic and can be described by a 4-dimensional phase-space (real and imaginary parts of the two slow amplitudes), confirming the results established earlier based on amplitude decomposition: excitation of nearby modes is not strong enough to affect the periodic behavior of the system. The function $C(\epsilon)$ for various m , denoted as C_m here, can also be used to estimate the sum of the positive Lyapunov exponents which correspond to the degree of trajectories' stretching. As proposed by [Grassberger & Procaccia \(1983b\)](#), at a fixed ϵ in the scaling range (for instance, when $\log(\epsilon) = -0.5$) the Kolmogorov's

entropy

$$K_m = (\log C_m - \log C_{m+1}) / \delta t \quad (2.6)$$

reaches a limiting value for large m that is less than or equal to the sum of the positive Lyapunov exponents and δt is the arbitrary decay in the embedding defined earlier. K_m is plotted in figure 2.13d: using an exponential curve fit (Ciliberto & Gollub, 1985a), the limiting value is found to be 0.003 ± 0.001 demonstrating negligible stretching of trajectories in the periodic regime. This adds further credence to our earlier conclusion, based on the phase-space portrait, regarding the periodicity of the system state, which is used as an initial condition to study the dependence of the shrinkage or growth paths on the initial pattern characteristics.

2.3.6 Effect of domain shrinkage or growth on the final stage mode

As evident from the observations we have made so far, the final stage pattern is normally insensitive to whether domain shrinks or grows. In other words, once walls stop moving the formed pattern is identical to the pattern on the time fixed domain of the same aspect ratio. Thus, domain shrinkage or growth effects do not appear to be strong enough to perturb the final stage pattern provided that the pattern is stable at the final domain size when the walls are at rest.

However, in order to reveal any possible weak effect of domain deformation on a final stage pattern, we set experiments where the final stage pattern belongs to a pattern competition regime. The experiments conducted had fixed experimental parameters identical to that in figure 2.12b, but only in the reverse (growth) direction, where the domain aspect ratio changes from $R = 2.00$ to 1.25. When the walls are at rest at the final aspect ratio $R = 1.25$, cf. figure 2.12b, the system is located in the pattern competition regime of modes (4, 3) and (2, 5), where various superpositions (4, 3), (2, 5), (4, 3) - (2, 5), and (4, 3) + (2, 5) are present. Starting from the initial aspect ratio $R = 2.00$ with the well-established and stable mode (2, 4), then growing the domain with various speeds, the following observations were made. For a wall speed below 0.15 mm s^{-1} the final stage only exhibits mode (2, 5), i.e. the given trajectory in the phase-space is attracted to this fixed point, which does not appear to be transient as it was observed over the period of time (several hours) considerably longer

than a typical settling time for a pattern. Above this wall speed the system remains in the pattern competition regime instead. Therefore, it transpires that *the domain deformation, if slow enough, may stabilize the final mode provided such a mode originally belongs to the pattern competition regime.*

At the dynamical systems level, one of the fine effects of domain evolution is that it can force the dynamical system trajectory to get closer to one of its fixed points, allowing the system to reach a stable state. At the physical level, this effect is due to wall motion affecting the bulk flow, which could be different for identical Faraday wave patterns (Périnet *et al.*, 2017). This leads to the possibility that hysteretic phenomena associated with the bulk flow structure (arising if one compares the well-developed flow for a fixed domain size with the flow formed by moving the walls to the same domain size) might be responsible for this memory effect – the dependence of the final Faraday wave pattern on the dynamical system trajectory. Since observations indicate different patterns between the two cases – when the domain is time-fixed or evolves to the same size – the flow in the bulk must necessarily be different, thus establishing the fact of hysteresis.

2.3.7 Effect of wall oscillation

Besides unidirectional motion, we also seek to understand the effect of wall oscillations on an excited Faraday wave mode, which in the linearized 1D stability theory is known to be always destabilizing in the sense that the band of stable wavenumbers is reduced and increasing with lowering the wall oscillation frequency (Krechetnikov & Knobloch, 2017). Here, instead, we study finite amplitude effects of wall oscillations. Depending on the mode, the pattern is observed to able to *elongate/compress* for some range of wall oscillation amplitudes A_w , though its (pattern) amplitude C eventually starts to diminish gradually with increase of A_w . To establish a direct relation between the wall oscillation amplitude A_w and the mode number n , at the fixed wall oscillation frequency of $f_w = 0.375$ Hz the amplitude A_w required to destroy patterns with the form $(1, n)$ was studied. The initial aspect ratio was set $R = 2.00$ and A_w increased with the step of 2 mm. Modes with $4 \leq n \leq 9$

were excited at their own respective driving frequency f and amplitude A , while the corresponding A_w required to destroy each pattern is determined, cf. figure 2.14a.

One might expect that destruction of a mode takes place when the sloshing wave amplitude C_w induced by the wall motion A_w becomes comparable with the Faraday wave amplitude C . The magnitude of C_w can be inferred from the forced surface-wave theory of Ursell *et al.* (1960):

$$\frac{C_w}{A_w} = 2 \frac{\cosh(2k_0 h) - 1}{\sinh(2k_0 h) + 2k_0 h}, \quad (2.7)$$

where k_0 is the real and positive root of $\omega_w^2 = g k_0 \tanh(k_0 h)$. Thus, for $f_w = 0.375$ Hz we find $C_w = 0.08 A_w$, cf. figure 2.14a. However, the amplitude C for each excited mode was different and belonged to the range from 1.3 to 2 mm, cf. the inset of figure 2.14a. For example, for mode (1,6) the Faraday wave amplitude is $C = 1.85$ mm and the corresponding $C_w = 1.12$ mm, while for mode (1,8) with $C = 1.60$ mm the required sloshing wave amplitude C_w induced by the walls was larger and equal to 1.44 mm. Thus, it is surmised that *comparability of the amplitudes C_w and C is not the only deciding factor in destruction of a pattern* as they do not form a trend. However, figure 2.14a indicates that with increasing n the pattern becomes more resistant to destruction as both A_w and C_w increase almost linearly. The latter is easy to understand from a physical point of view: when the number of pattern cells is higher, the driving frequency is higher as well, which means that the inertia force required to bring the fluid into motion increases and is balanced by higher gravity and capillary forces as per the linear free surface evolution equation $\zeta_{tt}^k + \omega_0^2(k) \zeta^k = 0$ with $\omega_0(k)$ given by (1.26); in particular, for higher n the curvature of the surface is locally larger compared to that of a lower mode number pattern and thus the surface tension force is stronger. Therefore, it requires a larger amplitude sloshing wave to overcome higher forces involved in the Faraday wave formation.

Since wall oscillations can be considered as pumping energy into the system – with increase in the frequency of the walls f_w energy injected to the system increases – one can expect that the pattern under consideration would eventually break down at high enough frequencies. Therefore, to gain more insight into the effects of domain oscillation we performed another set of experiments, in which the minimum frequency f_w required to destroy patterns of the form (1, n) at the fixed wall

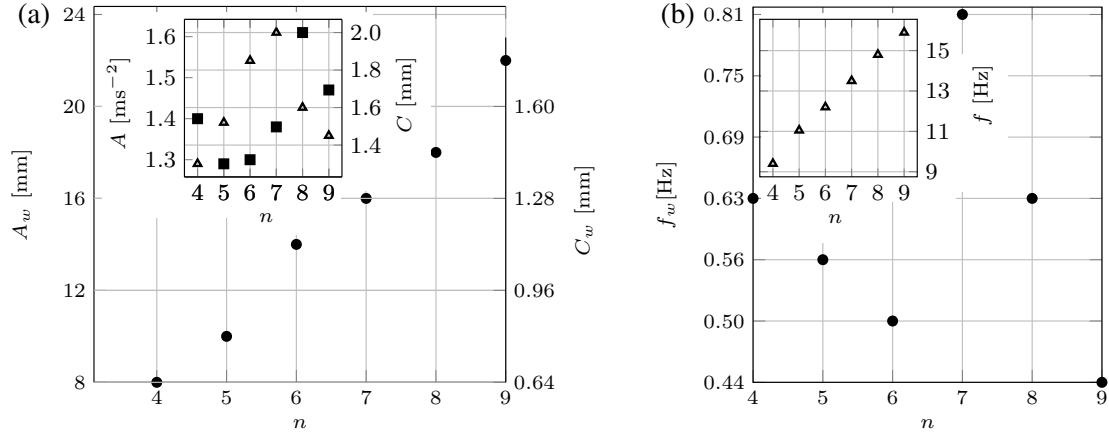


Figure 2.14: (a) Amplitude of wall oscillation A_w and corresponding wave amplitude C_w induced by the walls at the wall oscillation frequency $f_w = 0.375$ Hz required to destroy a mode $(1, n)$; Faraday wave amplitude C (triangles) and the amplitude of the tank vertical oscillations (squares) are presented in the inset. (b) The minimum f_w required to destroy a pattern at the fixed wall amplitude $A_w = 6$ mm. Each mode is excited at the respective driving frequency f (cf. inset) and amplitude with initial domain aspect ratio of $R = 2.00$.

amplitude $A_w = 6$ mm was measured, cf. figure 2.14b. The non-monotonic behavior of f_w with respect to n can be partially explained based on the stability properties of the excited mode $(1, n)$. Namely, in the course of the experiments we noticed that the required frequency f_w depends on how well-established a pattern is, i.e. on the location of the excited mode with respect to the marginal stability curve: when a pattern is excited at a driving frequency and amplitude that are very close to the stability boundary, it is very sensitive to any perturbation and can be easily destroyed. For example, the excited mode $(1, 6)$ is fairly sensitive to any perturbation and destroyed at a lower frequency compared to mode $(1, 7)$, which was observed to be resilient against larger amplitude perturbations.

2.3.8 Draining water tank

This section provides an example of a time-dependent domain with no dilution or advection effects. Namely, there also exist systems where domain change in one spatial direction leads to pattern wavelength change in another – though different from the transverse instability discussed in §2.3.2 – propagation of waves on the surface of a leaky shallow tank as pointed out by Knobloch & Krechetnikov (2015). Thus, as water slowly drains out of the tank, the frequency of free surface

waves changes according to (1.26). Conversely, in the case of Faraday waves, from the dispersion relation (1.26) one can expect that due to variation of depth h with time the mode wavenumber k would change as the frequency of the wave ω_0 is fixed by the driving frequency ω . In either case no dilution or advection terms are present in the governing equations because the domain changes in a direction orthogonal to the direction in which the waves are formed. A different example of such systems is provided by pattern formation in melting boundary convection (Vasil & Proctor, 2011).

By conducting an experiment where the water depth is controlled with a syringe pump, with the driving frequency 12.2 Hz, amplitude 1.62 m s^{-2} , domain aspect ratio of $R = 1.25$, and a slow draining rate of 5 ml min^{-1} , four distinct patterns were observed as the depth was reduced from 12.0 mm to 9.5 mm, cf. figure 2.15. In theory, based on the dispersion relation for the experimental variables stated above, one can expect that with the decrease of depth the wavenumber would increase. Such a behavior is confirmed in figure 2.15, where the patterns are observed in the order of increasing wavenumber starting with mode (3, 5) with $k = 130.89 \text{ m}^{-1}$ at full depth and ending with $k = 136.13 \text{ m}^{-1}$ corresponding to mode (2, 6) at $h = 9.5 \text{ mm}$. It should be noted that in figure 17 for the superposition pattern (4, 4) + (2, 6), cf. §2.2.4, the amplitude of mode (4, 4) is about twice that of mode (2, 6). With further decrease of depth, this pattern first reduces to mode (4, 4) and then to (2, 6) as per the dispersion relation (1.26). At the depths below 9.5 mm, unsteady random and then meniscus waves appeared as the vertical acceleration is no longer sufficient to excite any Faraday wave pattern.

While from a theoretical point of view, in the inviscid approximation mode change is considered to be non-smooth, the presence of viscosity prevents abrupt changes from one mode to another; thus a new pattern is formed while the other one phases out with an intermittent flat surface, as we saw in §2.3.1. The remarkable behavior observed in this experiment, which is distinctly different from the previous ones, was the formation of an intermittent flat surface for a considerable amount of time $\sim 10 \text{ s}$ between all the mode changes compared to *most* mode changes on the horizontal time-dependent domains happening over the time interval $\sim 1 \text{ s}$. Such behavior indicates that patterns cannot remain stable very far from the respective depth dictated by the dispersion relation unlike

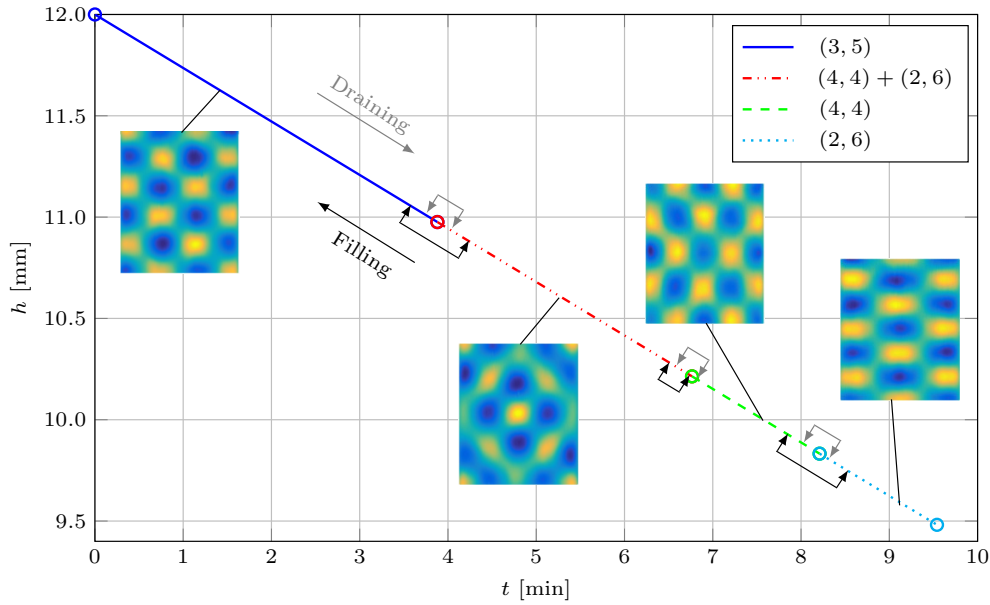


Figure 2.15: Patterns observed in the draining water tank. The depth of water is denoted by h and the experimental fixed variables are driving frequency 12.2 Hz, amplitude 1.62 m s^{-2} , domain aspect ratio of $R = 1.25$, and draining rate of 5 ml min^{-1} .

the case of time-dependent horizontal domain in which typically one pattern is stretched beyond that permitted by a time-fixed domain until a phase slip occurs and the next pattern is formed. In the latter case, pattern stretching is accompanied by wavenumber shifting given that the pattern remains stable beyond the wavenumber allowed by dispersion relation on the time-fixed domain. Therefore, pattern stretching or equivalently wavenumber shifting is found to be less noticeable in systems such as a draining water tank, which is due to the absence of dilution and advection effects making each pattern to form and remain stable only in a narrow range of depths around the time-fixed depth imposed by the dispersion relation. This observation brought us to the conclusion that pattern formation in this type of systems should be reversible (on the filling-draining paths, cf. figure 2.15) unlike in systems with dilution/convection, where frequent phase-slips on a shrinking domain and prominent pattern stretching on a growing domain stipulate irreversibility (§2.3.3).

2.4 Conclusions

In this work, we first investigated the mechanism of mode change by studying the phase-slip phenomena experimentally and observed that, as expected from phase transition theory, the mode change occurs when the complex slow amplitude of a Faraday wave goes through zero (§2.3.1). Moreover, from this experiment we found that the slow evolution time scale τ of the Faraday wave phase and amplitude is enslaved to that of the walls motion τ_w . The most remarkable finding in the mode change phenomena on time-dependent domains is the transverse instability (§2.3.2) orthogonal to the direction x of the domain deformation, which is more common than the direct one and explained as follows. Since subharmonic Faraday waves have their frequency ω_0 fixed at half of the driving frequency ω , the dispersion relation (§1.26) entails that the wavenumber k must be fixed as well. With domain evolution in the x direction the wavenumber k_x gets stretched due to dilution (Krechetnikov & Knobloch, 2017), and thus the wavenumber k_y in the y direction should adjust itself accordingly to keep k constant leading to the transverse instability.

Next, we considered sequences of mode changes on the shrinkage and growth paths (§2.3.3), which led to several findings. First, domain shrinkage-growth is irreversible with the number of patterns formed on the shrinkage path being greater than or equal to the number of patterns on the growth path. This is dictated by the fact that phase-slips are more frequent on shrinkage paths allowing the formation of larger number of patterns, while domain growth delays the phase-slip allowing a pattern to be stretched (Krechetnikov & Knobloch, 2017). Second, patterns on a shorter shrinkage path are embedded in longer ones provided the starting points for such paths are identical. Third, in the regime of the domain size oscillation (§2.3.7), we found that the pattern resistance against destruction depends not only on the amplitude of induced sloshing waves being comparable with that of the Faraday waves, but on other factors as well, e.g. patterns with a shorter wavelength are more resistant to destruction. Furthermore, depending on the location of the observed mode w.r.t. the marginal stability curve the pattern could be either easily disturbable or, conversely, insensitive to the perturbation caused by walls oscillation.

We also investigated the effect of wall speed (domain size evolution rate) on the pattern formation (§2.3.4). It was found that reducing the speed of walls reveals a larger number, i.e. more complex sequences, of patterns on the path, because the slower the domain evolution timescale, the more phase-slips either insert new cells into the pattern or annihilate the existing ones – the process typically faster compared to the domain evolution timescale. Conversely, extreme speed of walls may cause pattern freezing because the domain growth timescale surpasses that of the pattern formation. Naturally, all the patterns observed on higher speed paths are embedded in the lowest speed path since the lower evolution rate reveals a larger number of intermediate patterns.

To figure out other deciding factors influencing the sequences of patterns observed on evolving domains, we considered the effect of initial pattern characteristics starting from a pattern competition regime and discovered different sequences of patterns on the paths (§2.3.5). On the other hand, the effect of domain evolution on the final stage mode was found by choosing the final domain aspect ratio to belong to a pattern competition regime: if the domain evolution is slow enough, it may select either of the pattern competition modes as a final one (§2.3.6). We explained this phenomenon with the hysteretic behavior of the bulk flow field.

The last finding of the paper concerns reversibility of the domain shrinkage-growth in the absence of advection and dilution effects as demonstrated by performing an experiment in which the horizontal domain size is fixed but the fluid layer depth is varying (§2.3.8). We concluded that pattern stretching and equivalently wavenumber shifting is less prominent in the systems without advection and dilution effects (such as a draining tank), compared to the systems in which the advection and dilution effects are present (such as a tank shrinking/growing in the horizontal direction), thus allowing the pattern-changing process to be reversible.

Among the questions requiring further study are on the theoretical understanding of the hysteretic behavior of the bulk flow leading to the observed effects of domain shrinkage or growth on the final stage mode. The exact Eckhaus-type mechanism responsible for transverse instability needs to be established as well. Finally, given that the pattern competition regime may involve not only regular, but also chaotic motion (Ciliberto & Gollub, 1984) and that domain deformation can

isolate one of the competing modes in the regime which would otherwise correspond to pattern competition on a time-fixed domain of the same size, it becomes clear that domain deformation may also serve as a mechanism regularizing chaotic motion.

Appendices

2.A Effects of gaps underneath the moving walls

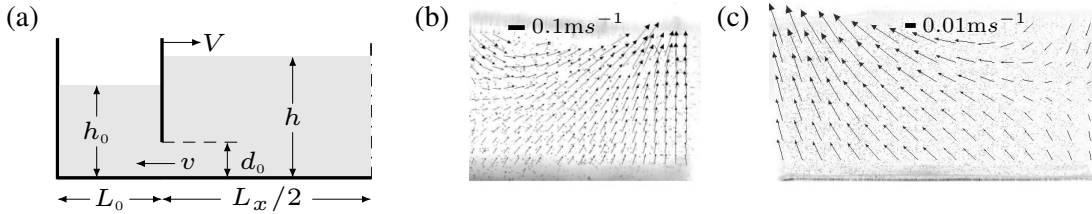


Figure A2.1: (a) Optimization of the gap height d_0 under moving walls (half of the tank is shown). (b) Flow field observed in the bulk between a maximum and an adjacent minimum of the free surface deformation 15 mm apart before domain shrinkage and (c) 25 mm apart after domain shrinkage. Note that when the domain is shrinking in the x direction, the wavelength in the x direction may *increase*: for instance, in figure 2.10a the mode change $(3, 3) \rightarrow (2, 4)$ indicates that the mode number in the x direction decreased which means the wavelength in that direction increased (as the change in the domain size is not commensurate with the change in the wavelength) and the distance from a maximum to the adjacent minimum of the free surface deformation has increased accordingly. In both (b,c) the wave amplitude is 1.5 mm.

An optimization of the gap height d_0 was performed with the goal to maintain the layer depth h within the accuracy ± 0.1 mm required by the sensitivity of Faraday waves in our setup, while introducing the minimal disturbance to the roll structure in the bulk. Apparently, the former requires one to enlarge the gap, while the latter to minimize it. Just to illustrate the idea of optimization with reference to figure A2.1a, let us consider the case when the horizontal dimensions of the water layers are much larger than the distance traveled by the wall at speed V , $L_0 \sim L_x \gg V t$, and, naturally, that the water layer depth considerably exceeds the gap height $h \gg d_0$; the variables are explained in the figure. Then the time t_1 it takes to create a disbalance in the heights $h - h_0$ between water levels on the left and right of the wall and the time t_2 it requires to level off the difference $h - h_0$ created by the wall motion can be estimated as

$$t_1 \sim (h - h_0)L_x/(hV) \quad \text{and} \quad t_2 \sim (h - h_0)L_x/(d_0v), \quad (\text{A2.1})$$

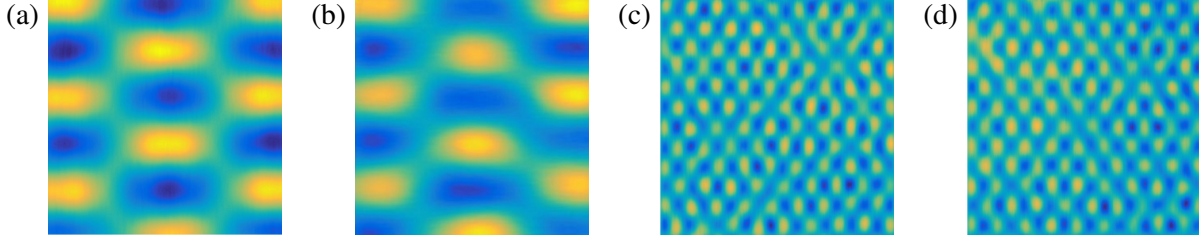


Figure A2.2: Top view of Faraday wave modes (2,5) and (17,11) excited at $R = 1.25$ with 2 mm gap underneath walls in (a) and (c). In (b) and (d) there is no gap. Modes (2, 5) and (17, 11) were excited at the frequencies 11.00 and 32.55 Hz and accelerations 1.32 and 3.49 m s^{-2} , respectively. Patterns in (c) and (d) were captured at different instants on the wave period. It should be noted that at high driving frequencies, patterns of the sine-type are formed such as the mode (17, 11) presented in (c,d).

respectively; here the escape velocity $v = \sqrt{g(h - h_0)}$ through the gap is driven by the hydrostatic pressure difference. The optimum corresponds to $t_1 \geq t_2$. Taking $d_0 \sim 1$ mm, $h - h_0 \sim 1$ mm, and $V \sim 1$ mm s^{-1} we find $t_1 \sim 10$ s $\geq t_2 \sim 1$ s, i.e. no significant disbalance $h - h_0$ occurs. The escape velocity for this choice of parameters is $v \sim 10^{-1}$ m s^{-1} , which yields $Re = O(10^3)$, i.e. the flow is in the inviscid regime and no significant dissipation takes place in the gaps. Similar conclusions persist down to and below $h - h_0 \sim 0.1$ mm.

To confirm that the gaps underneath walls do not affect the flow field regime in the bulk, which may in turn perturb the Faraday patterns, three sets of experiments were performed. First, for the domain aspect ratio of $R = 1.25$ two modes with large and small wavelengths have been excited with and without the 2 mm gap underneath walls, cf. figure A2.2. For both patterns no visible differences were identified between the two cases.

Second, the shrinkage-growth process previously presented in figure 2.11b was repeated without any gaps underneath walls by draining the water with the syringe pump from the inside of the domain. The results indicate no differences in the sequence of formed patterns and only minor changes in the formation time difference Δt not exceeding 5 s, which corresponds to a change in the domain size of only 1.5 mm ($\Delta L_x/L_x \simeq 1\%$) at the given walls velocity of 0.15 mm s^{-1} .

Third, ideally the gaps would have no effect on Faraday waves if the deep water conditions are met, i.e. in the inviscid limit, $\tanh kh = 1$. Since the excited wavenumbers in the cosine-regime, which was used throughout the experiments, had the range of 100 to 160 m^{-1} , cf. figure 2.4a and

its inset, with the depth of $h = 12$ mm we then get $0.83 \leq \tanh(kh) \leq 0.95$ implying that we are relatively close to the deep water condition. To this end, we also visualized the velocity field using the PIV system (§2.1.2) – figures A2.1b,c, however, indicate that the particle velocities near the bottom wall have significant horizontal components, so the deep water condition is not fully satisfied. Having said that, the recent study by Périnet *et al.* (2017) shows that when Faraday waves are excited at the surface, there exist three possible types of streaming flow *regimes* in the bulk categorized based on their appearance as counter-rotating rolls, mustache-shaped, and irregular patterns, respectively. Streaming itself is the result of complex mechanisms that couple the flow inside the bulk and at the boundary layers: (i) the oscillatory flow in the bulk induces an oscillating boundary layer; (ii) the oscillating boundary layer exerts a feedback on the bulk flow whose steady component originates the streaming; (iii) the streaming is diffused into the bulk due to a viscous process. From our PIV measurements we observed that the bulk regime type is the same (mustache-shaped) before and after the motion of the walls as presented in figures A2.1b and A2.1c, respectively. In other words, although there exist minor flow underneath the walls, the flow field regime in the bulk does not change during time-dependent domain experiments, and thus the gaps leave Faraday waves unaffected.

2.B Meniscus waves

Due to the semi-pinned boundary condition in our experiments it is impossible to prevent the formation of meniscus waves: however, we have not observed substantial excitation of these waves after the transient period of settling Faraday waves patterns. In fact, recent experimental work of Batson *et al.* (2013) shows that meniscus exhibits measurable interactions with harmonic Faraday waves rather than subharmonic ones at low frequencies.

In our experiments the contact line can move along the wall up to 0.7 mm, but the maximum amplitude of the meniscus waves observed in the middle of the container of size $150 \times 150 \times 12.7$ mm³ is only 0.2 mm. To reconcile this, let us consider the basic physics of the waves generated by the menisci motion and their dissipation. While it is not straightforward to separate Faraday and menis-

cus waves in the setting at hand, for small amplitude oscillations one may consider them as a linear superposition with the meniscus waves generated by vertical oscillations of a wall in the stationary container – the setup studied by [Hocking \(1987a,b\)](#). The key effect responsible for higher amplitude at the wall is purely geometric – while the interface meets the wall at the (dynamic) contact angle, the shape of the meniscus waves away from the wall is dictated by the capillary-gravity dispersion relation (1.26) and hence, based on mass conservation, the wave amplitude may decay significantly from that at the wall over short distance especially for perfect wetting conditions, when the contact line rises the most.

Besides the geometric effect, there is also dissipation at the contact line and due to bulk viscosity, but it proves to be subdominant. The following estimate of the waves decay due to bulk viscosity alone shows negligible effect. The amplitude of the meniscus wave in the center of the water tank can be estimated using the relation $\zeta_c = \zeta_0 e^{-\gamma x}$ ([Lamb, 1994](#)), where the spatial decay rate γ in the deep water case is calculated as $\gamma = 2\nu k^2/U$, with $U = V - \lambda dV/d\lambda$ being the group velocity of the waves calculated from the velocity $V = \omega/k$ of a wave of frequency $\omega = \omega_0$ and wavenumber $k = k_c$ excited at that frequency, i.e. $\omega_0^2 = gk_c + \sigma k_c^3/\rho$. For the typical driving frequency of 11 Hz, k_c will be $\approx 296 \text{ m}^{-1}$. Thus, the equation above yields $\gamma = 2 \text{ m}^{-1}$, which is not sufficient to explain the observed decay. Accounting for a finite depth in our case does not change this estimate significantly ([LeBlond & Mainardi, 1987](#)).

2.C Damping sources and effects

It is well-known that damping proved to be very difficult to account for properly in the Faraday wave phenomena ([Gollub, 2006](#)), especially for low viscosity fluids where contributions of surface contamination and contact line dissipation may not be negligible ([Bechhoefer et al., 1995](#)). At the very basic level, introduction of the linear damping term $2\gamma \dot{\theta}$ in (1.1) leads to the replacement of ϵ by $(\epsilon^2 - \gamma^2)^{1/2}$ in the subharmonic instability range (§1.2), i.e. the subharmonic response is possible only if the driving amplitude exceeds the dissipation effect $\epsilon > \gamma$.

The first systematic stability studies of Faraday waves incorporating bulk viscosity were carried out by [Kumar & Tuckerman \(1994\)](#) and [Kumar \(1996\)](#) using Floquet analysis, both assuming laterally unbounded domain confirming the key effect that a finite damping requires a finite non-zero driving acceleration for the instability to occur. Once damping is introduced, the linear amplitude equations for normal modes become coupled, though for low viscosity fluid ($\nu k^2 \ll 2\omega_0$), as in our case, one can compute the effect of viscosity perturbatively and recover a decoupled Mathieu equation for each mode ([Benjamin & Ursell, 1954](#)).

Theory of [Kumar & Tuckerman \(1994\)](#) and [Kumar \(1996\)](#) accounting for bulk damping was tested only experimentally by [Bechhoefer *et al.* \(1995\)](#) with a highly viscous fluid in a finite-size container and showed agreement if the ratio h/L is small enough and the frequency is sufficiently high, so that other sources of damping become less crucial compared to that of bulk. In order to test the theory at low frequencies, [Batson *et al.* \(2013\)](#) came up with an experimental setup in which the primary dissipation arises from damping in the bulk by having the stress-free boundary condition at the sidewalls satisfied using two immiscible liquids (to be in accordance with the [Kumar & Tuckerman \(1994\)](#) theory). Their experimental results were in excellent agreement with the theory and made them able to comment on various sources of dissipation in previous experimental studies of [Benjamin & Ursell \(1954\)](#), [Ciliberto & Gollub \(1985a\)](#), and [Henderson & Miles \(1990\)](#). For instance, they showed that the contact line mobility represents a substantial source of dissipation. However, to date there is no rigorous theory that accounts for dissipation due to moving contact lines, boundary layers near walls and corners, meniscus waves, and bulk viscosity ([Kidambi, 2009](#)). Instead, an empirical approach to integrate the wall effects was offered by [Christiansen *et al.* \(1995\)](#), who incorporated damping as $-2\gamma_t \dot{U}$ in the amplitude equation for the order parameter U ; here γ_t is the total damping coefficient determined empirically and accounting for dissipation in the bulk, the boundary layers, at the free surface, and the moving contact lines based on estimates from [Milner \(1991\)](#) and [Miles \(1967\)](#).

The total dissipation rate γ_t of a single mode in an experiment can be evaluated based on the idea ([Douady, 1990](#); [Christiansen *et al.*, 1995](#)) that a minimum acceleration A required to excite a

specific pattern of wavenumber k is proportional to:

$$\gamma_t = k A \tanh(k h)/(4 \omega_0). \quad (\text{A2.2})$$

Since the data presented in figure 2.4a are close to the minimum of each tongue, γ_t varies between 0.58 and 0.66 s^{-1} as the driving frequency changes as per that figure. We believe such values correspond to reasonably low dissipation rates, in particular, in the sense that they do not upset the monotonic behavior of the wavenumber selection, cf. §2.2.2, as opposed to some of the previous studies (Douady, 1990). Also, direct comparison of numerical values of γ_t for various single modes with available experiments in literature, in which the domain is rectangular and water is used as the working fluid, indicates the low dissipation in our system. For instance, the damping rate for mode (7, 1) from the Douady (1990) experiment (with the domain size of $65 \times 15 \text{ mm}^2$ and fluid layer depth of 4.85 mm) was found to be 2.89 s^{-1} considerably above that in our experiment. To further justify our claim, we need to consider various dissipation sources (in the bulk, in the boundary layers at the sidewalls and bottom, at the air-liquid interface, moving contact lines, and in the excited meniscus waves) in the cosine regime, cf. figure 2.4a.

Following the work of Kumar (1996), the damping rate due to the bulk dissipation for low viscosity fluid ($\nu k^2 \ll 2\omega_0$) for Faraday waves in a container of a finite depth h is $\gamma_{\text{bulk}} = 2(2\omega_0\nu)^{1/2}k / \sinh(2kh)$ rather than $2\nu k^2$ as often assumed (Ezerskii *et al.*, 1986; Milner, 1991; Christiansen *et al.*, 1995). The latter proves to be one of the primary contributions in our experiment and varies non-monotonically from 0.26 to 0.12 s^{-1} for the driving frequencies in figure 2.4a. However, as the inset in figure 2.4a indicates, the bulk dissipation alone does not account for dissipative effects as otherwise, as per the theory of Kumar & Tuckerman (1994), the measured wavenumbers should be larger than the ones predicted by the inviscid theory (Benjamin & Ursell, 1954) – instead they are noticeably lower, which indicates that the effect of boundary conditions and other sources of dissipation is dominant compared to that of the bulk. Increase of critical wavenumber with viscosity may seem counterintuitive as the frequency decreases with dissipation rate γ as $\omega_d^2 = \omega_0^2 - \gamma^2$ and hence from the dispersion relation (1.26) one might expect that the corresponding wavenumber

should decrease as well. However, the work of Kumar & Tuckerman (1994) showed the opposite, which is due to γ being dependent of the wavenumber k via $\gamma = 2\nu k^2$ – at short enough wavelengths the viscous dissipation dominates and overturns the linear and cubic growth of ω_0^2 with k due to gravity and surface tension, respectively. The latter is expected as at sufficiently short wavelengths λ the viscous timescale λ^2/ν becomes comparable with that of the wave $2\pi/\omega_0$.

The energy loss rates $\gamma_{\text{wall}} = \omega_0 \delta_\nu / L \approx 0.02 \text{ s}^{-1}$ at sidewalls of length L due to the (thin) Stokes boundary layers of thickness δ_ν and at the bottom $\gamma_{\text{bottom}} = (\omega_0 \nu / 2)^{1/2} k / \sinh(2kh) \approx 0.06 \text{ s}^{-1}$ are estimated based on the works of Miles (1967); Henderson & Miles (1990); Milner (1991); Christiansen *et al.* (1995). None of such estimates revealed value greater than 0.1 s^{-1} for sidewalls and bottom damping rates combined in our experiment. However, rectangular cells are known to have higher dissipation rate compared to cylindrical ones (Henderson & Miles, 1990), which can be attributed to the loss of energy at the corners of a rectangular tank where boundary layers are thicker.

Several estimates are available for dissipation rate γ_{surface} at the free surface, most of which are based on the work of Miles (1967) and confirm that in the case of contaminated surface the energy loss may even surpass that in the bulk by a factor of 4 based on empirical measurements (Milner, 1991; Christiansen *et al.*, 1995), thus giving about 1 s^{-1} , well above γ_t in our case. Also, using the formula $\gamma_{\text{surface}} = \omega_0 \delta_\nu k$ from Christiansen *et al.* (1995), based on the assumption that the interface is rigidified (completely covered with a contaminant) yields 0.56 s^{-1} indicating that even if the interface is affected by adsorbed surface active substances, the contamination in our case is far from saturation. Most importantly, presence of Marangoni stresses due to surface tension variations along the interface should increase the critical wavenumber (Kumar & Matar, 2004), which is in contrast to the observations, as per the inset in figure 2.4a.

Lastly, if one sums up the estimates for the damping sources the net result implies that there should be other considerable sources of dissipation, which, based on the previous discussion, should be due to the contact line mobility. While it is known that the damping from the moving contact line under certain conditions can exceed that produced by viscosity (Hocking, 1987a), there is no

rigorous theory. In our experiment due to the adoption of semi-pinned boundaries (§2.2.1), the contact lines have the freedom of moving up to 0.7 mm which should cause energy losses. The corresponding estimates available in literature, e.g. equation (13) in [Christiansen *et al.* \(1995\)](#) and equation (C.7) in [Milner \(1991\)](#), with the slip length $s = 10\forall$ yield

$$\gamma_{cl} = 16 \omega_0 \log(\delta_v/s) k \delta_v^2 / (\pi L) = 0.04 \text{ s}^{-1}, \quad (\text{A2.3})$$

which is much lower compared to the expected values from the experiments in literature, as has been investigated thoroughly by [Batson *et al.* \(2013\)](#). For example, the experiment conducted by [Benjamin & Ursell \(1954\)](#) in a *sealed* cylindrical water tank, where they had mode (1,2) excited, revealed a total damping rate of about 0.97 s^{-1} as extracted from figure 6a in [Batson *et al.* \(2013\)](#) or figure 3 in [Benjamin & Ursell \(1954\)](#). Although the condition of a low-viscosity fluid $\nu k^2 \ll 2\omega_0$ holds in their experiment, kh is much larger than unity due to the large depth h of about 25.4 cm, demonstrating that their experiment was conducted in the infinite depth regime, so that the bulk damping is simply $2\nu k^2 = 0.08 \text{ s}^{-1}$. Damping at the bottom $\gamma_{\text{bottom}} = (\omega_0 \nu / 2)^{1/2} k / \sinh(2kh)$ is negligible, since the fluid in motion is not in contact with the bottom surface given that the surface motion has the penetration distance of k^{-1} when $kh \gg 1$ ([Cerde & Tirapegui, 1998](#)). Damping at sidewalls due to the thin boundary layer is $\gamma_{\text{wall}} = \omega_0 \delta_v / L = 0.14 \text{ s}^{-1}$. The remaining sources of damping could be either at the surface or due to the motion of the contact line; since the water tank was sealed in [Benjamin & Ursell \(1954\)](#) experiment, it is unexpected to have the damping at the free surface as a prominent contribution to the total energy loss. Therefore, it can be concluded that the contact line contribution should be the chief source of dissipation as the sum of all the other damping rates discussed above ($\approx 0.22 \text{ s}^{-1}$) is much less than the total damping of $\gamma_t = 0.97 \text{ s}^{-1}$. However, for the experimental variables of [Benjamin & Ursell \(1954\)](#), the relation (A2.3) yields the value of $\gamma_{cl} = 0.24 \text{ s}^{-1}$, which is clearly an underestimate since $\gamma_t - \gamma_{\text{bulk}} - \gamma_{\text{bottom}} - \gamma_{\text{wall}} \approx 0.75 \text{ s}^{-1}$. We believe that this is also the case in our experiments due to similarity in the physical conditions.

2.D Common optical axis FTP for free surface waves

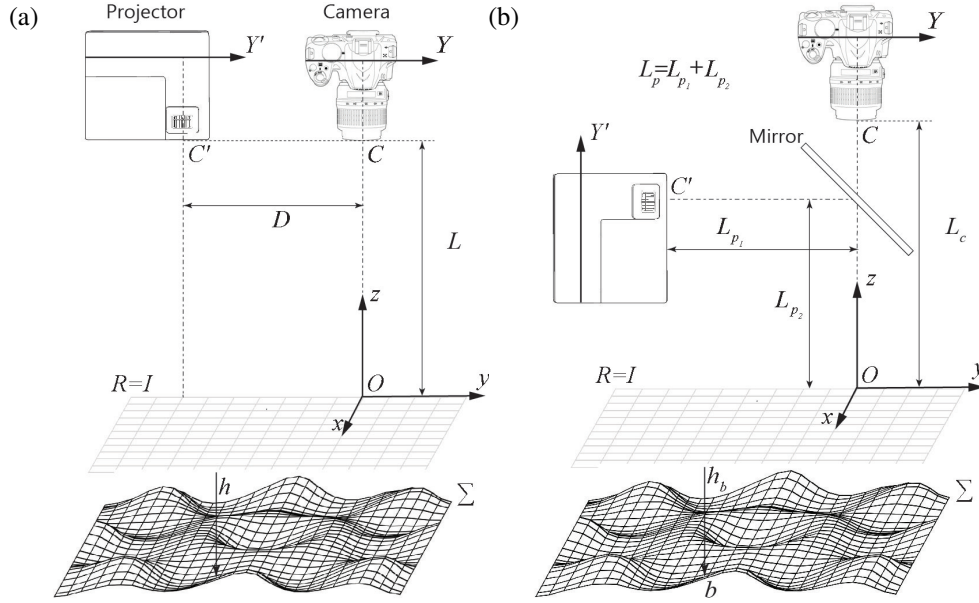


Figure A2.3: (a) and (b) depict parallel and common-optical axis geometry implementation of FTP, respectively.

As mentioned, we resorted to Fourier transform profilometry to reconstruct an accurate time history of the Faraday pattern three-dimensional landscape. Such a method is based on an optical system, cf. figure A2.3a, composed of a video projector displaying a grating pattern on the surface and a camera recording this pattern as the reference image. The deformed grating pattern following the deformation of the surface later is then recorded and compared to the reference image in order to produce a phase-shift map, from which the height of the deformed surface is reconstructed through an equation relating the *phase difference* to the *object's height*.

In an effort to improve the accuracy and applicability of the method we came up with a common-optical axis geometry implementation of FTP, cf. figure A2.3b, along with an appropriate phase-height relation. To make the common-optical axis geometry possible, i.e. bringing the camera and projector optical axes together, a semi-transparent mirror (standard 50/50 beam splitter) positioned precisely at 45 degrees, with respect to the projector and/or camera axis, was employed. In the following the derivation of the phase-height relation will be detailed.

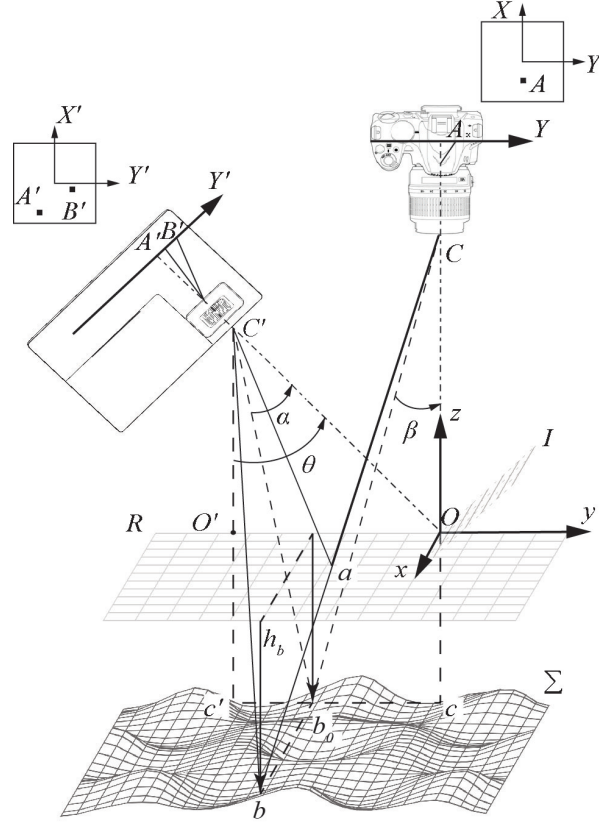


Figure A2.4: Geometry of the optical paths (Maurel *et al.*, 2009). In this figure, OC and $O'C'$ are equivalent to L_c and L_p : the distances of the camera and the projector from the unreformed surface, respectively. Also, the distance D between camera and projector here is denoted by cc' . Dashed lines $C'b_0$ and b_0C are the projections of the rays $C'b$ and bC on the $x = 0$ plane, and therefore, their inclination with respect to the line OC' and OC are measured as $-\alpha$ and $-\beta$, respectively. R denotes the reference plane and the camera object plane, whereas I represents the projector image plane.

In order to understand how the surface deformation can be reconstructed using the phase-shift map – produced from the comparison of the two images – one needs to investigate the recorded phase of light intensity at a given pixel of the camera image, and correspondingly the path of light reaching that pixel while being reflected from the flat surface in the first image and the deformed surface in the second one (Maurel *et al.*, 2009). As per figure A2.4, the intensity of the light arriving at the point A on the image plane XY is imposed by the intensity of the point A' on the grating plane $X'Y'$ when the ray is reflected from the reference plane R at the point a , whereas in the second image the reflected light from the deformed surface Σ at the point b – that reaches the same pixel A on the

camera – is originated from the point B' . Therefore, the recorded phase can be expressed as

$$\varphi_0(X, Y) = \varphi_{A'}(X, Y) = \omega_p Y'_{A'}, \quad (\text{A2.4a})$$

$$\varphi(X, Y) = \varphi_{B'}(X, Y) = \omega_p Y'_{B'}, \quad (\text{A2.4b})$$

where ω_p is the grating pattern frequency in the $X'Y'$ plane and is well-defined and known by the design. In order to determine the deformation h_b , cf. figure A2.4, at every point over the surface with the help of the phase difference $\Delta\varphi(X, Y) = \varphi - \varphi_0 = \omega_p (Y'_{B'} - Y'_{A'})$, it is required to find an expression for Y' in terms of X, Y, h_b , and other involved geometrical parameters.

Based on the elementary optics and considering the light paths inside the camera and projector, cf. figure A2.4, it is evident that

$$\tan \alpha = \frac{Y'_{B'}}{f_p}, \quad (\text{A2.5a})$$

$$\tan \beta = \frac{Y}{f_c}, \quad (\text{A2.5b})$$

where f_p and f_c are the focal length of the projector and the camera, respectively. On the other hand, based on the optical paths outside the camera and the projector, another set of expressions for $\tan \alpha$ and $\tan \beta$ can be derived: first $\tan(\theta - \alpha)$ can be written as $(D + y_b)/(L_p - h_b)$ and therefore,

$$\tan \alpha = \frac{(L_p - h_b) \tan \theta - (D + y_b)}{(D + y_b) \tan \theta + L_p - h_b} ; \quad (\text{A2.6})$$

whereas for the angle β we can write:

$$\tan \beta = -\frac{y_b}{L_c - h_b}. \quad (\text{A2.7})$$

Now an expression for y_b can be deduced using the above definition of $\tan \beta$ and the one in equation (A2.5b)

$$y_b = -\frac{Y(L_c - h_b)}{f_c}, \quad (\text{A2.8})$$

and accordingly with the substitution of the above result into (A2.6) and remembering $\tan \alpha = Y'_{B'}/f_p$ we obtain

$$Y'_{B'} = -f_p \frac{D - (L_c - h_b)Y/f_c - \tan \theta(L_p - h_b)}{L_p - h_b + \tan \theta[D - (L_c - h_b)Y/f_c]}, \quad (\text{A2.9})$$

thus, the phase function φ defined by equation (A2.4b) becomes

$$\varphi(X, Y) = -f_p \omega_p \frac{D - (L_c - h_b)Y/f_c - \tan \theta(L_p - h_b)}{L_p - h_b + \tan \theta[D - (L_c - h_b)Y/f_c]}. \quad (\text{A2.10})$$

Equation above is the general form for the phase function and hence the phase-height relation for various geometries can be deduced from this equation (Maurel *et al.*, 2009).

Parallel-optical axis geometry. When the optical axes of the camera and the projector are positioned in parallel, the reference plane R and the projector image plane I coincide, cf. figure A2.3a. Hence, with $L_p = L_c = L$ and $\theta = 0$, the equation above reduces to:

$$\varphi(X, Y) = -f_p \omega_p \frac{D - (L - h_b)Y/f_c}{L - h_b}, \quad (\text{A2.11})$$

and correspondingly by setting $h_b = 0$, the phase function for the undeformed surface is deduced

$$\varphi_0(X, Y) = -f_p \omega_p \frac{D - LY/f_c}{L}, \quad (\text{A2.12})$$

and from the last two equations $\Delta\varphi(X, Y)$ is determined

$$\Delta\varphi(X, Y) = -f_p \omega_p D \frac{h_b}{L(L - h_b)}. \quad (\text{A2.13})$$

Based on the definition of the magnification factor in a projector, $G_p = L/f_p$, the grating pattern frequency ω in the projector image plane I can be written as $\omega = \omega_p/G_p$, and finally the phase-to-height relation is deduced as

$$h_b = \frac{L\Delta\varphi}{\Delta\varphi - \omega D}. \quad (\text{A2.14})$$

As mentioned earlier, phase difference corresponds to the variation in the intensity at a *given pixel* of the camera, such as A , for a given change in the reflecting surface (R to Σ). Therefore, the recorded intensity in the reference image and the second image at the same pixel A is associated with two different points: point a while reflecting from the reference plane R in the first image and point b while reflecting from the deformed surface Σ in the second image, and h is measured at the latter point, cf. figure A2.4. Therefore,

$$h(x_b, y_b) = \frac{L\Delta\varphi}{\Delta\varphi - \omega D}, \quad x_b = x - \frac{h}{L}x, \quad y_b = y - \frac{h}{L}y, \quad \text{with } h = h(x_b, y_b), \quad (\text{A2.15a})$$

where the relations between x_b, y_b and x, y have been derived based on the fact that the rays aC and bC coincide, cf. figure A2.4, thus the cross product of their directional vector should vanishes.

Common-optical axis geometry. Takeda & Mutoh (1983) proved that the measurable range of slopes in FTP technique is limited by the ratio L/D , i.e. the larger the ratio the greater would be the maximum measurable slope. To that end, the two possible options are increasing L or reducing D . The former leads to the increased size of the projected pixel and hence reducing the overall accuracy of the method, whereas the latter is limited by the physical size of the camera and projector, cf. figure A2.3a. However, we achieved $D = 0$ by introducing a semi-transparent mirror – positioned precisely at 45 degrees, with respect to the projector and/or camera axis – which virtually decreases D to zero and brings the projector and camera axes together, cf. figure A2.3b.

As one can inspect, equation (A2.14) is not applicable directly for the common-optical axis geometry, as evaluating this equation at $D = 0$ yields the constant deformation $h_b = L$ over the entire surface, thus rendered as invalid. From the physical point of view, such an issue is attributed to the

fact that the grating pattern and the resulting image are being projected and observed, respectively, from an identical position, due to the zero distance between camera and the projector. To resolve this issue we consider the case where $L_c \neq L_p$. Therefore, starting from equation (A2.10)

$$\varphi(X, Y) = -f_p \omega_p \frac{D - (L_c - h_b)Y/f_c - \tan \theta(L_p - h_b)}{L_p - h_b + \tan \theta[D - (L_c - h_b)Y/f_c]}, \quad (\text{A2.16})$$

and setting θ and D to zero yields

$$\varphi(X, Y) = f_p \omega_p \frac{(L_c - h_b)Y/f_c}{L_p - h_b}, \quad (\text{A2.17})$$

and, as before, $\varphi_0(X, Y)$ can be determined by setting $h_b = 0$

$$\varphi_0(X, Y) = f_p \omega_p \frac{L_c Y/f_c}{L_p}. \quad (\text{A2.18})$$

Using $Y = -yG_c$, $f_c = G_c L_c$, $f_p = L_p/G_p$ and $\omega_p = \omega G_p$, where G_c denotes the camera magnification factor, the $\Delta\varphi(X, Y)$ becomes

$$\Delta\varphi(X, Y) = -\omega y \frac{h_b}{L_c} \frac{L_c - L_p}{L_p - h_b}, \quad (\text{A2.19})$$

and finally,

$$h_b = \frac{\Delta\varphi L_p}{\Delta\varphi - \omega y(1 - L_p/L_c)}. \quad (\text{A2.20})$$

It should be noted that in equation (A2.20) $y \neq 0$, otherwise $h_b = L_p$. Therefore, the common camera/projector axis has to be away from the area of interest, which, from an experimental point of view, leads to a substantial reduction of light reflection to the camera in the case of water surface waves.

Chapter 3

Controlling chaos by the system size

3.1 Chaotic Faraday waves and the road map

When a container is filled with a liquid and vibrated with sufficient acceleration in the direction of gravity, standing surface waves, historically named after Faraday ([Faraday, 1831](#)), oscillate with a frequency $\omega_0/2\pi$ half that of the forcing. Such waves have patterns with a large variety of shapes and symmetries (figure 3.1), depending on the fluid properties, layer depth, driving and boundary conditions. Our experimental setup (cf. Methods) produces Faraday waves and enables variation of the rectangular container length $L(t)$ in a time-dependent fashion with the help of computer controlled stepper motors while still maintaining the width of the container W and the liquid layer depth h constant.

In the rectangular (x, y) -domain, the surface deformation due to excitation of the single mode $l = (m, n)$ is

$$\zeta(t, x, y) = a_l(t, \tau) S_l(x, y), \quad (3.1)$$

where $a_l(t, \tau) = C_l(\tau) \cos[\omega_0 t + \phi_l(\tau)]$ and $S_l(x, y) = \cos(\pi m x/L) \cos(\pi n y/W)$, in which $C_l(\tau)$ and $\phi_l(\tau)$ are the Faraday wave amplitude and phase evolving on a slow timescale $\tau \gg 2\pi/\omega_0$, and m and n represent the number of half-wavelengths formed in each direction ([Benjamin & Ursell, 1954](#);

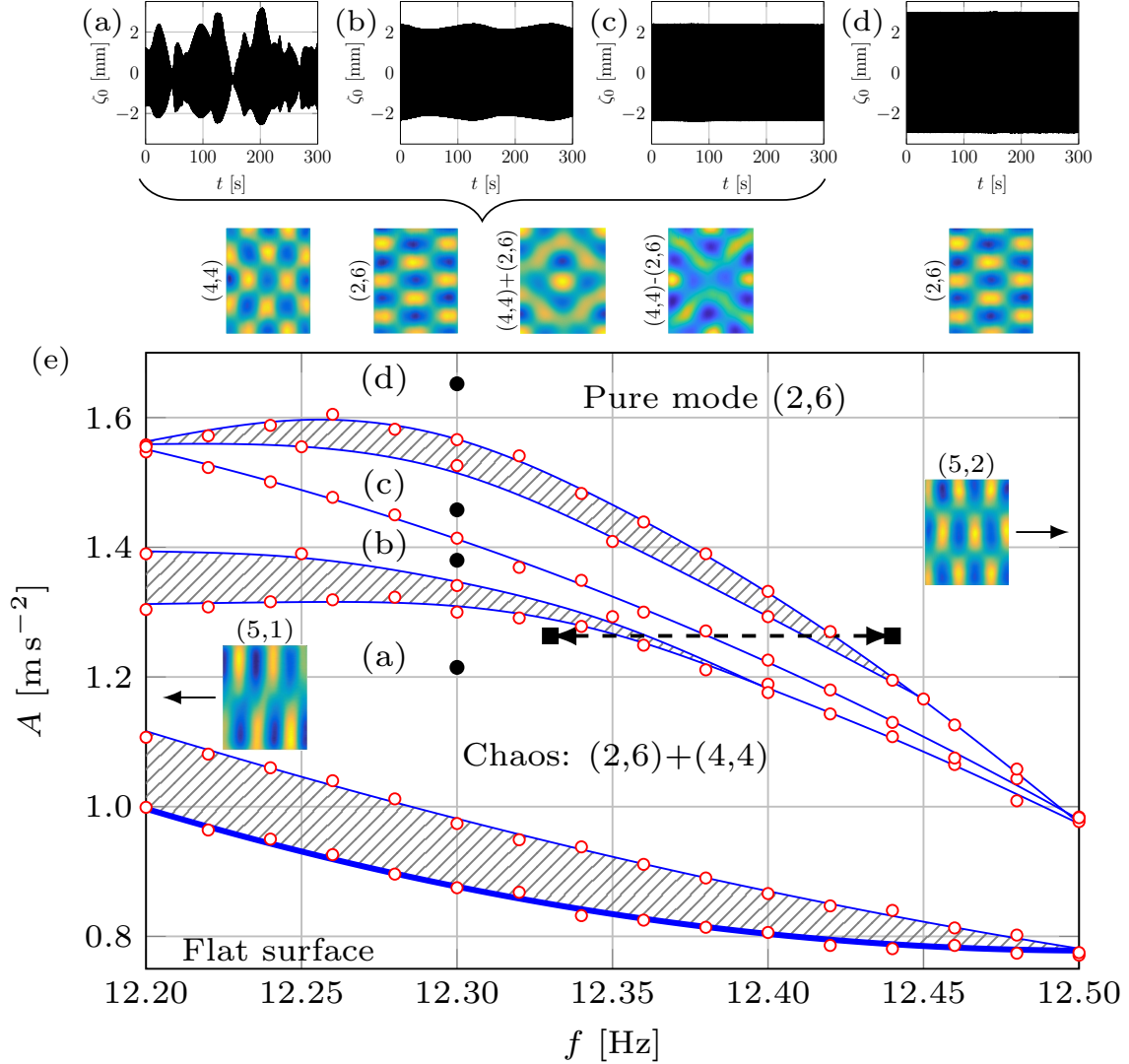


Figure 3.1: Physical experiment: road map. Interactions between modes (2, 6) and (4, 4) on the time-fixed domain of dimensions $L \times W = 120 \text{ mm} \times 150 \text{ mm}$. Surface deformations $\zeta_0(t)$ (a-d) corresponding to solid circles in the amplitude-frequency (A, f) map (e). Four distinct regions exist above the threshold (thick curve): the chaotic pattern competition (a), the periodic time-dependent (b) and -independent (c) pattern competition, and time-independent periodic pure mode (2, 6) in (d). Below the panels are the patterns observed when the respective $\zeta_0(t)$ was recorded: (2, 6) in (d) and all of (4, 4), (2, 6), (2, 6) + (4, 4), (2, 6) - (4, 4) in (a-c). The measurement error is $\delta A = 10^{-2} \text{ m s}^{-2}$.

(Simonelli & Gollub, 1987): for example, in figure 3.1a, the leftmost surface pattern corresponds to mode (4, 4).

Simultaneous excitation of two (adjacent) modes at the same values of driving amplitude and frequency (A, f) takes place in the overlap region of the two stability curves known as the pattern competition regime, which is common in Faraday wave phenomena (Ciliberto & Gollub, 1985b).

In this regime slow amplitudes $C_l(\tau)$ of two different patterns are both nonzero, non-equal, and oscillate with different phases at a frequency smaller than the driving one by more than two orders in magnitude (Ciliberto & Gollub, 1984, 1985a). According to (3.1), at the center of the container for the two modes $l_1 = (2, 6)$ and $l_2 = (4, 4)$, and with the addition of meniscus waves with the amplitude $a_M(t, \tau) = C_M(\tau) \cos [2\omega_0 t + \phi_M(\tau)]$, we have:

$$\zeta_0(t) \equiv \zeta(t, L/2, W/2) = a(t, \tau) + a_M(t, \tau), \quad (3.2)$$

where $a(t, \tau) = a_{l_1}(t, \tau) + a_{l_2}(t, \tau) \equiv C(\tau) \cos [\omega_0 t + \phi(\tau)]$ is the superposition of the two Faraday modes. From $a(t, \tau)$ the amplitude envelope $C(\tau)$, wave frequency ω_0 , and phase ϕ are recovered and, accordingly, the Faraday waves slow amplitude $U(\tau) = C(\tau) e^{-i\phi(\tau)}$ is reconstructed. Using $\text{Re } U$ as the time series, the state of the dynamical system, either periodic or chaotic, is determined by measuring the fractal dimension D of the chaotic attractor, with a non-integer D corresponding to a chaotic state, whereas $D = 1$ to a periodic one (cf. Methods).

To navigate the experiments on time-dependent domains, first we developed the road map on the time fixed domain analogous to that in the literature (Simonelli & Gollub, 1989), in the (A, f) -space surrounding the pattern competition regime of the two modes $l_1 = (2, 6)$ and $l_2 = (4, 4)$, cf. figure 3.1e. This map is limited from the left and right by the excitation of nearby modes $(5, 1)$ and $(5, 2)$, respectively, and defines the boundaries between chaotic and periodic regimes which we will attempt to cross using domain deformation. Four distinct regions are observed above the threshold (thick curve): (a) chaotic competition between the two modes; (b) periodic competition with a time-dependent envelope; (c) periodic competition with a time-independent envelope; (d) the pure mode $(2, 6)$ oscillating periodically with a time-independent envelope. The shaded areas represent the hysteretic regions: for example, if one starts from below the threshold curve and increases the amplitude, in the lowest shaded area flat surface is observed, but if the starting point is in region (a), then by decreasing the amplitude and entering the shaded area, chaotic competition is exhibited. The surface patterns presented in figure 3.1a-d are observed during the record of the corresponding surface deformation ζ_0 at various instances in time, i.e. mode $(2, 6)$ in (d) and all of the combinations

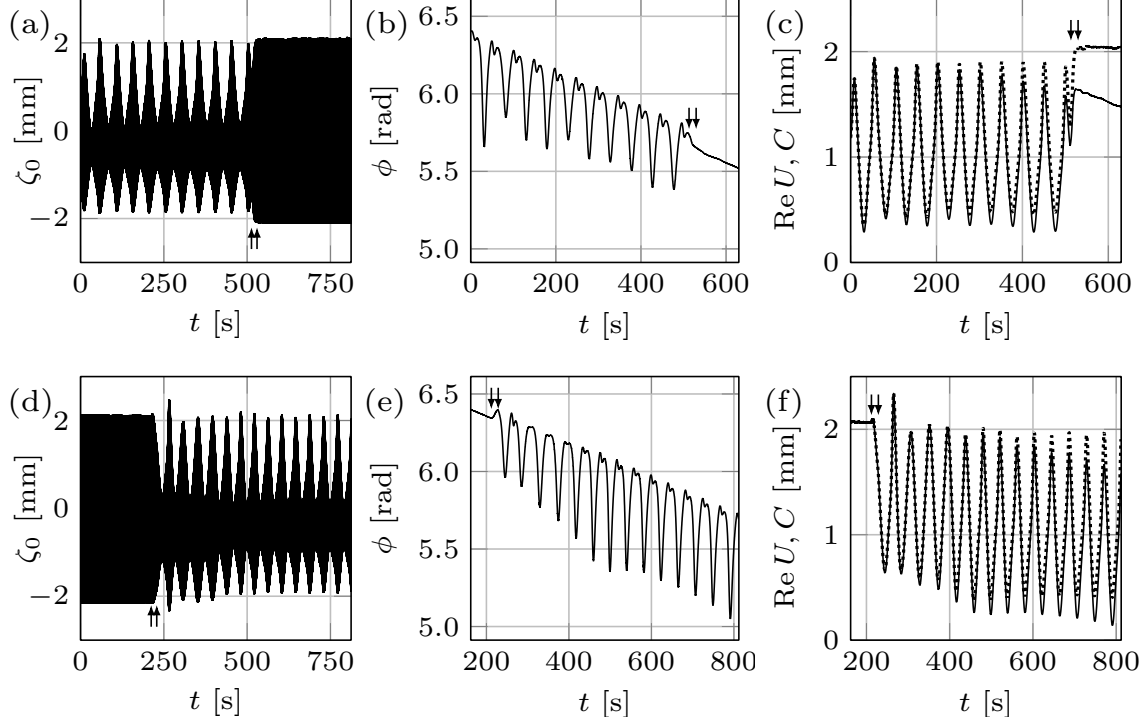


Figure 3.2: Physical experiment: regime change in response to domain deformation at $f = 12.33$ Hz and $A = 1.26 \text{ m s}^{-2}$. Top (bottom) row represents domain growth (shrinkage) by $\Delta L = 2 \text{ mm}$ at a rate 0.06 mm s^{-1} , over which the regime changes from chaotic (periodic) to periodic (chaotic). (a,d) The surface deformation $\zeta_0(t)$ with arrows indicating the start and finish of wall motion. (b,e) The slow phase ϕ . In (c,f) the amplitude envelope C and the real part of the slow amplitude $\text{Re } U$ are shown by dotted and solid curves, respectively.

$(4, 4)$, $(2, 6)$, $(2, 6) + (4, 4)$, $(2, 6) - (4, 4)$ in (a-c), because in any of the latter regions the two modes are competing. Finally, it must be noted that in our map (figure 3.1e), unlike mode $(2, 6)$, the pure mode $(4, 4)$ failed to exist because of the excitation of nearby modes, such as $(5, 1)$, at frequencies less than 12.20 Hz .

3.2 Traversing the edge of chaos by changing the system size

We start by illustrating how domain growth can lead to regularization of the chaotic regime corresponding to $f = 12.33 \text{ Hz}$, $A = 1.26 \text{ m s}^{-2}$, and $L = 120 \text{ mm}$, cf. figure 3.2a-c. Despite that $\text{Re } U$ may appear periodic (figure 3.2c), its analysis reveals a chaotic attractor with fractal dimension of $D = 1.38$ (figure 3.3a). At $t = 513 \text{ s}$ the domain starts to grow at a rate 0.06 mm s^{-1} and in the course of stretching for 2 mm the system reaches the periodic state, where mode $(2, 6)$ oscil-

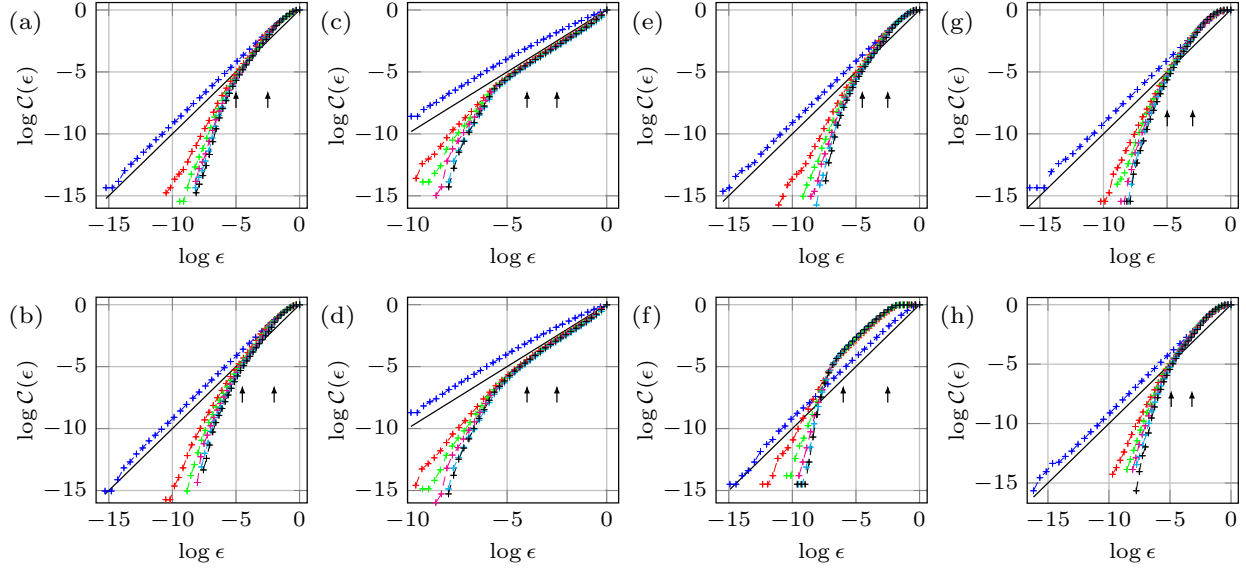


Figure 3.3: The correlation function, $C(\epsilon)$ obtained for each physical experiments from a single time series of the real part of the slow amplitude $\text{Re } U$ for various embedding dimensions m . The solid black line with slope is shown to compare with the saturated slope D in the scaling region (between the two arrows). Parts (a,b), (e,f), and (g,h) indicate the chaotic strange attractor dimension $D = 1.38, 1.42, 1.52, 1.00, 1.48,$ and 1.31 ± 0.02 , corresponding to figure 3.2a,d, figure 3.4a,d, and figure 3.5a,d, respectively. In (c) correlation function for 100 fast cycles prior to wall motion in figure 3.2d is presented indicating regular periodic dynamics with $D = 1.00 \pm 0.02$, whereas in (d) inclusion of 65 additional fast cycles corresponding to the interval of domain shrinkage $\Delta L = 1.3$ mm resulted in the fractal dimension $D = 1.1 \pm 0.02$ indicating the transition into chaos.

lates periodically with a time-independent envelope (figure 3.2a,c). Several *key observations* can be made from figure 3.2a-c. *First*, the fractal dimension D decreases with the domain size increasing as opposed to, say, Rayleigh-Bénard convection (Ahlers & Behringer, 1978; Paul *et al.*, 2007) in which D increases with the system size; in general, however, the trend can be reversed depending upon the interplay between the bulk and boundary dynamics. *Second*, using the initial phase and envelope within the time-independent regime as the reference, the regime transformation is accompanied by the changes in the slow phase (-0.9%) and envelope (36.1%) during the domain growth (figure 3.2b,c). *Third*, in this case the transition from chaotic to periodic state takes place during the wall motion (indicated by arrows) over $\Delta L = 1.68$ mm when the amplitude $a(t, \tau)$ reaches constant envelope, and once the motion ceases the system is already oscillating periodically with a time-independent envelope. However, this scenario is not universal: in other experiments, such as the one presented in figure 3.11a with an initial chaotic state of dimension $D = 1.82$ undergoing domain growth at a rate 0.15 mm s^{-1} , the transition to periodic regime is not confined to the do-

main deformation time interval (though, in this case the domain evolution interval is shorter in time owing to the faster wall motion). This difference could possibly be due to a weaker chaotic state in figure 3.2a-c ($D = 1.38$) compared to that in figure 3.11a ($D = 1.82$), which is characterized by more unstable (in terms of Lyapunov exponents) periodic orbits (Temam, 1997) and therefore requires longer transition regime in order to regularize the system. On the one hand, since a large number of unstable low-period orbits are embedded within a chaotic set, on which the trajectory of the chaotic process lives, sensitive dependence on small changes to the chaotic state implies that the system's behavior can be altered by using smaller (domain) perturbations for larger D . On the other hand, due to higher sensitivity at larger D , probabilistically it takes longer to 'hit' a periodic orbit with sufficiently large basin of attraction.

Next, using the periodic state reached at $L = 122$ mm as the initial state and then shrinking the domain back to the original length $L = 120$ mm (figure 3.2d-f) with the same wall speed returns the system to the chaotic state, but with a fractal dimension $D = 1.42$ (figure 3.3b). The reconstructed slow phase ϕ (figure 3.2e) and envelope C (figure 3.2f) indicate that the dynamical system is qualitatively experiencing a reverse process to that during the domain growth. However, the transition from periodic to chaotic state is shorter in length than the domain shrinkage interval: analysis of the amplitude $a(t, \tau)$ reveals that before the start of the domain shrinkage, the system is in a periodic state with $D = 1.00 \pm 0.02$ (figure 3.3c), while the domain shrinkage $\Delta L = 1.3$ mm leads to $D = 1.1$ (figure 3.3d), hence indicating a transition to chaos before the walls come to rest. Therefore, in comparison with the domain growth cases presented in figure 3.2a ($\Delta L = 1.68$ mm) and figure 3.11a ($\Delta L = 2$ mm), domain shrinkage (figure 3.2d) leads to regime transformation on a smaller domain size variation ΔL .

3.3 The effect of the domains evolution rate: chaos prevention

With the help of the same map (figure 3.1e), another remarkable ability of domain evolution to control chaos is identified: namely, isolating one of the competing modes in the regime, which on a time-fixed domain of the same size would otherwise correspond to a chaotic pattern competition. As

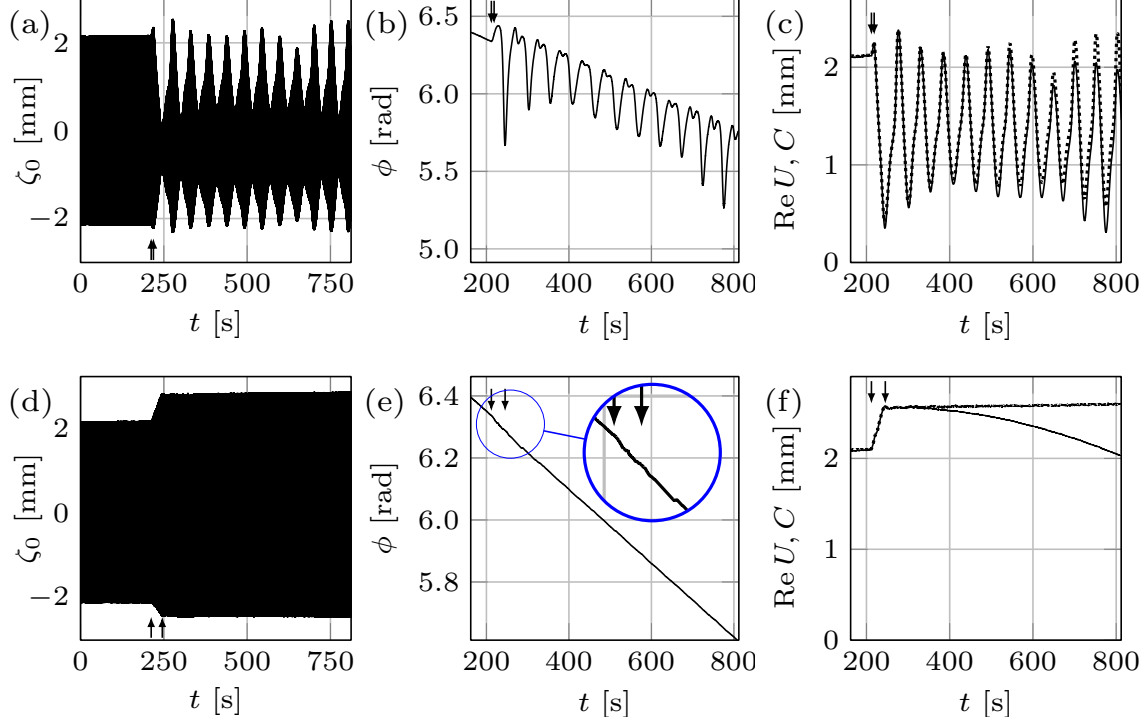


Figure 3.4: Physical experiment: wall speed effect at $f = 12.33$ Hz and $A = 1.26$ m s⁻². The slower evolution of the domain prevents the system from entering the chaotic regime. The domain shrinkage $\Delta L = 2$ mm starts at $L = 122$ mm with two wall speeds 0.15 (top) and 0.03 mm s⁻¹ (bottom).

evident from figure 3.1e, the system at $f = 12.33$ Hz and $A = 1.26$ m s⁻² is located in the chaotic competition regime – we examine if this final state of the system can be altered with the help of domain evolution at varying rates. These experiments are similar to the one in figure 3.2d-f but conducted at different evolution rates. Starting with the pure mode (2, 6) oscillating periodically with a time-independent envelope on the domain $L = 122$ mm we will see if, depending on the domain evolution rate, shrinking the domain to $L = 120$ mm would provide the ability to control the final state of the system, which is known to be chaotic on a time-fixed domain of the same size.

Top and bottom rows in figure 3.4 show two different runs at wall speeds of 0.15 and 0.03 mm s⁻¹, respectively. At 0.15 mm s⁻¹, the domain shrinkage leads to the chaotic pattern competition (figure 3.4a) – the regime expected on a time-fixed domain of the same size – with the strange attractor of dimension $D = 1.52$ (figure 3.3e). Surprisingly, decreasing the speed below 0.03 mm s⁻¹ prevents the system from entering the chaotic regime (figure 3.4d), and makes it continue with periodic oscillation of mode (2, 6). That is, domain deformation isolates mode (2, 6) out of the potential (expected

on a time-fixed domain of the same size) chaotic pattern competition regime, which is confirmed by the attractor dimension study in figure 3.3f showing $D = 1.00 \pm 0.02$. Furthermore, as shown in figure 3.4d, even after 535 s from the moment the walls are brought to rest, the system remains in the periodic steady state. The two other performed experiments (not presented here) at the speeds 0.3 and 0.015 mm s^{-1} indicated the same result as above, i.e. the former led to the chaotic state while the later allowed the system to remain periodic. Yet, with another domain shrinkage experiment at the wall speed 0.06 mm s^{-1} presented in figure 3.2d-f one can conclude that at this speed and above the system reaches the expected chaotic pattern competition regime, whereas for the speeds $\leq 0.03 \text{ mm s}^{-1}$, the chaotic behavior of the system is prevented. Between the two speeds of 0.03 and 0.06 mm s^{-1} , either of the chaotic or periodic final state is possible since no further experiments were performed in this range as the selected wall speeds to perform experiments were discrete with the selection criteria being doubling the speed (at least) from one experiment to another (0.015, 0.03, 0.06, 0.15, and 0.3 mm s^{-1}). Therefore, if slow enough, the domain deformation isolates one of the competing modes and forces the system to stay in the periodic state – altogether the signature of hysteretic behavior.

Surface profiles reveal that domain shrinkage at slow rates only shortens the wavelength λ_x of mode (2, 6), which is balanced out by the increase in wave amplitude (figure 3.4d) in accord with the mass conservation $C \times \lambda_x \times \lambda_y \approx \text{const}$. Thus, slow domain evolution is not strong enough to perturb the system away from the periodic state of mode (2, 6), i.e. the system is capable of adapting and thus staying near this periodic orbit; hence mode (4, 4) is no longer formed. On the contrary, during a rapid domain evolution the system experiences an instability leading to the appearance of mode (4, 4) and hence competition with the preexisting mode (2, 6) resulting in the chaotic regime. At intermediate speeds, the system transitions through the edge of chaos,¹ which separates the basins of attraction where perturbations decay either towards regular or chaotic regime, due to larger perturbations of the system caused, in particular, by sloshing induced by moving walls.

¹Topologically, the edge of chaos may have a very complicated structure in spatially extended systems as in the laminar-turbulent flow transition (Schneider *et al.*, 2007; C.-L. Chian *et al.*, 2013), where it is an unstable traveling wave, which corresponds to a saddle point lying at the basic boundary between regular and chaotic states

At the dynamical systems level, one of the fine effects of domain evolution is that it can force the dynamical system trajectory to be closer to one of its fixed points, allowing the system to reach (or remain in) a stable periodic state. At the physical level, this effect is due to wall motion affecting the bulk flow, which could be different for identical Faraday wave patterns (Périnet *et al.*, 2017). This leads to the possibility that hysteretic phenomena associated with the bulk flow structure (arising if one compares the well-developed flow on a fixed domain with the flow formed when walls move to the same domain size) might be responsible for this memory effect – the dependence of the final Faraday wave pattern on the dynamical system trajectory. Since observations indicate different patterns between the two cases – when the domain is stationary and when it evolves to the same size – the flow in the bulk must necessarily be different, thus establishing the fact of hysteresis.

3.4 Relation to frequency chirping

From the dispersion relation $\omega_0^2 = [gk + (\sigma/\rho)k^3] \tanh kh$ for Faraday waves, one can see that the variation (chirping) of the frequency ω_0 in time affects the instability wavenumber $k(t) = |\mathbf{k}|$; hence, if the number of cells is not changing under the domain deformation, but the wavelength is being adjusted instead, domain shrinkage $k \uparrow$ should be equivalent to frequency increase $\omega_0 \uparrow$ and vice versa. However, due to the Eckhaus instability of the modes and because of the mode quantization on a finite size domain (Knobloch & Krechetnikov, 2015), the link between domain deformation and frequency chirping is not as monotonic as we saw from the road map in figure 3.1 and it is known in the literature (Simonelli & Gollub, 1989); nevertheless, we expect that the frequency chirping effect is related to changing the domain size. Thus, phenomena similar to that in figure 3.2 can be investigated with frequency being the controlling parameter, while the domain size is fixed at $L = 120$ mm (figure 3.5). To be able to compare the two processes, the initial starting point on the road map (figure 3.1) should be the same. In order to reveal the effects of frequency variation, it is desired to pass through all regions (a-d) in figure 3.1, from a chaotic to a periodic state of the pure mode (2, 6) and vice versa, which is achieved, as the one shown in figure 3.1e, at $A = 1.26 \text{ m s}^{-2}$ and f varying from 12.33 to 12.44 Hz at the rate of 0.0066 Hz s^{-1} , thereby taking the same amount of time as the

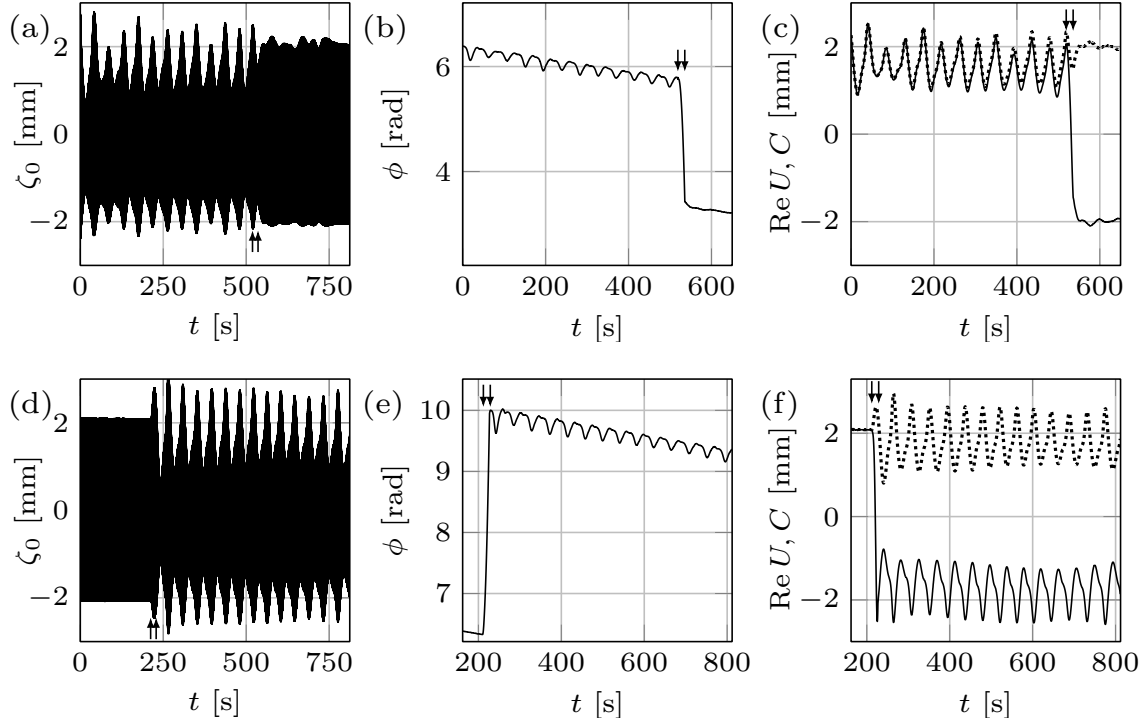


Figure 3.5: Physical experiment: regime change in response to frequency chirping. Frequency change $12.33 \text{ Hz} \leftrightarrow 12.44 \text{ Hz}$ takes place on fixed domain of size $L = 120 \text{ mm}$. Top (bottom) row represents frequency increase (decrease) for 0.11 Hz at the rate of 0.0066 Hz s^{-1} , due to which the regime changes from chaotic (periodic) to periodic (chaotic).

domain deformation (figure 3.2). Considering that in figure 3.5a location of the arrows indicates the start and the finish of the frequency chirping, it is evident that, unlike the domain deformation case in figure 3.2, the transition regime is extended far beyond the point where the frequency increase ceases: the envelope takes a considerably longer time (about 250 s) to become time-independent and thus to settle the regular regime than the frequency chirping application time. Since the chaotic attractor dimensions in these two cases are comparable ($D = 1.38$ and $D = 1.48$, respectively), this likely means that the system adapts better to domain size variation than to frequency chirping. To that end, figure 3.5b,c demonstrate relative changes in slow phase ϕ and the envelope C of -36.6% and 40.7% in the course of frequency chirping, respectively. It seems that this substantial change in the phase is the reason behind the extended transition in the frequency chirping case, whereas the corresponding phase change in the domain deformation case is negligible and correlated to a short transition regime contained in the wall motion interval. It must be noted that the observed

phase jumps -0.74π in figure 3.5b and 1.1π in figure 3.5e are not phase-slips requiring $\Delta\phi = 2\pi$ since they result from the appearance of a new mode (4, 4) on top of pre-existing one (2, 6) thus leading to a change in the total phase of both superimposed modes (3.2). This behavior differs from the standard frequency chirping when the driving frequency f crosses the border of the Arnold tongue leading to the loss of synchronization (zero detuning) between the driving and the oscillator frequencies and thus infinite growth of the phase difference (Pikovsky *et al.*, 2001). This growth is not uniform: there are epochs when the phase difference is nearly constant, and other, much shorter, epochs where the phase difference changes relatively rapidly by 2π , which is called a phase-slip. On the other hand, phase jumps, which are not multiples of 2π , are known to accompany phase synchronization transitions in chaotic systems which exhibit phase coherence (Lee *et al.*, 1998) as in our case, cf. Figs. 3.2b,e, figure 3.5b-e, and figure 3.4b. While the phase coherence of a chaotic attractor may mean that a suitably defined phase increases steadily in time, here we understand the phase coherence in a broader sense when the phase exhibits some pattern on a long timescale – the fact that chaotic systems, if examined over a sufficiently long time, can display regular patterns has been known for a while (Encinas-Sanz *et al.*, 2000) and could be the result of some symmetries underlying the dynamical system (Stewart, 2000).

The lower panels in figure 3.5 correspond to the reverse process, i.e. decrease of the frequency leading to the change of the regime from periodic to chaotic. Since the system reaches the chaotic state once the frequency decrease is finished (figure 3.5d), the transition regime should be short and contained in the frequency chirping interval. Compared to domain shrinkage (figure 3.2f), the envelope C in figure 3.5f (dotted curve) experiences a sharp increase during the very initial stage of frequency decrease, i.e. at the location of the first arrow. This is because on top of mode (2, 6) a new appearing mode (4, 4) superimposes thus increasing the total amplitude C of both modes. In general, while frequency chirping leads to a “domain flow” linear term in the corresponding amplitude equation (Fauve, 1998) similar to that for the actual domain flow (Krechetnikov & Knobloch, 2017) since both of them amount to the Doppler-like effect, at the nonlinear level there are crucial differ-

ences in the corresponding amplitude equations and thus in the finite-amplitude behaviors reported above.

3.5 The Ginzburg-Landau model

Spatially extended (and thus infinite-dimensional) systems are prone not only to temporal (amplitude) chaos, which is well studied in finite-dimensional contexts, but also to spatio-temporal chaos (van Hecke, 1998), in particular phase turbulence (Shraiman, 1986; Chaté & Manneville, 1995). A good example where both phase and amplitude chaos are observed is the temperature evolution in a well controlled time-dependent convection experiment (Mancini & Maza, 1997). Phase slips are the signature of the temporal chaos during which the amplitude of the wave goes to zero (defect) and the total phase of the system experiences a 2π jump, i.e. a wavelength is inserted or eliminated; in the phase-chaotic regime essentially no phase slips occur (Granzow & Riecke, 1996).

To gain further insights, in what follows we study the Ginzburg-Landau equation (GLE) on a time-dependent spatial domain as a minimal model. Although the current system is two-dimensional and would require two coupled GLEs to describe the two cross-roll hydrodynamic system (Hoyle, 2006), qualitative results can still be achieved using a single 1D complex GLE (cGLE) evolving on the slow time τ and long spatial $\xi \in [-L(\tau), L(\tau)]$ scales written here in a non-dimensional form (van Hecke, 1998):

$$U_\tau = (1 - i\mathcal{u})U + (1 + i\alpha)U_{\xi\xi} - (1 + i\beta)|U|^2U, \quad (3.3)$$

which incorporates an extra term $i\mathcal{u}U$ accounting for the effects of advection and dilution, where $\mathcal{u}(\tau, \xi)$ denotes the domain velocity at point ξ . Chaotic behavior exhibited by the cGLE on time-fixed domains and with $\mathcal{u} = 0$ has been extensively studied (Aranson & Kramer, 2002), and, therefore, will be used as a reference. Depending on the values of α and β , the cGLE on time-fixed domains can exhibit various behaviors including plane waves, spatio-temporal chaos, and intermittency (both chaotic and periodic) (Aranson & Kramer, 2002; van Hecke, 1998). The chaotic regime

occurs beyond the Benjamin-Feir-Newell curve $\beta \leq -\alpha^{-1}$, leading either to phase chaos, defect chaos, or bichaos (Aranson & Kramer, 2002; van Hecke, 1998). When U has no zeros, $|U|$ remains saturated and only its phase will be dynamically active, leading to phase chaos. On the contrary, if U reaches zero at some point ξ , then the complex phase is undefined there and a phase slip occurs leading to defect (amplitude) chaos. In the bichaotic regime, taking place for the values of α and β closer to the Benjamin-Feir-Newell curve $\alpha\beta = -1$ (van Hecke, 1998), a defect- and phase-chaotic attractors coexist.

3.5.1 Numerical simulation of cGLE on time-fixed domains

In the following, we first discuss the numerical treatment of the cGLE on time-fixed domain

$$U_\tau = U + (1 + i\alpha) U_{\xi\xi} - (1 + i\beta) |U|^2 U, \quad (3.4)$$

by means of pseudo-spectral method and exponential time-differencing, the combination of which was necessary due to the stiffness of the system (Boyd, 2001; Cox & Matthews, 2002). To that end, the latter two techniques will be discussed in a general context and later these results will be used as the basis for developing the required numerical framework in order to solve the cGLEs on time-dependent domains, cf. equation (3.3).

Pseudo-spectral method. To set up the stage, we start with the following spatial partial differential equation (PDE) governing the evolution of some vector function $U(\mathbf{x})$

$$\mathcal{L}U(\mathbf{x}) = f(\mathbf{x}) \quad \mathbf{x} \in \Omega \subseteq \mathbb{R}^n, \quad (3.5)$$

with boundary conditions

$$\mathcal{B}U(\mathbf{x}) = 0 \quad \mathbf{x} \in \partial\Omega, \quad (3.6)$$

where \mathcal{L} and \mathcal{B} are some linear operators. We intend to find the best approximation for function U , and to that aim, spectral and pseudo-spectral methods have been shown to be significantly accurate for a various type of applications (Cox & Matthews, 2002; Boyd, 2001; Canuto *et al.*, 1988; Fornberg, 1995). Therefore, we will resort to the latter to discretize the space.

Spectral methods are generally based on the approximation of a real, continuous, “well-behaved” function, $U(\mathbf{x})$, as an expansion in an orthogonal set of functions $\phi_n(\mathbf{x})$ called basis or trial functions

$$U(\mathbf{x}) \approx \tilde{U}(\mathbf{x}) = \sum_{n=0}^{N-1} \hat{a}_n \phi_n(\mathbf{x}), \quad (3.7)$$

where \hat{a}_n are the coefficients to be determined. Due to the above approximation, once equation (3.7) is substituted into (3.5) there is a non-zero residual $R = \mathcal{L}\tilde{U} - f$. This residual needs to be minimized with the help of weighting functions $\mathcal{X}_n(\mathbf{x})$, $n = 0, \dots, N - 1$, that allow the weighted average of residual become zero over the entire domain

$$\int_{\Omega} \mathcal{X}_n(\mathbf{x}) R d\mathbf{x} = 0, \quad n = 0, \dots, N - 1. \quad (3.8)$$

Weighting functions. Depending on the weighting functions’ type various numerical methods are developed (Boyd, 2001; Gurevich, 2016). For example, if the weighting functions are selected to be the same as the basis functions ϕ_n , then it is referred to as the Galerkin method. On the other hand, if the former are defined as the delta functions at spatial points \mathbf{x}_n , i.e. $\mathcal{X}_n(\mathbf{x}) = \delta(\mathbf{x} - \mathbf{x}_n)$, then the approach is called the “pseudo-spectral” method. In that case equation (3.8) leads to

$$\int_{\Omega} \mathcal{X}_n(\mathbf{x}) R d\mathbf{x} = \int_{\Omega} \delta(\mathbf{x} - \mathbf{x}_n) [\mathcal{L}\tilde{U}(\mathbf{x}) - f(\mathbf{x})] d\mathbf{x} = \mathcal{L}\tilde{U}(\mathbf{x}_n) - f(\mathbf{x}_n) = 0, \quad (3.9)$$

where the second step uses the sampling property of the delta function. Then, applying equation (3.7) leads to the following linear system of equations

$$\sum_{j=0}^{N-1} \hat{a}_j \mathcal{L}\phi_j(\mathbf{x}_n) = f(\mathbf{x}_n), \quad (3.10)$$

which can be used to determine all the unknown coefficients \hat{a}_j once the basis functions ϕ_j are selected.

Basis functions. In contrast with the finite-difference or finite element methods where the trial functions are local polynomials, spectral methods implement globally smooth functions, e.g. Fourier or Chebyshev series, and the particular choice is dependent on the geometry of the problem. For instance, with the spatially periodic intervals, as in the case of cGLE, Fourier series $\phi_j(\mathbf{x}_n) = e^{-i\mathbf{k}_j \mathbf{x}_n}$ is the natural choice (Boyd, 2001; Gurevich, 2016). Therefore, with the assumption of \mathcal{L} being a linear operator, equation (3.10) reduces to

$$\sum_{j=0}^{N-1} \hat{a}_j q(\mathbf{k}_j) e^{-i\mathbf{k}_j \mathbf{x}_n} - f(\mathbf{x}_n) = 0, \quad n = 0, \dots, N-1, \quad (3.11)$$

where q is deduced from the mapping of the basis functions ϕ_j through the linear operator \mathcal{L} , i.e. $\mathcal{L} \phi_j(\mathbf{x}_n) = q(\mathbf{k}_j) e^{-i\mathbf{k}_j \mathbf{x}_n}$.

For simplicity, we now turn to the one-dimensional case and accordingly set

$$x_n = n\Delta, \quad n = 0, \dots, N-1, \quad (3.12a)$$

$$k_j = \frac{2\pi j}{N\Delta}, \quad j = -N/2, \dots, N/2, \quad (3.12b)$$

which yields

$$\sum_{j=0}^{N-1} \hat{a}_j q(k_j) e^{-2\pi i j n / N} - f(x_n) = 0, \quad n = 0, \dots, N-1. \quad (3.13)$$

With the help of the discrete Fourier transform \mathcal{F} and its inverse \mathcal{F}^{-1}

$$\hat{a}_j = \mathcal{F}(a_n) = \frac{1}{\sqrt{N}} \sum_{n=0}^{N-1} a_n e^{2\pi i j n / N}, \quad (3.14a)$$

$$a_n = \mathcal{F}^{-1}(\hat{a}_j) = \frac{1}{\sqrt{N}} \sum_{j=-N/2}^{N/2} \hat{a}_j e^{-2\pi i j n / N}, \quad (3.14b)$$

equation (3.13) can be written as

$$\mathcal{F}^{-1} [\hat{a}_j q(k_j)] (x_n) - f(x_n) = 0, \quad (3.15)$$

and after applying DFT we obtain

$$\hat{a}_j q(k_j) - \mathcal{F} [f(x_n)] (k_j) = 0. \quad (3.16)$$

The Fourier transform of $f(x_n)$ can be computed efficiently using fast Fourier transform (FFT) algorithm available in MATLAB and therefore \hat{a}_j can be deduced using the equation above. The latter leads to the desired result: approximation of the solution \tilde{U} through equation (3.7).

Exponential time differencing method. When solving a PDE involving both temporal and spatial terms subject to spatially periodic boundary conditions, it is natural to express the solution as a sum of Fourier modes with time-dependent coefficients (Cox & Matthews, 2002; Boyd, 2001). However, the linear terms introduce stiffness into the resulting set of ODEs governing the mode amplitudes: indeed, the highest modes evolve on a very short time scale of the order $O(n^{-m})$, where n and m denote the mode number and the highest spatial derivative involved. For such problems, applying standard explicit time-stepping techniques, if feasible, is very costly as it requires extremely small time steps to integrate the resulting ODEs (Cox & Matthews, 2002). The exponential time differencing (ETD) exploits the advantages of the exact integration of the linear parts with the help of integration factor, while the nonlinear terms integration is treated approximately. This combination leads to a more accurate solution and superior performance compared to its counterparts such as linearly implicit schemes (Cox & Matthews, 2002).

Inspired by the cGLE's from, cf. equation (3.4), in this part we consider the PDE of the form

$$U_t = \mathcal{L}U + \mathcal{N}(U), \quad U = U(\mathbf{x}, t), \quad \mathbf{x} \in \Omega \subset \mathbb{R}^3, \quad t \in [0, T], \quad (3.17)$$

along with the initial condition $U(\mathbf{x}, 0) = U_0(\mathbf{x})$ in Ω and periodic boundary conditions. \mathcal{L} and \mathcal{N} denote the linear and nonlinear operators, respectively. Following the pseudo-spectral technique discussed above, we first discretize the space by taking the Fourier transform \mathcal{F}

$$\hat{U}_t = q(\mathbf{k})\hat{U} + \mathcal{F}[\mathcal{N}(U)], \quad (3.18)$$

where $\hat{U} = \mathcal{F}U$. Since $q(\mathbf{k})$ is not dependent on time, it may be treated as a constant variable for the current purpose of time discretization. To perform the exact integration of the linear terms involved, equation (3.18) should be multiplied by the integration factor e^{-qt}

$$\hat{U}_t e^{-qt} - qe^{-qt}\hat{U} = \frac{d}{dt} \left[\hat{U} e^{-qt} \right] = e^{-qt} \mathcal{F}[\mathcal{N}(U)], \quad (3.19)$$

and accordingly the integration over a single time step from $t = t_n$ to $t = t_n + h$ yields

$$\hat{U}(t_{n+1}) = \hat{U}(t_n) e^{qh} + e^{qh} \int_0^h e^{-q\tau} \mathcal{F}[\mathcal{N}(U(\mathbf{x}, t_n + \tau), t_n + \tau)] d\tau, \quad (3.20)$$

where we have used the change of variable $t = t_n + \tau$. The last integration in the above equation can be approximated with various approaches. For example, the assumption of \mathcal{N} evolving linearly in time between $t = t_n$ and $t = t_n + h$, i.e. $\mathcal{N} \approx \mathcal{N}^{(n)} + \tau \frac{\mathcal{N}^{(n)} - \mathcal{N}^{(n-1)}}{h}$, leads to the following scheme

$$\hat{U}^{(n+1)} = \hat{U}^{(n)} e^{qh} + \mathcal{F}[\mathcal{N}^{(n)}] \frac{(1 + qh)e^{qh} - 1 - 2qh}{qh^2} + \mathcal{F}[\mathcal{N}^{(n-1)}] \frac{-e^{qh} + 1 + qh}{qh^2}. \quad (3.21)$$

Integration of the cGLE on time-fixed domains. With the combination of pseudo-spectral methods and ETD now we are well equipped to treat the cGLE numerically: first we rewrite equation (3.4) in the Fourier space

$$\hat{U}_\tau = [1 - k^2(1 + i\alpha)] \hat{U} - \mathcal{F}[(1 + i\beta) |U|^2 U], \quad (3.22)$$

where we have used $\mathcal{F}U_{\xi\xi} = -k^2\widehat{U}$. Then, given that $[1 - k^2(1 + i\alpha)]$ is not a function of time, equation above can be classified as the type discussed in previous section, cf. equation (3.18), and therefore by setting $[1 - k^2(1 + i\alpha)] = q$, and $[(1 + i\beta)|u|^2u] = \mathcal{N}$ we can use the scheme (3.21).

3.5.2 Numerical simulation of cGLE on time-dependent domains

As mentioned earlier, to compare and interpret the results of our physical experiments we need to develop the framework for numerical simulations of a single complex GLE on time-dependent domains, cf. equation (3.3), where the evolution of the domain introduces new challenges and enigmas compared to the time-fixed domains scenario discussed above – these will be detailed below.

In our physical problem of Faraday waves, the appropriate length scale is the domain size and since in the case of time-varying domains $L(\tau)$ is not constant, the spatial variable in equation (3.3) needs to be scaled first, i.e. $\xi \rightarrow L(\tau)\xi$, thus

$$U_\tau = (1 - iu)U + \frac{1 + i\alpha}{L^2(\tau)} U_{\xi\xi} - (1 + i\beta)|U|^2U, \quad (3.23)$$

where for the case of isotropic growth $u(\tau, \xi)$ can be expressed as $u = \xi L'(\tau)/L(\tau) = \xi f(\tau)$ indicating that the velocity u of stretching depends on the location away from the stationary center $\xi = 0$ (Krechetnikov & Knobloch, 2017). Then, the above equation in Fourier space becomes

$$\widehat{U}_\tau = \left[1 - \frac{k^2(1 + i\alpha)}{L^2(\tau)} \right] \widehat{U} - (1 + i\beta)\widehat{U|\widehat{U}|^2} + if(\tau)\xi\widehat{U}, \quad (3.24)$$

and unlike equation (3.18) the coefficient of the linear term in equation (3.24) is not constant in time, i.e. $1 - k^2(1 + i\alpha)/L^2(\tau)$ is a function of time and the scheme demonstrated by equation (3.21) will not work. Indeed, the required integration factor in equation (3.24) can be written as

$$I = \exp \left[- \int 1 - \frac{k^2(1 + i\alpha)}{L^2(\tau)} d\tau \right], \quad (3.25)$$

and assuming domain growth at a constant rate, i.e. $L(\tau) = L_0 + v\tau$, we obtain

$$I = \exp \left[-\tau - \frac{k^2(1 + i\alpha)}{vL(\tau)} \right]. \quad (3.26)$$

Now multiplying equation (3.24) with the corresponding integration factor, and denoting the non-linear terms $-(1 + i\beta)\widehat{U}|\widehat{U}|^2 + if(\tau)\widehat{\xi}\widehat{U}$ as \mathcal{N} , the resulting equation simplifies to

$$\frac{d}{d\tau} \left[\widehat{U} I \right] = I \mathcal{N}, \quad (3.27)$$

leading to the following exact integration of the linear part of the equation over a single time step from $\tau = \tau_n$ to $\tau = \tau_n + h$

$$\begin{aligned} \widehat{U}(\tau_n + h)I(\tau_n + h) - \widehat{U}(\tau_n)I(\tau_n) &= \int_{\tau_n}^{\tau_n+h} I \mathcal{N} d\tau = \\ &= \int_0^h I(\tau_n + t) \left[\mathcal{N} \left(\widehat{U}(\tau_n + t, \xi), \widehat{\xi}, \tau_n + t \right) \right] dt, \end{aligned} \quad (3.28)$$

where the change of variable $\tau = \tau_n + t$ is used to arrive at the last integral above. Assuming \mathcal{N} grows linearly in time, i.e. $\mathcal{N} \approx \mathcal{N}^{(n)} + t \frac{\mathcal{N}^{(n)} - \mathcal{N}^{(n-1)}}{h}$ and using trapezoidal approximation for the integration we obtain

$$\widehat{U}(\tau_n + h)I(\tau_n + h) - \widehat{U}(\tau_n)I(\tau_n) = \frac{h}{2} \left[I(\tau_n + h) (2\mathcal{N}^{(n)} - \mathcal{N}^{(n-1)}) + I(\tau_n)\mathcal{N}^{(n)} \right]. \quad (3.29)$$

Thus, the developed numerical scheme becomes

$$\widehat{U}^{(n+1)} = \frac{h}{2} (2\mathcal{N}^{(n)} - \mathcal{N}^{(n-1)}) + \left(\widehat{U}^{(n)} + \frac{h}{2}\mathcal{N}^{(n)} \right) \exp \left[h + \frac{k^2}{v} \left(\frac{1}{L^{(n+1)}} - \frac{1}{L^{(n)}} \right) \right], \quad (3.30)$$

where hats denote discrete Fourier transforms which can be calculated using FFT command in MATLAB, and $L^{(n+1)} = L^{(n)} + vh$.

3.5.3 Traversing the edge of chaos

We first consider domain shrinkage and its reverse process in analogy with experiments in figure 3.2. Figure 3.6a,b depict the spatio-temporal bichaotic state on time-fixed domain – resulting from integration of (3.3) with $(\alpha, \beta) = (0.75, -1.4)$ and $\nu = 0$ up to $\tau_f = 500$ – used as the initial condition for integration on a time-varying domain. Then the domain growth by $\Delta L = 17.98$ at the rate of $\nu = 0.003$ brings the system to the periodic state (figure 3.6g). Figure 3.6c,d present $\text{Re } U(\xi, \tau_f = 6000)$ and $\text{Re } U(\xi = 0, \tau)$ where $5500 \leq \tau \leq 6000$, respectively, and indicate that the system has reached periodic state both in time and space, thereby proving the capability of domain evolution not only to control the temporal but also the spatial chaos. To examine the reversibility of the process, the domain growth is undertaken starting from the periodic state in figure 3.6c,d – as demonstrated in figure 3.6h, the system becomes chaotic right away and remains chaotic even beyond $\tau = 550$ for which the final stage is presented in figure 3.6e,f. Therefore, the regime transformation from chaotic to periodic is reversible, though the required change of the domain size during shrinkage and growth are not necessarily equal or even of the same order (figure 3.6g,h) as will be explained later. To confirm that domain shrinkage also has the capability to control chaotic state, a similar to the above numerical investigation is performed, except that the domain now first undergoes shrinkage and then growth. figure 3.7c,g indicate that the domain shrinkage by $\Delta L = 13.50$ brings the system to the periodic state and growth by $\Delta L = 7.68$ takes the system back to the chaotic state (figure 3.7e,h). Next, an important observation can be made from the comparison of the results of integration in figure 3.6 and figure 3.7, as both were initiated from an identical state (panels a and b in both figures). Compared to domain growth, shrinkage can make the system periodic over a smaller change in the domain size, i.e. $\Delta L = 13.50$ in figure 3.7a→c vs. $\Delta L = 17.98$ in figure 3.6a→c. The same observation is also made for the regime transformation from periodic to chaotic: domain shrinkage takes only $\Delta L = 1.66$ (figure 3.6c→e) whereas domain growth requires $\Delta L = 7.68$ (figure 3.7c→e). To understand this asymmetry between growth and shrinkage, note that compared to domain growth, domain shrinkage causes early phase-slips thereby leading to a faster change in the wavenumber structure of a pattern as known theoretically (Knobloch & Krechet-

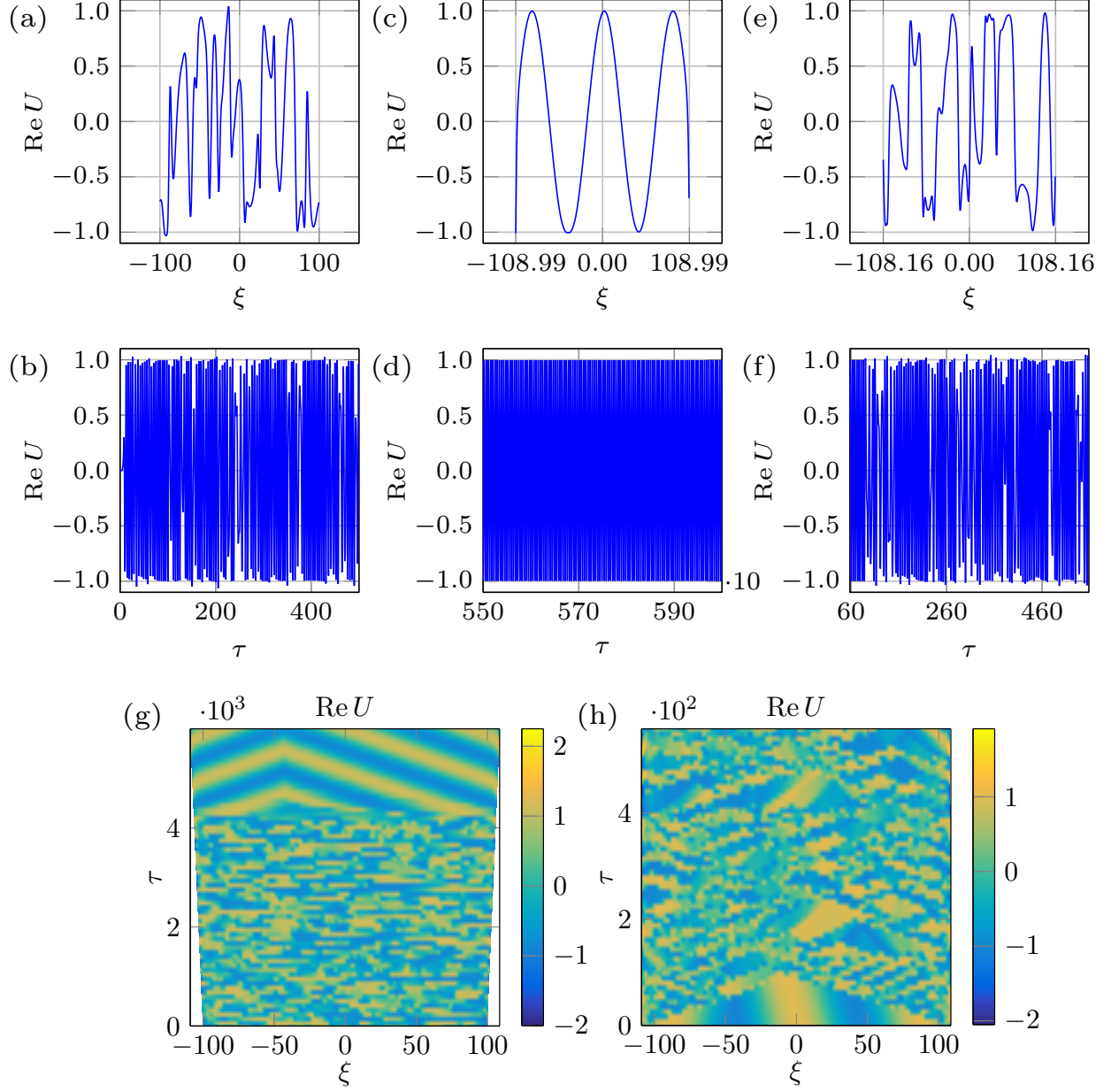


Figure 3.6: Numerical modeling: regime change in response to domain deformation. (a,b) the spatio-temporal bichaos used as the initial state with domain size fixed at $L = 200$ and $(\alpha, \beta) = (0.75, -1.4)$. In (c,d) the state of the system after domain growth by $\Delta L = 17.98$ at a rate $v = 0.003$, over which the regime changes from chaotic to periodic. Starting from the periodic state in (c,d), shrinking the domain by $\Delta L = 1.66$ at a rate $v = 0.003$ leads to the chaotic state (e,f). In (a,c,e) $\text{Re} U(\xi, \tau)$ is plotted at the corresponding final integrated time τ_f , whereas in (b,d,f) $\text{Re} U(\xi, \tau)$ is plotted at $\xi = 0$ over $\tau_f - 500 \leq \tau \leq \tau_f$. space-time plots of the growth and shrinkage processes are shown in (g) and (h), respectively.

nikov, 2015) in 1D and experimentally in 2D (Ghadiri & Krechetnikov, 2018). Hence, if the route to chaos requires the change in the wavenumber structure of the original periodic mode, then the difference in the phase-slip characteristic times between domain shrinkage and growth might be

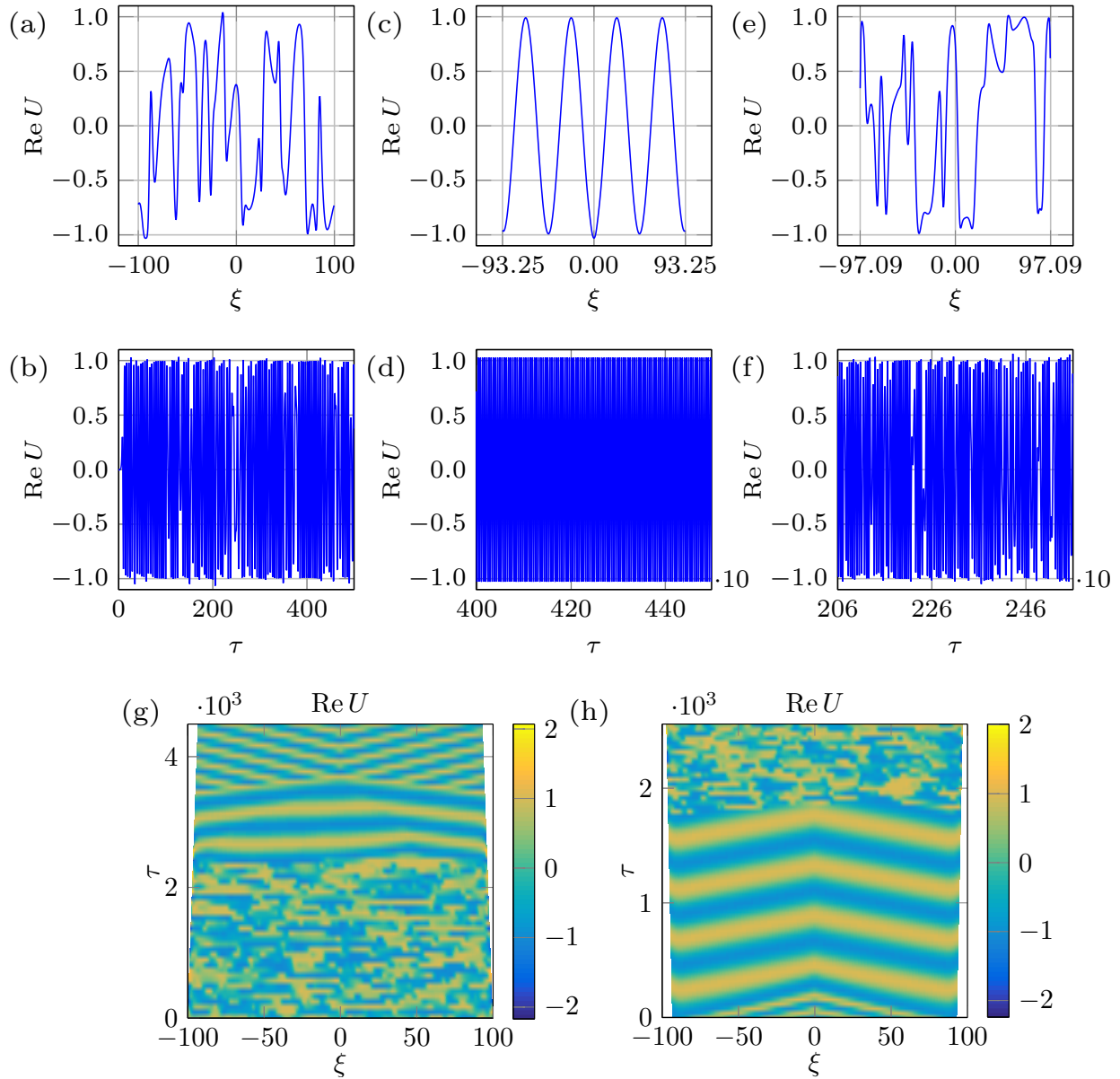


Figure 3.7: Numerical modeling: regime change in response to domain deformation. (a,b) depict the spatio-temporal bichaos used as an initial state with domain size $L = 200$ and $(\alpha, \beta) = (0.75, -1.4)$. In (c,d) the state of the system after domain shrinkage by $\Delta L = 13.50$ at a rate $v = 0.003$, due to which the regime changes from chaotic to periodic, is presented. Starting from the periodic state in (c,d), growing the domain by $\Delta L = 7.68$ at a rate $v = 0.003$ leads to the chaotic state (e,f). space-time plots of the shrinkage and growth processes are shown in (g) and (h), respectively.

responsible for the observed difference. If, on the other hand, the route to chaos from a given original periodic mode simply requires an excitation of another mode, the interaction of which with the original one (so-called pattern competition) leads to temporal chaos (Ciliberto & Gollub, 1984), then the difference could lie in the subcritical nature of the transition to chaos, which can occur

directly as it happens in other contexts, e.g. when a modulationally destabilized monochromatic wave in a fluid system undergoes a subcritical bifurcation directly into chaos, provided dissipation is weak enough (Moon, 2004). It is known that finite amplitude perturbations are needed in order to trigger subcritical instabilities (Krechetnikov & Marsden, 2009; E *et al.*, 2012). In the context of Faraday waves, such finite-amplitude perturbations are always present, e.g. in our system due to wall motion when domain size is changing. The direct transition from periodic to chaotic via subcritical bifurcation is justified not only by the periodic and chaotic regions being adjacent (Meron & Procaccia, 1986) in the amplitude-frequency (A, f) -plane, but also by the fact that superposition of modes, where chaos is observed, belongs to the subcritical side of the resonant tongue (Simonelli & Gollub, 1989). Given that in the case of domain shrinkage, modes from the subcritical side of the resonant tongue are excited via a finite-amplitude instability, while in the case of growth, modes from the supercritical side emerge – this entails irreversibility and therefore hysteretic behavior of Faraday waves (Ghadiri & Krechetnikov, 2019), which fundamentally is due to viscous dynamics of the bulk flow underlying the surface pattern (Périnet *et al.*, 2016, 2017).

While performing the above numerical investigation, we observed that domain shrinkage is more effective at controlling chaos; for instance, the domain growth fails to regularize the stronger chaotic state presented in figure 3.9a,b (compared to the weaker chaotic state in figure 3.6a,b), whereas domain shrinkage is able to make the system periodic starting from both the weaker and the stronger chaotic states. This fact is again rationalized as the early and hence more frequent phase-slips on domain shrinkage can control the stronger chaotic state better compared to delayed phase slips which tend to keep the system in its existing state. Furthermore, the ability of the domain shrinkage to reveal more delicate states and a higher number of patterns has been previously shown experimentally (Ghadiri & Krechetnikov, 2019).

3.5.4 The effect of the domain evolution rate

Finally, a numerical study is performed to demonstrate the effect of domain evolution rate similar to experiments in figure 3.4: a periodic state that is reached by the domain growth (figure 3.6c) is

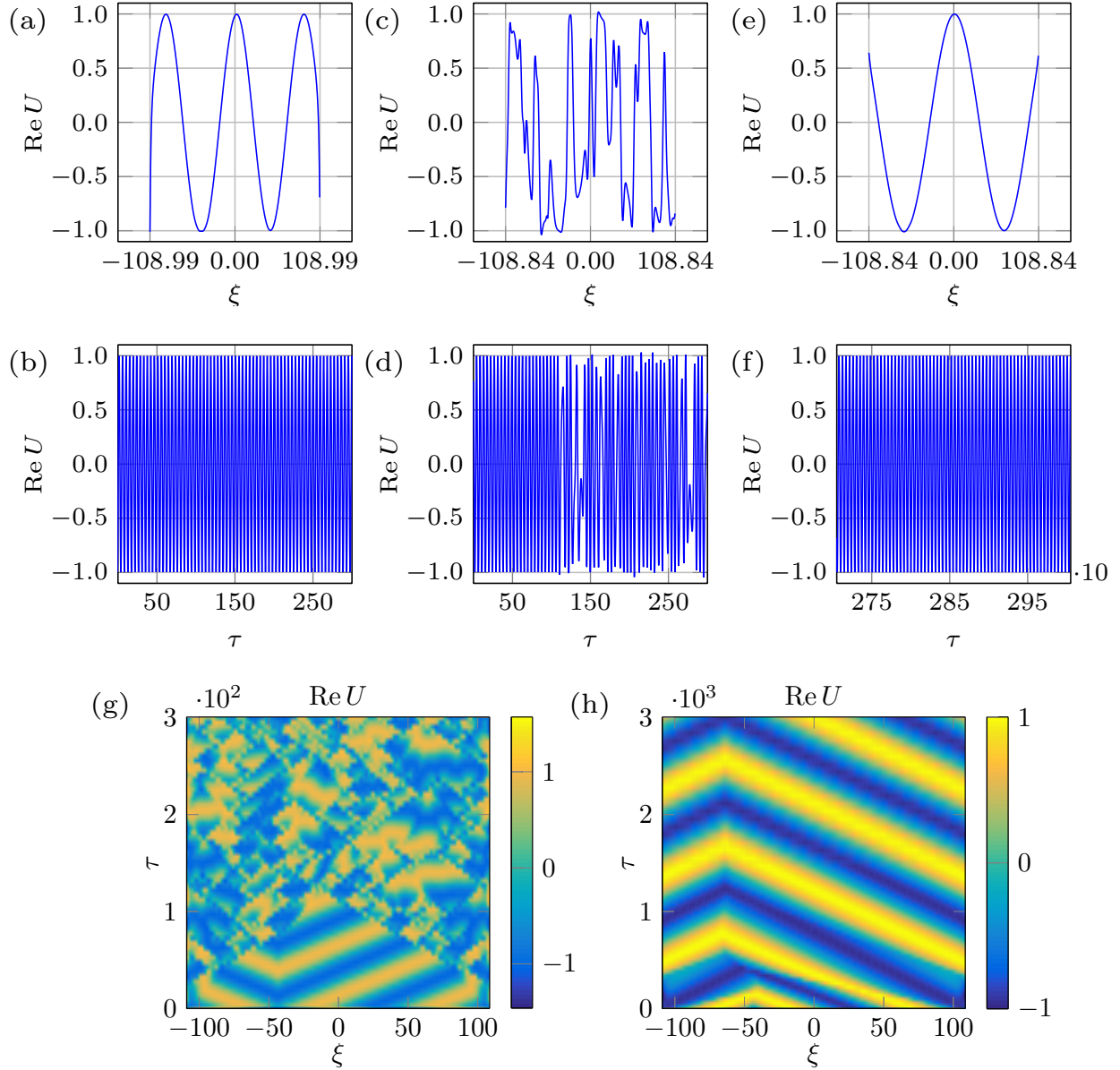


Figure 3.8: Numerical modeling: domain evolution rate effect. The slower domain evolution prevents the system from entering the chaotic regime. (a,b) depict the initial periodic state (figure 3.6c,d). The domain shrinkage $\Delta L = 0.3$ at two rates $v = 10^{-3}$ and 10^{-4} correspond to the middle (c,d) and right columns (e,f) respectively. space-time plots of the two processes are shown in (g,h).

used as the initial state for the domain shrinkage at various rates with the result shown in figure 3.8. The domain evolution by $\Delta L = 0.3$ at two rates $v = -0.001$ and $v = -0.0001$ reveals that the faster rate (figure 3.8c,d,g) allows the system to go back to the expected chaotic state, as in figure 3.6e,f; on the other hand, the slower rate (figure 3.8e,f,h) keeps the state of the system periodic.

We also started from a chaotic state rather than a periodic one in order to see if the shrinkage rate would play a role in controlling chaos. Using as an initial condition a stronger chaotic state (figure 3.9a,b) – reached by picking the values $(\alpha, \beta) = (0.8, -1.4)$ that are further away from the Benjamin-Feir-Newell curve $\alpha\beta = -1$ – the required domain shrinkage to enter the periodic regime at the rate of $\nu = 0.01$ is about $\Delta L = 100$ (figure 3.9c,g), whereas at the slower rate of $\nu = 0.001$, the required change in domain length is much smaller, $\Delta L = 15.4$ (figure 3.9e,h). As alluded to above, at a lower speed the system is subject to smaller perturbations, the slower associated time scales of which allow the system to adapt and get attracted to a periodic orbit; at a higher speed the perturbations are larger thus making it harder for a system to get attracted to a stable periodic orbit, which statistically takes longer time (larger domain size variation). In other words, a slower rate facilitates the regularization of the regime, while a faster rate impedes the process: this is analogous to the experimental results on regular Faraday waves on time-dependent domains (Ghadiri & Krechetnikov, 2019) showing that pattern formation is naturally impeded during fast domain evolution as phase slips have no time to develop. Furthermore, such results compare well with the 1D theoretical findings (Ueda & Nishiura, 2012) indicating that more complex pattern sequences can be expected with slow domain evolution, i.e. slower rates allow for more phase-slips to occur and lead to sooner changes in the state of the system.

3.6 Methods

The built experimental setup in figure 3.10 produces Faraday waves, and allows computer-controlled variation of the container dimensions in a time dependent fashion as well as measurement of the formed patterns characteristics. The designed Faraday assembly is mounted on top of the electrodynamic shaker (Labworks ET-139) and is controlled by a computer signal via amplifier. The liquid is housed in a container with a transparent bottom and four sidewalls, so that inner tank dimensions are $150 \times 150 \times 12.7 \text{ mm}^3$ without moving walls. The length $L(\tau_w)$ of the domain can be controlled in a time-dependent fashion according to the prescribed laws, where τ_w is a time scale longer compared to that of the vertical oscillations in order to avoid generating sloshing waves. Also, the fluid

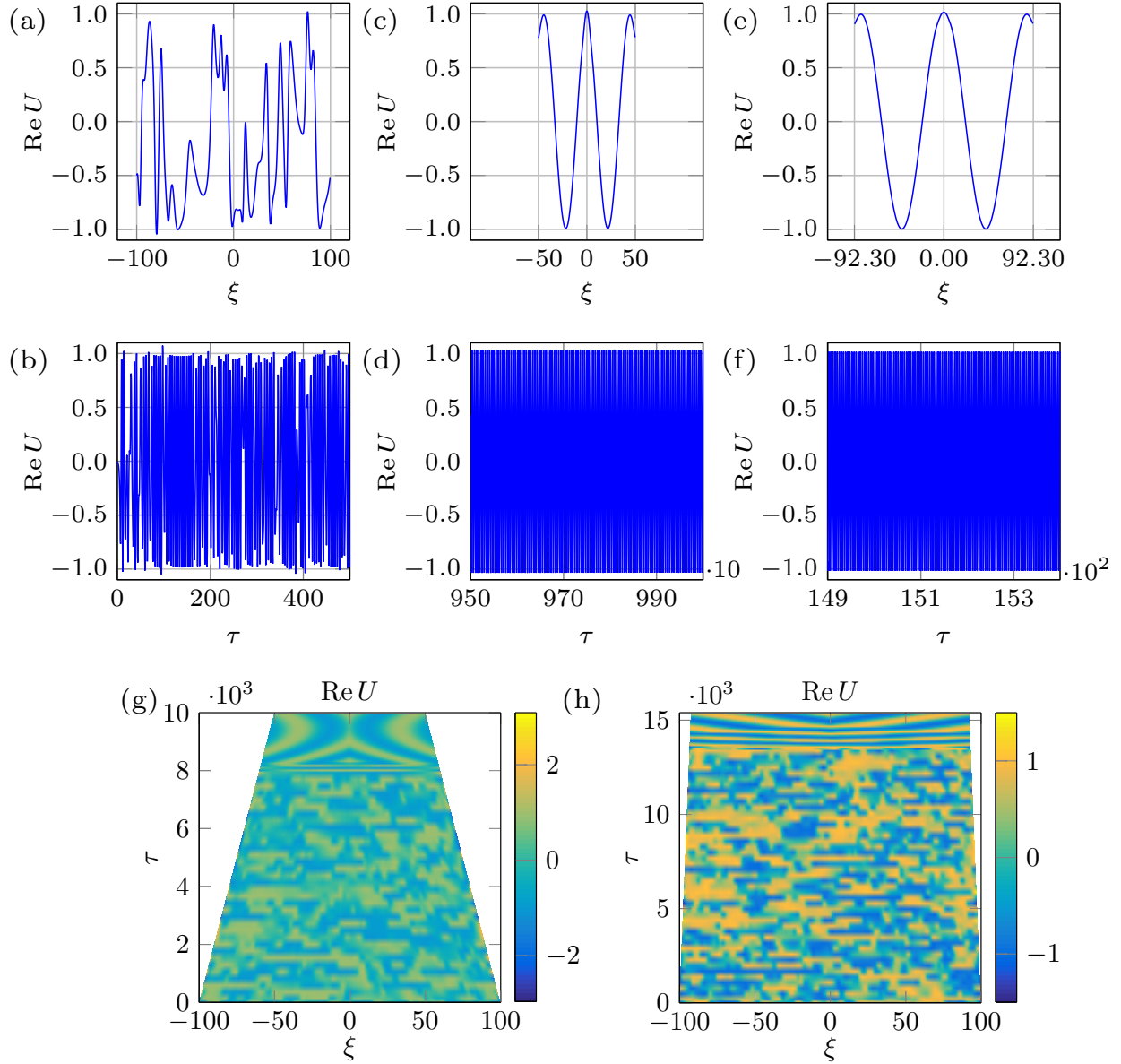


Figure 3.9: Numerical modeling: domain evolution rate effect. (a,b) depict the spatio-temporal bichaos used as the initial state with domain size $L = 200$ and $(\alpha, \beta) = (0.8, -1.4)$. The domain shrinkage $\Delta L = 100$ and $\Delta L = 15.4$, over which the regime changes from chaotic to periodic, with two different rates $\nu = 10^{-2}$ and 10^{-3} corresponding to the middle (c,d) and right columns (e,f), respectively. Space-time plots of the two processes are shown in (g,h).

layer depth is kept constant by allowing the moving sidewalls not to reach the bottom of the container, i.e. there exists a clearance of about 2 mm enabling unobstructed flow underneath the walls and not affecting Faraday waves (Ghadiri & Krechetnikov, 2019). Furthermore, considering the sensitivity of Faraday waves to possible evaporation and thus to water layer depth changes (Ghadiri & Krechetnikov, 2019; Douady, 1990), in our setup the water level was maintained constant at

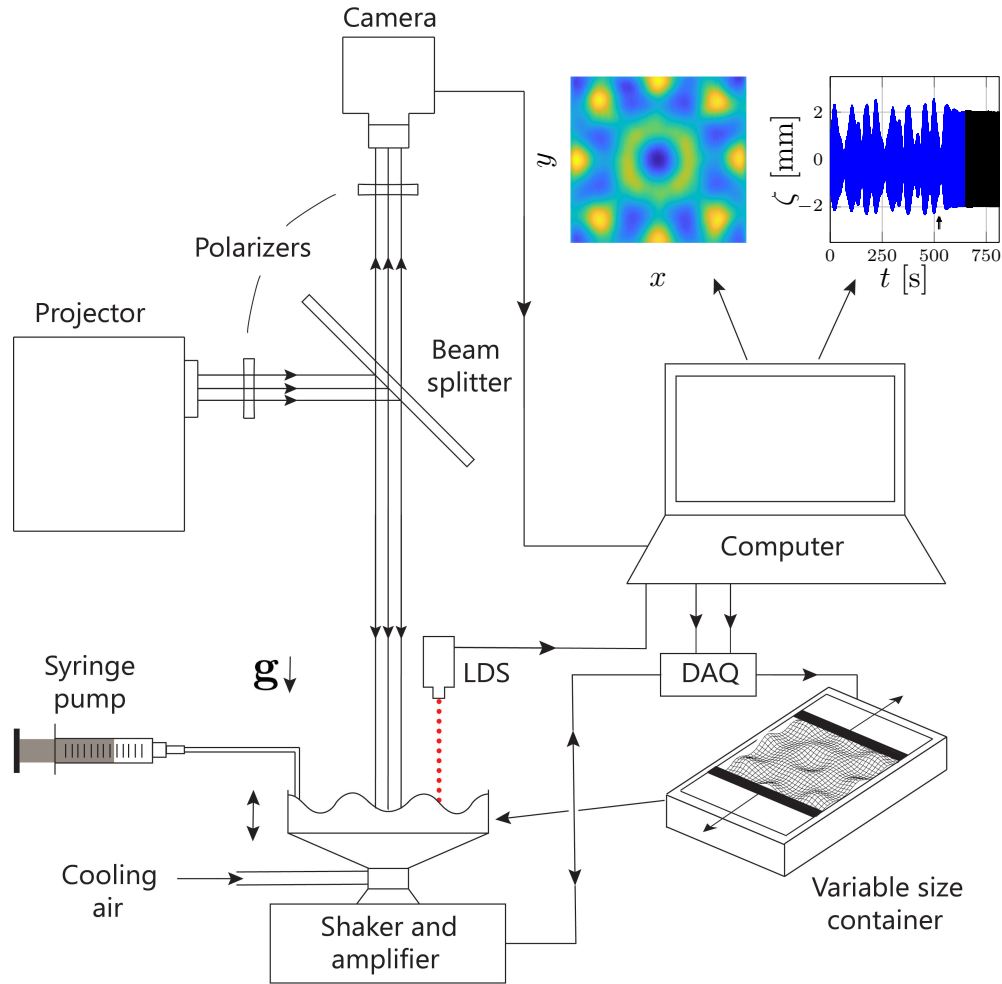


Figure 3.10: Experimental setup. Faraday waves assembly with variable size container is mounted on the shaker which is driven using the amplifier and controlled through the data acquisition card (DAQ). The surface wave amplitude is measured using the laser displacement sensor (LDS). The camera, projector, beam splitter, and polarizers form the optical part required to visualize the Faraday waves.

$h = 12 \pm 0.1$ mm with the help of a syringe pump (PHD ULTRA Harvard apparatus) which injects water outside the moving walls at the rate $42 \mu\text{l min}^{-1}$ required to compensate the evaporation for the given conditions in the lab.

Figure 3.10 also reflects on the optical setup used to visualize Faraday waves with the help of the Fourier transform profilometry (FTP) technique – a single-shot optical profilometric measurement of surface deformation – which has been widely used in water wave studies (Ghadiri & Krechetnikov, 2019; Cobelli *et al.*, 2011; Przada *et al.*, 2011). This method is based on an optical system composed of a video projector (ViewSonic PJD7820HD) casting a grating pattern on the water free

surface and a camera (Nikon D5200) recording the reflection of this pattern from the free surface. The grating pattern distorted due to deformation of the surface is then recorded and compared to the reference image of the undistorted grating pattern on the flat surface in order to produce a phase-shift map – the difference between phases of light intensity at each pixel in these two images – from which the height of the deformed surface is reconstructed using a relation between the phase shift and the object’s height. The highly accurate common-optical axis implementation of FTP for water surface waves introduced recently (Ghadiri & Krechetnikov, 2019) guarantees a vertical resolution of 0.05 mm. For further details on the experimental setup and the visualization technique the reader is referred to Ghadiri & Krechetnikov (2019).

For the present study, the setup reported in Ghadiri & Krechetnikov (2019) was modified in order to investigate temporal chaos. To that end, measurement of the waves amplitude at a single point on the surface suffices (Ciliberto & Gollub, 1985a) as explained below; hence, we resorted to a laser displacement sensor (Optex FA CDX-30A) allowing us to measure the surface deformation with the accuracy of 0.01 mm and the sampling rate of up to 80,000 per second. Although no spatial information is provided by the measurement at a single point (3.2), combination with the Fourier transform profilometry used to visualize the surface assured that there is no additional spatially-induced time dependence involved such as pattern rotation (Ciliberto & Gollub, 1985a). An example of controlling chaos by the domain deformation is provided in figure 3.11, which also illustrates the data analysis procedure. The surface deformation $\zeta_0(t)$ is recorded with the laser displacement sensor (LDS) at the vessel’s center (figure 3.11a), the Fourier transform of which (figure 3.11b) reveals that the strongest contribution is made by the Faraday waves oscillating at half of the driving frequency and the next contribution, though much weaker, comes from the meniscus waves. Such a process will be discussed in detail below. Blocks of data were recorded continuously over a 650 s interval, which is more than 20 times longer than required for the regime to change from periodic to chaotic or vice versa due to wall motion, also allowing us to carefully study the regime before and after the domain deformation. Moreover, being capable to record continuously – with loss of

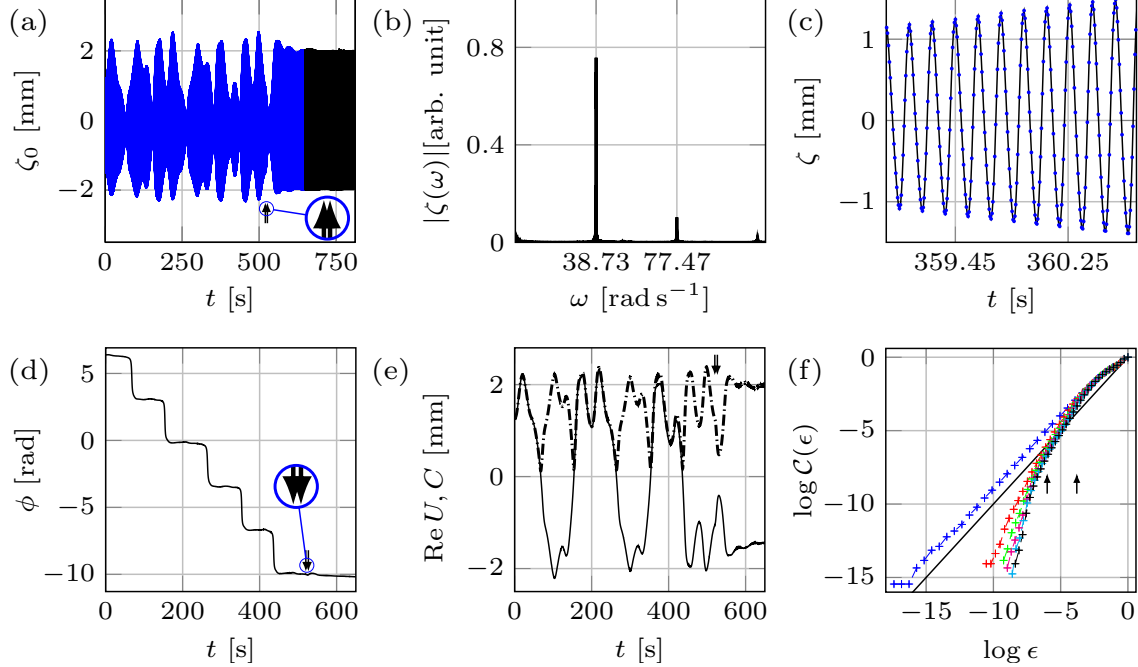


Figure 3.11: Data analysis procedure. (a) The recorded surface deformation ζ_0 at the vessel's center with arrows indicating the start and finish of wall motion. The experimental conditions: $f = 12.33$ Hz, $A = 1.16 \text{ m s}^{-2}$. The domain growth of $\Delta L = 2$ mm starts from $L = 120$ mm at $t = 520$ s with wall speed 0.15 mm s^{-1} . (b) Fourier transform's amplitude $|\zeta_0(\omega)|$ of the recorded surface deformation. (c) Data points recorded by the laser for several fast cycles are presented along with the curves fitted to the data. (d) The extracted slow phase ϕ . In (e) the amplitude envelope C and $\text{Re } U$ are shown by dashed and solid curves, respectively. (f) The correlation function $C(\epsilon)$ obtained from a single time series of $\text{Re } U$ for various embedding dimensions m . The solid black line with slope one signifies the saturated slope \mathcal{D} in the scaling region (between the two arrows) is larger than one.

data on the order of 0.1 s between the two blocks (figure 3.11a) – assured that the regime under investigation is not transient.

Collecting data at the rate 150 per second and with a vertical resolution of 0.01 mm enabled us to fully eliminate the meniscus wave contribution from the surface deformation. Following equation (3.1), the spatial contribution of the two modes l_1 and l_2 to the surface deformation at the center of the container reduces to unity, i.e. $S_{l_1} = S_{l_2} = 1$. Thus, with the inclusion of meniscus waves we arrive at equation (3.2). Given the Faraday waves total amplitude $a(t, \tau) = C(\tau) \cos [\omega_0 t + \phi(\tau)]$, the complex slow amplitude function is defined as:

$$U(\tau) = C(\tau) e^{-i\phi(\tau)}, \quad (3.31)$$

The real and imaginary parts of $U(\tau)$ can be reconstructed from the measurements as follows. From the recorded surface deformation given by (3.2), the amplitude envelope $C(\tau)$ (figure 3.11e), wave frequency ω_0 , and phase $\phi(\tau)$ (figure 3.11d) are recovered for each of the fast cycles individually sampled at the rate 25 data points per cycle, cf. figure 3.11c. Then, $\text{Re } U$ (figure 3.11e) and $\text{Im } U$ are determined based on equation (3.31). In figure 3.11d,e the extracted data are from the first block of 650 s (shown with blue color in figure 3.11a), covering 520 s of the chaotic regime, the domain growth of 6.67 s and the final periodic stage of 123.33 s. The second block of data – partially shown in figure 3.11a with black color – is provided just to confirm that the regime remains periodic. Finally, it should be noted that for different experiments, laser measurement naturally starts at an arbitrary instant within the single fast cycle period, resulting in a different initial phase ϕ . To have the same initial phase ϕ for all the experiments, during the data analysis we picked up the starting data point of the first fast cycle to be at (approximately) the same location during the fast cycle period for every experiment. Then, the reconstruction of the slow amplitude initiated from the first fast cycle with a specific value of ϕ , which in our case was selected to be 2.03π for the convenience of plotting; being close to 2π allows us to observe the effect of the phase in the slow amplitude U more clearly when the amplitude envelope C and $\text{Re } U$ are plotted in the same axes (figure 3.11e): with ϕ starting from 2π , C and $\text{Re } U$ are equal initially ($\text{Re } U = C \cos(2\pi) = C$) and as the phase evolves they start to differ from each other.

To determine the dynamic type of the Faraday wave regime we resorted to the analysis of the total amplitude $a(t, \tau)$ using the embedding technique (Takens, 1981; Grassberger & Procaccia, 1983c; Sauer & Yorke, 1991), which with the measurement at a single location on the surface not only reveals the regularity of the regime (the dimension of the strange attractor) but also the number of modes involved. This technique assumes that all the important dynamical features are contained (embedded) in a single time series. A strange attractor is characterized as an aperiodic one, in which the surrounding trajectories diverge exponentially from each other in time, and, most importantly, is an object of fractal dimension D , i.e. the number of small cells of size ϵ required to cover the attractor scales as ϵ^{-D} as $\epsilon \rightarrow 0$. The m -dimensional embedding phase-space coordinates

are constructed as $\{\text{Re } U[t], \text{Re } U[t + \delta t], \dots, \text{Re } U[t + (m - 1)\delta t]\}$, where δt is an arbitrary time delay. The theory (Takens, 1981; Sauer & Yorke, 1991) assures that the topological properties extracted from the above embedding, such as dimension and Lyapunov exponent, are equivalent to that of the attractor provided that $m \geq 2D + 1$. Practically, it is very difficult to measure D from an experimental data set (Ciliberto & Gollub, 1984, 1985a; Swinney & Gollub, 1986; Henry *et al.*, 2012); however, there exist equivalent estimates of D , the most common one being based on the correlation dimension:

$$D = \lim_{\epsilon \rightarrow 0} \frac{\log C(\epsilon)}{\log \epsilon} \leq D, \quad (3.32)$$

where $C(\epsilon)$ is the number of data-point pairs separated by a distance less than ϵ in the phase-space multiplied by N^{-2} with N denoting the total number of data points. The numerical implementation of (3.32) has been well developed in literature (Ciliberto & Gollub, 1984; Grassberger & Procaccia, 1983a; Henry *et al.*, 2012). Once $C(\epsilon)$ is determined and plotted against ϵ for different values of the phase-space dimension m , the limiting slope in the scaling region, e.g. in figure 3.11f the neighborhood of $\log(\epsilon) = -5$ shown by the arrows, defines the value of D . It can be seen from figure 3.11f that the slope in the scaling region does not change with further increase of m beyond four and is saturated at the value of 1.82 ± 0.02 which corresponds to the fractal dimension D of the strange attractor thus indicating that the system is in a chaotic state and can be described by a 4-dimensional phase-space formed by real and imaginary parts of the two slow amplitudes.

Conclusions

In this thesis, I explored the key differences in the dynamics between extended systems on time-fixed and time-dependent spatial domains. We chose to use the Faraday wave phenomenon as a testbed to study regular and chaotic dynamical properties of physical systems evolving on time-varying domains. Consequently, a vibrating fluid container with time-dependent dimensions was designed and constructed. Our study revealed how patterns transform in response to the domain dynamics on various length- and time-scales. In particular, we considered three regimes of domain evolution: shrinkage, growth, and oscillation leading to various remarkable findings. First, we observed that when a two-dimensional pattern is stretched in one direction, it most often experiences a wavenumber change in the transverse direction, a new twist to the well-studied Eckhaus instability in 2D. Second, the domain evolution rate was found as the key factor dictating the formation of patterns observed on the path between two domain aspect ratios. Its effects range from allowing the formation of complex sequences of patterns at slow rates to impeding the appearance of any new pattern on the path at higher rates. The primary differences in pattern formation on time-dependent domains with and without dilution and convective effects – the latter case is achieved by varying the liquid layer depth instead of the domains size – have been explored and it was found that the shrinkage-growth process is irreversible in the former case but reversible in the latter. The most intriguing result presented in this thesis was the discovery of a novel mechanism to traverse the edge of chaos, namely by time-variation of the domain size and in the extreme cases, i.e. at a very slow rate of the domain evolution, preventing the chaotic state altogether.

Given the difficulty and complexity of the systems evolving on time-dependent domains, in biology where the applications are ubiquitous, it is common to consider the domain size as an externally

imposed parameter, while in reality the tissue on which the spatial pattern resides is growing at a rate which is itself regulated by the diffusible chemicals that establish the spatial pattern. Also, despite much progress in observations, most theoretical studies resort to numerical simulations thus providing insufficient fundamental insight in the fundamental underlying mechanisms responsible not only for various metamorphoses in pattern formation, but also for the simple creation of a new pattern cell. The theoretical foundations for understanding pattern formation on time-dependent domains in one dimension have been laid out recently (Knobloch & Krechetnikov, 2014, 2015; Krechetnikov & Knobloch, 2017); however, this theoretical framework needs to be extended to two dimensions should one target the quantitative comparison of the experimental results presented in this thesis with theory. One question that is in need of immediate attention is the observed transverse instability phenomena where Eckhaus instability analysis fails to provide an adequate explanation, which is likely the result of the domain flow effects being neglected. Thus, it is required to derive a set of two-dimensional coupled Ginzburg-Landau equations from the Swift-Hohenberg equation in the presence of the domain flow and then to perform a thorough stability analysis. Once the theoretical framework for pattern formation on time-dependent domains in two dimensions is established, the subsequent study of controlling chaos by the domain size variation will be the next natural step.

With the pivotal role of Faraday wave phenomena in our study, another interesting avenue to explore is to extend the pertinent viscous theory (Kumar & Tuckerman, 1994) to the case of finite domains. The latter can be achieved by modeling the dissipation with the help of lubrication theory assuming the fluid layer being thin. This would allow for a better comparison to experimental results, for instance those presented in figure 2.5.

In summary, since the concepts of pattern formation and, especially, chaos are ubiquitous in nature and science, the results presented in this thesis should be of interest to various scientific and engineering fields.

Bibliography

- AHLERS, G. & BEHRINGER, R. P. 1978 Evolution of turbulence from the Rayleigh-Bénard instability. *Phys. Rev. Lett.* **40**, 712.
- ARANSON, I. S. & KRAMER, L. 2002 The world of the complex Ginzburg-Landau equation. *Rev. Mod. Phys.* **74**, 99–143.
- BARD, J. & LAUDER, I. 1974 How well does Turing’s theory of morphogenesis work? *J. Theor. Biol.* **45**, 501–531.
- BARTON, G. 1989 *Elements of Green’s Functions and Propagation: Potentials, Diffusion and Waves*. Oxford, UK.
- BATSON, W., ZOUESHTIAGH, F. & NARAYANAN, R. 2013 The Faraday threshold in small cylinders and the sidewall non-ideality. *J. Fluid Mech.* **729**, 496–523.
- BECHHOEFER, J., EGO, K., MANNEVILLE, S. & JOHNSON, B. 1995 An experimental study of the onset of parametrically pumped surface waves in viscous fluids. *J. Fluid Mech.* **288**, 325–350.
- BENJAMIN, T.B. & SCOTT, J. C. 1979 Gravity-capillary waves with edge constraints. *J. Fluid Mech.* **92**, 241–267.
- BENJAMIN, T.B. & URSELL, F. 1954 The stability of the plane free surface of a liquid in vertical periodic motion. *Philos. Trans. R. Soc. London* **225**, 505–4515.
- BINKS, D. & VAN DE WATER, W. 1997 Nonlinear pattern formation of Faraday waves. *Phys. Rev. Lett.* **78**, 4043–4046.

- BOYD, J. P. 2001 *Chebyshev and Fourier Spectral Methods*. Dover, New York.
- C.-L. CHIAN, A., NOZ, P. R. MU & REMPEL, E. L. 2013 Edge of chaos and genesis of turbulence. *Phys. Rev. E* **88**, 052910.
- CANUTO, C., HUSSAINI, M. Y., QUARTERONI, A. & ZANG, T. A. 1988 *Spectral Methods in Fluid Dynamics*. Springer-Verlag, Berlin, 1988.
- CASTETS, V., DULOS, E., BOISSONADE, J. & KEPPEL, P. DE 1990 Experimental evidence of a sustained Turing-type equilibrium chemical pattern. *Phys. Rev. Lett.* **64**, 2953–2956.
- CERDA, E. A. & TIRAPEGUI, E. L. 1998 Faraday’s instability in viscous fluid. *J. Fluid Mech.* **368**, 195–228.
- CHATÉ, H. & MANNEVILLE, P. 1995 Phase turbulence. In *Turbulence: a tentative dictionary* (ed. P. Tabeling & O. Cardoso), pp. 67–74. Plenum press, New York.
- CHRISTIANSEN, B., ALSTROM, P. & LEVINSSEN, M. 1995 Dissipation and ordering in capillary waves at high aspect ratio. *J. Fluid Mech.* **291**, 323–341.
- CILIBERTO, S. & GOLLUB, J. P. 1984 Pattern competition leads to chaos. *Phys. Rev. Lett.* **52**, 922–925.
- CILIBERTO, S. & GOLLUB, J. P. 1985a Chaotic mode competition in parametrically forced surface waves. *J. Fluid Mech.* **158**, 381–398.
- CILIBERTO, S. & GOLLUB, J. P. 1985b Phenomenological model of chaotic mode competition in surface waves. *Il Nuovo Cimento D* **6**, 309–316.
- COBELLI, P., MAUREL, A., PAGNEUX, V. & PETITJEANS, P. 2009 Global measurement of water waves by Fourier transform profilometry. *Exp. Fluids* **46**, 1037–1047.
- COBELLI, P. J., PAGNEUX, V., MAUREL, A. & PETITJEANS, P. 2011 Experimental study on water-wave trapped modes. *J. Fluid Mech.* **666**, 445–476.

- COX, S. M. & MATTHEWS, P. C. 2002 Exponential time differencing for stiff systems. *J. Comput. Phys.* **176**, 430–455.
- CRAIK, A. D. D. & ARMITAGE, J. G. M. 1995 Faraday excitation, hysteresis and wave instability in a narrow rectangular wave tank. *Fluid Dynamics Research* **15**, 129–143.
- CRAMPIN, E. J., GAFFNEY, E. A. & MAINI, P. K. 1999 Reaction and diffusion on growing domains: Scenarios for robust pattern formation. *Bull. Math. Biol.* **61**, 1093–1120.
- CROSS, M. C. & HOHENBERG, P. C. 1993 Pattern formation outside of equilibrium. *Rev. Mod. Phys.* **65**, 851–1112.
- DOUADY, S. 1990 Experimental study of the Faraday instability. *J. Fluid Mech.* **221**, 383–409.
- DOUADY, S. & FAUVE, S. 1988 Pattern selection in Faraday instability. *Europhys. Lett.* **6**, 221–226.
- E, W., ZHOU, X. & CHENG, X. 2012 Subcritical bifurcation in spatially extended systems. *Nonlinearity* **25**, 761–779.
- ECKHAUS, W. 1965 *Studies in non-linear stability theory*. Springer-Verlag, New York.
- EDWARDS, W. S. & FAUVE, S. 1994 Patterns and quasi-patterns in the Faraday experiment. *J. Fluid Mech.* **278**, 123–148.
- ENCINAS-SANZ, F., LEYVA, I. & GUERRA, J. M. 2000 Time resolved pattern evolution in a large aperture laser. *Phys. Rev. Lett.* **84**, 883–886.
- EZERSKII, A. B., RABINOVICH, M. I., REUTOV, V. P. & STAROBINETS, I. M. 1986 Spatiotemporal chaos in the parametric excitation of a capillary ripple. *Sov. Phys. JETP* **64**, 1228–1236.
- FARADAY, M. 1831 On a peculiar class of acoustical figures, and on the forms of fluids vibrating on elastic surfaces. *Philos. Trans. R. Soc. London* **121**, 299–340.
- FAUVE, S. 1998 Pattern forming instabilities. In *Hydrodynamics and Nonlinear Instabilities* (ed. C. Godr che & P. Manneville), pp. 387–492. Cambridge University Press.

- FENG, Z. C. & SETHNA, P. R. 1989 Symmetry-breaking bifurcations in resonant surface waves. *J. Fluid Mech.* **199**, 495–518.
- FORNBERG, B. 1995 *A practical guide to pseudospectral methods*. Cambridge Univ. Press, Cambridge, UK, 1995.
- FRANCESCO, P., MATHIEU, P. & SÉNÉCHAL, D. 1997 *Conformal field theory*. Springer.
- GHADIRI, M. & KRECHETNIKOV, R. 2018 Common-optical axis Fourier transform profilometry for water surface waves. *Exp. Fluids (to be submitted)* .
- GHADIRI, M. & KRECHETNIKOV, R. 2019 Pattern formation on time-dependent domains. *J. Fluid Mech.* **880**, 136–179.
- GOLLUB, J.P. 2006 Patterns and chaotic dynamics in Faraday surface waves. In *Dynamics of Spatio-Temporal Cellular Structures. Henri Bénard Centenary Review* (ed. I. Mutabazi, J. E. Wesfreid & E. Guyon), pp. 213–224. Springer, New York.
- GRANZOW, G. D. & RIECKE, H. 1996 Phase diffusion in localized spatiotemporal amplitude chaos. *Phys. Rev. Lett.* **77**, 2451–2454.
- GRASSBERGER, P. & PROCACCIA, I. 1983a Characterization of strange attractors. *Phys. Rev. Lett.* **50**, 346–349.
- GRASSBERGER, P. & PROCACCIA, I. 1983b Estimation of the Kolmogorov entropy from a chaotic signal. *Phys. Rev. A* **28**, 2591–2593.
- GRASSBERGER, P. & PROCACCIA, I. 1983c Measuring the strangeness of strange attractors. *Physica D.* **9**, 189–208.
- GU, X. M., SETHNA, P. R. & NARAIN, A. 1988 On three-dimensional non-linear subharmonic resonant surface waves in a fluid. Part I: theory. *Trans. ASME E: J. Appl. Mech.* **55**, 213–219.
- GUREVICH, S. 2016 Numerical methods for complex systems II. *Lecture notes* .

- HARTONG-REDDEN, R. & KRECHETNIKOV, R. 2011 Pattern identification in systems with $S(1)$ symmetry. *Phys. Rev. E* **84**, 056212.
- VAN HECKE, M. 1998 Building blocks of spatiotemporal intermittency. *Rev. Mod. Phys.* **80**, 1896–1899.
- HENDERSON, D.M. & MILES, J. W. 1990 Single-mode Faraday waves in small cylinders. *J. Fluid Mech.* **213**, 95–109.
- HENRY, B., LOVELL, N. & CAMACHO, F. 2012 Nonlinear dynamics time series analysis. *Nonlinear Biomedical Signal Processing, Dynamic Analysis and Modeling* **2**, 1–39.
- HOCKING, L. M. 1987a The damping of capillary-gravity waves at a rigid boundary. *J. Fluid Mech.* **179**, 253–266.
- HOCKING, L. M. 1987b Waves produced by a vertically oscillating plate. *J. Fluid Mech.* **179**, 267–281.
- HOYLE, R. B. 1993 Long wavelength instabilities of square patterns. *Physica D* **67**, 198–223.
- HOYLE, R. B. 2006 *Pattern Formation: An Introduction to Methods*. Cambridge University Press.
- JOST, J. 2013 *Partial Differential Equations*. Springer, New York.
- KIDAMBI, R. 2009 Capillary damping of inviscid surface waves in a circular cylinder. *J. Fluid Mech.* **627**, 323–340.
- KNOBLOCH, E. & KRECHETNIKOV, R. 2014 Stability on time-dependent domains. *J. Nonlinear Sci.* **24**, 493–523.
- KNOBLOCH, E. & KRECHETNIKOV, R. 2015 Problems on time-varying domains: formulation, dynamics, and challenges. *Acta Appl. Math.* **137**, 123–157.
- KONDO, S. & ASAI, R. 1995 A reaction-diffusion wave on the skin of the marine angelfish *Pomacanthus*. *Nature* **376**, 765–768.

- KOROLJA, A., WUC, H.-T. & RADISICA, M. 2019 A healthy dose of chaos: Using fractal frameworks for engineering higher-fidelity biomedical systems. *Biomaterials* **219**, 119363.
- KRECHETNIKOV, R. & KNOBLOCH, E. 2017 Stability on time-dependent domains: convective and dilution effects. *Physica D* **342**, 16–23.
- KRECHETNIKOV, R. & MARSDEN, J. E. 2009 On the origin and nature of finite-amplitude instabilities in physical systems. *J. Phys. A* **42**, 412004.
- KUDROLLI, A. & GOLLUB, J. P. 1996 Patterns and spatiotemporal chaos in parametrically forced surface waves: a systematic survey at large aspect ratio. *Physica D* **97**, 133–154.
- KUMAR, K. 1996 Linear theory of Faraday instability in viscous liquids. *Proc. R. Soc. Lond. A* **452**, 1113–1126.
- KUMAR, K. & TUCKERMAN, L. S. 1994 Parametric instability of the interface between two fluids. *J. Fluid Mech.* **279**, 49–68.
- KUMAR, S. & MATAR, O. K. 2004 On the Faraday instability in a surfactant-covered liquid. *Phys. Fluids* **16**, 39–46.
- LAMB, H. 1994 *Hydrodynamics*. Cambridge University Press.
- LANGER, J. S. & AMBEGAOKAR, V. 1967 Intrinsic resistive transition in narrow superconducting channels. *Phys. Rev.* **164**, 498–510.
- LEBLOND, P. H. & MAINARDI, F. 1987 The viscous damping of capillary-gravity waves. *Acta Mechanica* **68**, 203–222.
- LEE, K. J., KWAK, Y. & LIM, T. K. 1998 Phase jumps near a phase synchronization transition in systems of two coupled chaotic oscillators. *Phys. Rev. Lett.* **81**, 321–324.
- MADZVAMUSE, A., GAFFNEY, E. A. & MAINI, P. K. 2010 Stability analysis of non-autonomous reaction-diffusion systems: the effects of growing domains. *J. Math. Biol.* **61**, 133–164.

- MADZVAMUSE, A., MAINI, P. K. & WATHEN, A. J. 2003 A moving grid finite element method applied to a model biological pattern generator. *J. Comp. Phys.* **190**, 478–500.
- MANCINI, H. & MAZA, D. 1997 Bénard-Marangoni thermal oscillators: An experimental study. *Phys. Rev. E* **55**, 2757–2768.
- MATTHIESSEN, L. 1868 Akustische Versuche, die kleinsten Transversal wellen der Flüssigkeiten betressend. *Ann. Phys.* **134**, 107–117.
- MAUREL, A., COBELLI, P., PAGNEUX, V. & PETITJEANS, P. 2009 Experimental and theoretical inspection of the phase-to-height relation in Fourier transform profilometry. *Appl. Opt.* **48**, 380–392.
- MERON, E. & PROCACCIA, I. 1986 Theory of chaos in surface waves: the reduction from hydrodynamics to few-dimensional dynamics. *Phys. Rev. Lett.* **56**, 1323–1326.
- MILES, J. W. 1967 Surface-wave damping in closed basins. *Proc. R. Soc. Lond.* **297**, 459–475.
- MILES, J. W. & HENDERSON, D. M. 1990 Parametrically forced surface waves. *Ann. Rev. Fluid Mech.* **22**, 143–165.
- MILNER, S. T. 1991 Square patterns and secondary instabilities in driven capillary waves. *J. Fluid Mech.* **225**, 81–100.
- MOISY, F., RABAUD, M. & SALSAC, K. 2009 A synthetic Schlieren method for the measurement of the topography of a liquid interface. *Exp. Fluids* **46**, 1021–1036.
- MOON, H.-T. 2004 Subcritical modulational instability and transition to chaos from periodicity. *Phys. Lett. A* **325**, 324–328.
- OUYANG, Q. & SWINNEY, H. L. 1991 Transition from a uniform state to hexagonal and striped Turing patterns. *Nature* **352**, 610–612.

- PAINTER, K. J., MAINI, P. K. & OTHMER, H. G. 1999 Stripe formation in juvenile pomacanthus explained by a generalized turing mechanism with chemotaxis. *Proc. Natl. Acad. Sci. USA* **96**, 5549–5554.
- PAUL, M. R., EINARSSON, M. I., FISCHER, P. F. & CROSS, M. C. 2007 Extensive chaos in Rayleigh-Bénard convection. *Phys. Rev. E* **75**, 045203(R).
- PÉRINET, N., FALCÓN, C., CHERGUI, J. & JURIC, D. 2016 Hysteretic Faraday waves. *Phys. Rev. E* **93**, 063114.
- PÉRINET, N., GUTIÉRREZ, P., URRA, H., MUJICA, N. & GORDILLO, L. 2017 Streaming patterns in Faraday waves. *J. Fluid Mech.* **819**, 285–310.
- PIKOVSKY, A., ROSENBLUM, M. & KURTHS, JÜRGEN 2001 *Synchronization: a universal concept in nonlinear sciences*. Cambridge University Press.
- PRZADKA, A., CABANE, B., PAGNEUX, V., MAUREL, A. & PETITJEANS, P. 2011 Fourier transform profilometry for water waves: how to achieve clean water attenuation with diffusive reflection at the water surface? *Exp. Fluids* **52**, 519–527.
- RAYLEIGH, LORD 1883 On maintained vibrations. *Philos. Mag.* **15**, 229–235.
- SAUER, T. & YORKE, J. A. 1991 Rigorous verification of trajectories for computer simulation of dynamical systems. *Nonlinearity* **4**, 961–979.
- SCHNEIDER, T. M., ECKHARDT, B. & YORKE, J. A. 2007 Turbulence transition and the edge of chaos in pipe flow. *Phys. Rev. Lett.* **99**, 034502.
- SCHWARTZ, K. 2014 On the edge of chaos: where creativity flourishes. *KQED URL* <https://www.kqed.org/mindshift/35462/on-the-edge-of-chaos-where-creativity-flourishes> .
- SHRAIMAN, B. I. 1986 Order, disorder, and phase turbulence. *Phys. Rev. Lett.* **57**, 325–328.

- SIMONELLI, F. & GOLLUB, J. 1988 Stability boundaries and phase space measurements for spatially extended dynamical systems. *Rev. Sci. Instrum.* **59**, 280–284.
- SIMONELLI, F. & GOLLUB, J. 1989 Surface wave mode interactions: effects of symmetry and degeneracy. *J. Fluid Mech.* **199**, 471–494.
- SIMONELLI, F. & GOLLUB, J. P. 1987 The masking of symmetry by degeneracy in the dynamics of interacting modes. *Nuclear Physics B (Proceedings Supplements)* **2**, 87–95.
- STEWART, I. 2000 Traces of symmetric chaos. *Science* **288**, 55.
- SWINNEY, H.L. & GOLLUB, J.P. 1986 Characterization of hydrodynamic strange attractors. *Physica D*. **18**, 448–454.
- TAKEDA, M. & MUTOH, K. 1983 Fourier transform profilometry for the automatic measurement of 3-D object shapes. *Appl. Opt.* **22**, 3977–3982.
- TAKENS, F. 1981 Detecting strange attractors in turbulence. In *Dynamical Systems and Turbulence, Lecture Notes in Mathematics, Vol. 898* (ed. D. A. Rand & L. S. Young), pp. 366–381. Springer, New York.
- TEMAM, R. 1997 *Infinite-Dimensional Dynamical Systems in Mechanics and Physics*. Springer.
- TUCKERMAN, L. S. & BARKLEY, D. 1990 Bifurcation analysis of the Eckhaus instability. *Physica D* **46**, 57–86.
- TURING, A. M. 1952 The chemical basis of morphogenesis. *Philos. Trans. R. Soc. Lond. B* **237**, 37–72.
- UEDA, K.-I. & NISHIURA, Y. 2012 A mathematical mechanism for instabilities in stripe formation on growing domains. *Physica D* **241**, 37–59.
- URSELL, F., DEAN, R. G. & YU, Y. S. 1960 Forced small-amplitude water waves: a comparison of theory and experiment. *J. Fluid Mech.* **7**, 33–52.

- VASIL, G. M. & PROCTOR, M. R. E. 2011 Dynamic bifurcations and pattern formation in melting-boundary convection. *J. Fluid Mech.* **686**, 77–108.
- WALDROP, M. M. 1993 *Complexity: the emerging science at the edge of order and chaos*. Simon & Schuster.
- WRIGHT, W. B., BUDAKIAN, R. & PUTTERMAN, S. J. 1996 Diffusing light photography of fully developed isotropic ripple turbulence. *Phys. Rev. Lett.* **76**, 4528–4531.
- XIA, H., MAIMBOURG, T., PUNZMANN, H. & SHATS, M. 2012 Oscillon dynamics and rogue wave generation in Faraday surface ripples. *Phys. Rev. Lett.* **109**, 114502.